A NOVEL CONSTRUCTION OF WIND TUNNEL MODELS FOR WIND ENERGY APPLICATIONS

MSc. Thesis

Yorick de Valk

Documentnr.: EFD-331

UNIVERSITY OF TWENTE.

A NOVEL CONSTRUCTION OF WIND TUNNEL MODELS FOR WIND ENERGY APPLICATIONS

Thesis

by

Yorick Abraham de Valk

in partial fulfilment of the requirements for the degree of

Master of Science
in Mechanical Engineering

at the University of Twente department of Engineering Technology
to be defended on December 20th 2019

Thesis committee	
Chairman:	prof. dr. ir. C.H. Venner[1]
Supervisor:	dr. ir. A. van Garrel[1]
External members:	dr. ir. J.B.W. Kok[2]
	ir. J. van Muijden[3]

Document number: EFD-331

UNIVERSITY OF TWENTE.

[1]University of Twente, Faculty of Engineering Technology (ET), Engineering Fluid Dynamics (EFD)
[2]University of Twente, Faculty of Engineering Technology (ET), Thermal Engineering (THW)
[3]Royal Netherlands Aerospace Centre (NLR), Aerospace Vehicles Division

Preface and acknowledgements

This thesis is written to finalize my Master's degree in Mechanical Engineering at the University of Twente (UT) faculty of Engineering Technology in the Engineering Fluid Dynamics (EFD) group.

The project engaged in December 2018 with the original aim of designing and testing an add-on system for boundary layer suction (BLS) on wind turbine wing sections. As no thick wind-turbine style wings were present in de EFD group as base for designing a BLS system the idea of manufacturing a model came to mind. The Delft DU97-W-300 airfoil was chosen because of its relative thickness (30%c) and its frequent use in wind turbine blades. The plan was to suspend the model in the available balance, of which the accuracy was deemed sufficient based on the available documentation and experience. Nevertheless, surface pressure taps were incorporated in the model design to function as redundancy for determining the lift and drag.

The design and manufacturing of the model parts by the UT's 'Techno Centrum voor Onderwijs en Onderzoek' (TCO) was completed between February and May 2019 after which, at the start of June, the first wind tunnel tests where planned. Unfortunately during assembly of the measurement section a vital mistake was made which required the model to be suspended in the wind tunnel without surface pressure taps. During calibration of the balance significant discrepancies between the applied loads and recorded values came about. As no (reliable) method of measuring the aerodynamic forces was then available the experiments were forced to be cancelled.

The assembly mistake of the measurement section required new parts to be ordered from TCO causing multiple months of delay. Time limitations for the project then led to cancellation of the design and fabrication of the BLS system. To fill in the gap in the assignment a numerical analysis of the DU97-W-300 airfoil was proposed to complement the wind tunnel experiments which were then planned to commence in September. Based on the knowledge obtained during the courses on numerical analysis (NMME and CFD)[1] a grid refinement study was started which proved to be more involved than originally planned. Difficulties converging to a approximate exact solution lead to a more comprehensive study to the underlying causes.

In August the new, and improved, parts were delivered by TCO which started the tedious assembly of the measurement section. After four weeks the parts were assembled, sealed and tested for air tightness such that the measurement block could be assembled in the wind tunnel model. The newly designed open test section of the wind tunnel was used this time requiring the model to be positioned vertically. Also, the wake rake was installed this time to allow for a wake survey.

The experiments progressed far better than ever expected which allowed much more operating conditions to be tested than originally planned. High and low Reynolds numbers under free and forced transition conditions where measured revealing good agreement with reference data from Delft and simulations by XFOIL. Also, hysteresis phenomena at low Reynolds numbers at negative angles of attack were discovered during these experiments.

Following this brief review of the project I would like to take a moment here to express my gratitude to all people who helped me in one way or another:

Starting of all people with my supervisor Arne van Garrel. Thank you for the opportunity to work on this project and allowing me to give my own substance to the project. Your support and guidance during this project, although experimental work was not your main expertise, has been a tremendous help. Also, your enthusiasm and vast knowledge on (numerical) aerodynamics provided me with an indispensable source of motivation and information. I'd like to thank you for the nice discussions we had and the confidence you had in me.

Next I'd like to thank the EFD laboratory staff Walter Lette, Steven Wanrooij, Elise Leusink and Herman Stobbe for all the help with building of the wind tunnel model and during the experiments. Without your support, effort and advise the experimental activities in this work would not have succeeded the way they did. Also, thanks to Erik de Vries and Leo Tiemersma who provided indispensable advice and support in building the wind tunnel model for which I'm grateful.

[1] NMME: *Numerical Methods in Mechanical Engineering.* CFD: *Comutational Fluid Dynamics.*

The people at TCO did a tremendous job manufacturing the wind tunnel model and thanks Sib-Jan Boorsma and Pieter Post for your effort and the nice collaboration. I was fully aware the task was difficult and labour-intensive but you remained flexible and willing to always opt for the highest possible quality.

Thanks to all the scientific staff in the EFD department for the support and providing solicited and unsolicited advice. Special thanks to prof. Kees Venner for the opportunities in the project and for the assurance given when things didn't look to bright. Thank you for the effort of submitting request for a TGS grant in order to pursue a PhD. Although I didn't receive the grand I thank you for the confidence in me. Thanks to Leandro de Santana and Marijn Sanders for giving me the opportunity to join you to Deharde GmbH for the buy-off of your high-lift-device wind tunnel model. It was a very nice experience and gave me a lot of insight in professional wind tunnel model building. Also, thanks to Edwin van der Weide for his advice on grid convergence studies during the numerical phase in the project.

Designing the wind tunnel model would not have succeeded the way it did if it wasn't for my fellow student Sven van der Werf. More than once did you come up with smart idea's of which I didn't think early enough.

Lastly I want to thank my girlfriend Nienke for her continuous love, support, patience and faith in me during the thesis. And thank you mum and dad for allowing me the opportunity to re-enrol for a Master's program and for your unconditional support.

Thank you all.

Yorick.

Abstract

Transition from fossil-fuels as the prominent form of energy to renewable sources has led to the revival of wind turbines for large scale power production. Efficiency at which wind turbines convert the kinetic energy of the wind into electric power highly depends on the design of the turbine rotor blades. The process of designing rotor blades nowadays relies heavily upon numerical simulations using both panel codes (XFOIL) and Navier-Stokes solvers. Predictions using these numerical methods, within the region of their applicability, are in fair agreement with experimental data. However in regimes beyond aerodynamic stall and for very thick airfoils their predictions start to deviate significantly. As such, in these cases, no reliable data is available for further rotor blade design. Therefore the need to verify two-dimensional characteristics of airfoils outside the applicability of numerical methods using experimental techniques remains.

The wind tunnel of the Engineering Fluid Dynamics (EFD) group at the University of Twente (UT) is an open-jet closed-circuit wind tunnel. Airfoil models with a chord length up to 0.3 m which, together with a maximum jet velocity of 60 m/s at free stream turbulence intensities below 0.08%, enable chord based Reynolds numbers around 1 million to be reached in this tunnel. To further enhance the capabilities for aerodynamic research and education on (wind turbine) aerodynamics an instrumented airfoil model was desired.

An instrumented DU97-W-300 airfoil model representative for wind turbine applications is designed and manufactured at the UT. An experimental campaign measuring the aerodynamic characteristics such as lift, drag and moment is executed in the EFD wind tunnel facility. For deriving the aerodynamic lift force, surface pressures are measured using an array of pressure taps around the model perimeter. Wake velocities downstream the model are measured to determine the aerodynamic drag. The obtained data matches that available in literature such that the model is suitable for publishable research. Moreover, model manufacturing was accomplished completely at the UT presenting the aerodynamic experimental capabilities within the EFD group. Besides this work a two-dimensional numerical analysis is performed on the corresponding airfoil shape to asses the predictive accuracy of Navier-Stokes solvers with respect to panel codes and experimental data.

Contents

Nomenclature

Capital letters

A	Axial force
D	Total drag
D_p	Pressure drag
F	Force
H	Stagnation pressure / Boundary layer shape parameter (δ^*/θ)
L	Lift / Length scale
M	Moment / Molar mass
M_{LE}	Moment around the leading edge
$M_{c/4}$	Moment around the quarter chord point
N	Normal force / Number of elements
R	Gas constant
RH	Relative humidity
S	Span
U_∞	Free stream velocity
U_e	Boundary layer edge velocity

Greek symbols

α	Angle of attack
δ	Boundary layer thickness
δ^*	Boundary layer displacement thickness
Γ	Circulation
μ	Dynamic viscosity
ν	Kinematic viscosity
ρ	Mass density
τ	Shear stress
θ	Boundary layer momentum thickness / Surface angle airfoil with chord line

Coefficients

C_d	Total drag coefficient
C_f	Friction coefficient
C_l	Lift coefficient
C_p	Pressure coefficient
C_{dp}	Pressure drag coefficient
$C_{m\frac{1}{4}}$	Moment coefficient around the quarter chord point

Other symbols

c	Chord length
f	Solution functional
k	Roughness height

p	Pressure / Order of accuracy
q	Dynamic pressure $\frac{1}{2}\rho u^2$
t	Thickness
u, v, w	Velocity components in x, y, z direction
Ma	Mach number
Re	Reynolds number

1 Introduction

1.1 Motivation

The transition from fossil-fuels as the prominent form of energy to renewable sources has led to the revival of wind turbines for large scale power production. The efficiency at which wind turbines convert the kinetic energy of the wind into electric power highly depends on the design of the turbine rotor blades. In case of horizontal axis wind turbines (HAWT's) the rotor blades generate lift force leading to torque at the axis driving the electric generator. Proper rotor blade design for wind turbines is of vital importance for effectively generating power with little losses.

Wind turbine rotor blade design is the product of the combined effort of aerodynamic and structural engineering. The process of designing rotor blades nowadays relies heavily upon numerical simulations in case of both disciplines, each relying on their respective tools for predicting characteristics. Different numerical techniques exist for the aerodynamic analysis of rotor blades varying from rather simple models such as the *Blade Element Method (BEM)* to more complicated ones utilizing *Computational Fluid Dynamics (CFD)* codes. Simple models are attractive as the computational requirements are low but when more details of the flow are required they fail to deliver reliable results. CFD, in its various implementations, can predict rather complicated flow phenomena. However, the computational cost is very high such that these techniques are limited for evaluation rather than conceptual designs.

Flow over the large and slender blades of a wind turbine rotor may (under given circumstances) be simplified as two-dimensional. At given span-wise locations the flow is deemed two-dimensional allowing solely the blade cross section, or *airfoil*, to be analysed. Airfoils used in rotor blades vary depending on their location. Sections close to the rotor hub are thick for structural requirements while airfoil at the tip are thin to achieve high lift. Numerical predictions of two-dimensional airfoil performance allow rotor blade engineers to quickly design the most suitable sections for use in their concepts. At present most airfoils are designed using so called *panel codes* of which XFOIL is by far the most used.

XFOIL is developed by Mark Drela at the Massachusetts Institute of Technology (MIT) in 1986 and is a two-dimensional panel (or Boundary Element Method[1]) code with a strong viscid-inviscid interaction scheme allowing the prediction of realist boundary layer properties. It is used heavily in the conceptual design of airfoils in favour of CFD due to is minor computational requirements and ease of use.

CFD codes commonly solve the *Reynolds Average Navier-Stokes (RANS)* equations on a computational grid covering a chosen fluid domain. The processes of defining an accurate airfoil geometry, generating a suitable computational grid, choosing the correct boundary conditions and turbulence model and finally solving the equations is labour and computationally intensive.

The numerical predictions of XFOIL, within the region of its applicability, are in fair agreement with experimental data. However, in regimes beyond aerodynamic stall and for very thick airfoils its predictions start to deviate significantly from experiments. Therefore, in these cases, no reliable data is available for further rotor blade design. Neither RANS based CFD codes posses the possibility to accuracy predict performance of stalled airfoils such that either high fidelity CFD schemes or experiments are required. The need to verify two-dimensional characteristics of airfoils with experiments therefore remains.

1.2 Research objective

The wind tunnel of the Engineering Fluid Dynamics (EFD) group at the University of Twente (UT) is an open-jet closed-circuit wind tunnel. It is designed in the 1970s, is converted to an aeroacoustic tunnel in 2001 [66] and upgraded further in 2018 [12]. The facility allows for aeroacoustic and aerodynamic measurements on objects for which both an open and closed test section are available. The open test section combined with the anechoic chamber is required for the free-field conditions necessary for research on flow-induced noise. Generally in such experiments microphones are placed in the direct acoustic field but outside the airflow allowing one to resolve the radiated noise levels and their directivity.

[1] The term *panel code* is customary in wind turbine design as the acronym of the Blade Element Method is identical.

In case of aerodynamic research the anechoic chamber is not necessarily required. The facility's size however allows for airfoil models with a chord length up to 0.3 m which together with a maximum jet velocity of 60 m/s allows chord Reynolds numbers around 1 million to be reached. Low free stream turbulence intensities below 0.08% are obtained at maximum velocity and the flow is temperature controlled by a water/air heat exchanger. The wind tunnel is designed for both fundamental and applied research together with support for eduction of bachelors and masters students. To further enhance the capabilities for aerodynamic research and eduction on (wind turbine) aerodynamics an instrumented airfoil model was desired.

The objective of this research was to design and manufacture a wind tunnel model of an airfoil representative for wind turbine applications together with the experimental campaign measuring the aerodynamic characteristics. To determine the forces acting on the airfoil surface pressures were to be measured together with the velocities in the wake. Obtained characteristics would need to match those available in literature such that the model is suitable for publishable research. Moreover, the model had to be manufactured in a cost effective manner.

1.3 Outline

Background on two-dimensional wind tunnels testing is discussed in the Chapter 2 together with information on airfoil designs for wind energy applications. A brief background on fluid dynamics and aerodynamics is given in Chapter 3 such that the reader is able to understand further terminology in the report. Wind tunnel model design and construction are discussed in detail in Chapter 4. This section also discusses the reference aerodynamic characteristics obtained from literature and used for validation of experiments. The experimental work is completely discussed in Chapter 5. The test setup including equipment specifications, data reduction equations, discussion on the tripping device, experimental procedure and measurement results are explained in detail in this section. Chapter 6 sets out the numerical work including the problem description, solution verification and final results. Results of both the experimental campaign and numerical work are compared in Chapter 7 including an analysis on the discrepancies between data. Lastly conclusions with respect to the project and recommendations for improvements are drawn in Chapter 8.

2 Background and literature survey

The gathering of experimental information for solving aerodynamic problems can be accomplished in a number of ways. Wind tunnels are able to provide this information on models in early phases of design cycles. They allow testing under conditions similar as experienced on full scale and can provide large amounts of reliable and reproducible data. Wind tunnels have been used since the end of the 19^{th} century for the purpose of determining lift and drag of bodies moving trough air. As the science of aerodynamics was established further, due to advancements in air travel, the use of wind tunnels for experimental research increased considerably.

2.1 Two dimensional wind tunnels and model construction

The seemingly first use of wind tunnel experiments on two-dimensional wing sections dates back to the 1940s. Von Doenhoff and Abbott [14] discuss the Langley two-dimensional low-turbulence pressure tunnel which was particularly suited for research on the effects of basic shape variables of airfoils. The tunnel was a single-return closed throat tunnel which could be pressurized up to 10 bar. The maximum chord length of airfoil models used was 24 inch (0.61 m) allowing chord Reynolds numbers up to $9{\times}10^6$ to be tested. Airfoil models completely panned the tunnel such to assure two-dimensional flow as good as possible and were oriented horizontally (Figure 2.1).

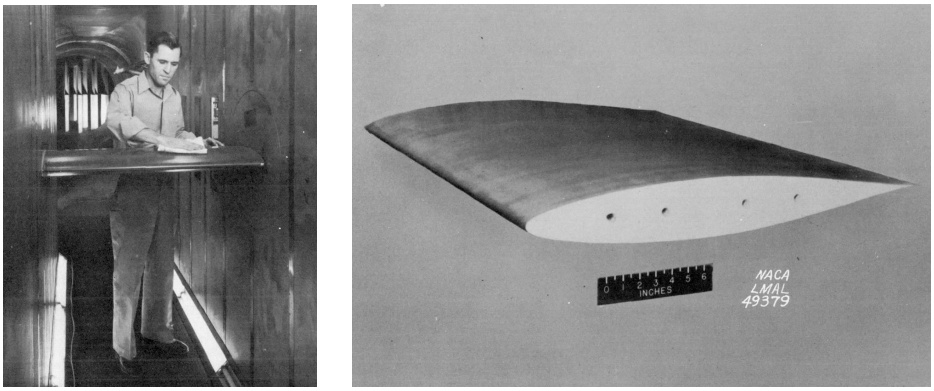

Figure 2.1: An Aifoil model mounted in the Langley two-dimensional low turbulence tunnel (l) and a 24 inch chord model of a NACA 64_2-215 airfoil used in the tunnel (r). Pictures courtesy of [14]

Most experimental airfoil data in the well known reference work of Abbott and von Doenhoff [1] was measured in this tunnel and (possibly because of this) many wind tunnel experiments today are heavily based on this setup. To measure the aerodynamic forces in a two-dimensional wind tunnel multiple methods exists:

- Models can be mounted on a *force balance system* which measured forces and moments directly using load cells. The balance is calibrated against known forces and moments prior the experiments and the output commonly needs corrections for interference effects of the wind tunnel walls. Lift, drag and aerodynamic moment can be measured semi-directly using the balance and provide the net results of the combined effects of pressure and viscous forces. A comprehensive discussion of balance systems is presented in the book of Barlow (1999) [7].
- An alternative method of deducing the aerodynamic lift of a two-dimensional airfoil is by means of measuring *tunnel surface pressures*. As an airfoil generates lift it induces an equal and opposite reaction upon the wind tunnel ceiling and floor[1]. By integration of the pressure distribution along the floor and ceiling the lift may be deduced [14].

[1] When mounted horizontally. A prerequisite for this method is that the model is situated in a confined space.

- Next method for measuring aerodynamic lift and (pressure) drag is by integration of the surface *pressure distribution around the object* under test. To this end the airfoil is equipped with an array of pressure taps distributed around the perimeter allowing integration of the surface pressure.

- Aerodynamic drag is generally measured using a so called *wake survey* in which an array of total pressure probes is placed downstream such to measure the momentum deficit in the flow due to presence of the object. Integration of the total pressure measurements allows determination of the drag.

Depending on the tunnel type, data requirements from the experiments and measurement techniques employed tunnel scale models are being constructed in various ways. A comprehensive discussion is given by Norton [41] on the construction of wind tunnel models for tunnels of the National Advisory Committee for Aeronautics (NACA) in the 1920s .

Thin airfoil sections were generally made of a light aluminium allow as opposed to wood to maintain geometrical accuracy during tests, however for thicker airfoils wood was used rather frequently. Wooden airfoils of constant cross section where manufactured from blocks of laminated maple of which the shape was crafted manually using a special saw table. Metal airfoils where either crafted from aluminium by hand (using filing) or from brass or steel which allowed using milling machines to which the raw material was soldered. Other, more rapid though less permanent, manners of constructing airfoils was by means casting calcined plaster ("*gips*" or "*pleister*" in Dutch) or certain types of wax.

When surface pressures around the airfoil were to be measured, brass or steel airfoils were used in which a series of grooves was cut along the span. Hypodermic tubing was then placed in each groove and smoothed with the surface using solder. Holes were then drilled at the desired positions opening the covered tubing to the surface.

Fiber-reinforced plastics started to emerge as a construction material for wind tunnel models in the 1970s. Llewelyn-Davies [35] lays out the process of producing wind tunnel models using CFRP's[2]. The publication shows that this manufacturing technique allows for a shell type construction in which much instrumentation can be fitted without compromising on structural rigidity. Dimensional accuracy was found sufficient for use on airfoil models. As such this technique is nowadays heavily used on complex models requiring much instrumentation as shown by the Royal Netherlands Aerospace Centre (NLR) [40, 39].

The advances in *computer numerically controlled (CNC) machining* allowed for complex shapes to be made entirely from solid blocks. These techniques nowadays allow extreme tolerances to be obtained which are required typically for use in supersonic, hypersonic or cryogenic wind tunnels.

Rapid development of *additive manufacturing techniques* (3D printing) allows for rapid prototyping (RP) of models which, depending on the technique used, are suitable for wind tunnel testing. Landrum et al. and Springer [32, 57] are one of the first to publish comparative research in 3D printing of wind tunnel models. They found that surface quality of printed parts had a large influence on the measured aerodynamic performance and that the structural properties of RP materials limited these models to preliminary, low-speed, design studies. Surface finish of printed parts should therefore be improved by manual sanding or painting as shown by Traub and Aghanajafi et al. [61, 3] together with using the thinnest possible layer thickness during printing. The reduction in lead times for model manufacturing is considerable when using RP-techniques (Tyler et al.) [62] which popularized the technique heavily in educational settings (Kroll and Artzi) [29]. Also, the ability to easily manufacture complex models for measuring surface pressures (Heyes and Smith) [24] or for testing aerodynamic control techniques (Shun and Ahmed) [55] makes 3D printing a promising manufacturing method for wind tunnel models.

If a large amount of experiments based on a single airfoil design are required profiles made by *extrusion* can economically be feasible. Examples of extruded profiles can be found in the EFD group at the University of Twente where large profiles of the NACA 0018 airfoil are present.

A rather exceptional material for models is used the automotive industry where *clay* is a preferred material for the construction of models for use in wind tunnels. As Reynolds numbers and aerodynamic loads in automotive applications are much lower less emphasis on structural integrity of the models is required.

[2]Carbon Fibre Reinforced Plastics

2.2 Airfoils for wind turbine applications

Wind turbine performance is predominantly determined by the efficiency at which the blades convert kinetic energy from the wind to torque around the rotor axis. In horizontal axis wind turbines (HAWT) aerodynamic *lift*, L, acting on the blades is the force responsible for torque development resulting in power generation by the turbine. A resisting *drag*, D, force opposing the motion of the blades is generated as well. A rotor blade yielding a high lift and low drag force, thus a high lift-over-drag ratio (L/D), is desired for wind turbine applications. Figure 2.2 shows a typical rotor blade together with the forces acting on both the root and tip section.

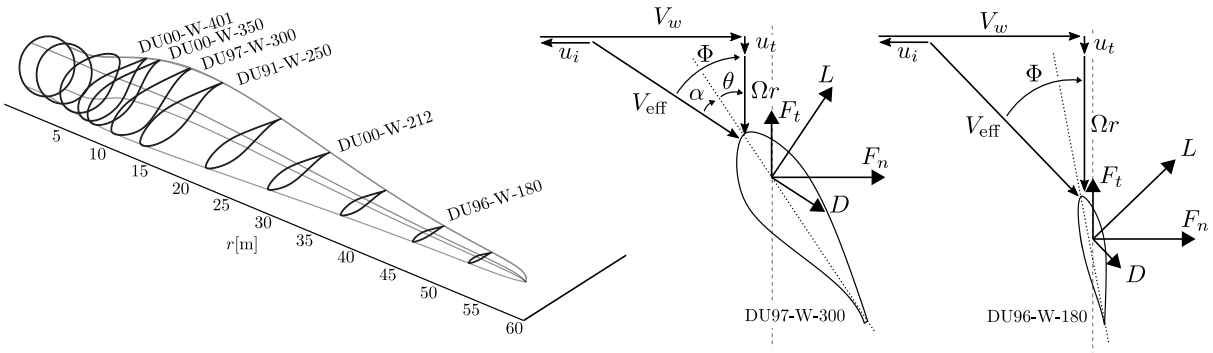

Figure 2.2: A typical rotor blade highlighting the different airfoil sections (l) including the aerodynamic forces acting in the root section (m) and tip section (r) of the blades.

Airfoils for wind turbine applications have different requirements than those used in aviation industry as they operate in different environments and are subject to different mechanical loading. Some differences between aviation airfoils and wind turbine airfoils are (from Schubel and Crossley [53]):

- *Roughness sensitivity.* The low altitude operation of wind turbines causes insects and other particles to foul the blades. As aircraft fly at high altitudes no prerequisites are taken for possible performance degradation due the effects of soil build-up. Standard aviation airfoils (NACA 44 and 63 series), or scaled versions of them, used in early wind turbines have been found susceptible to so called fouling, especially contamination of the leading edge [60, 9]. Tangler and Somers [59], Björk [8], Timmer and van Rooij [60], Fuglsang and Bak [21], van Dam [63] and Miller et al. [37] all developed profiles that are less sensitive to leading edge contamination for use in wind turbine blades.
- *Structural requirements.* Wind turbine blades are significantly longer than aircraft wings requiring airfoils of high thickness-to-chord ratios ($t/c > 0.27$) to be used in the root sections. Such thick airfoils are seldom used in the aviation industry as they generally have a lower lift-over-drag ratio. To circumvent this problem special design considerations are required. Profiles designed for root sections of wind turbine blades are generally characterised by blunt trailing edges, a so-called "flatback" design, which reduces the adverse pressure gradient and increases structural integrity ([59, 8, 60, 21, 63, 37]).
- *Geometric compatibility.* The change in thickness-to-chord ratio over the span requires airfoils of varying t/c to blend in smoothly along the span. The chord-wise location of maximum thickness and the curvature at the leading edge can be constrained to allow for smooth transition between airfoils (Fuglsang and Bak [21]).

Requirements which are more-or-less common between aviation and wind energy type airfoils are:

- A *high design* C_l[3] *near* $C_{l,\max}$. Especially airfoils designed for the blade tip section, where the tangential force component is relatively mall, a high design C_l increases power extraction efficiency (see Figure 2.2). To account for the stochastic nature of wind off design operation is to be considered and in most cases the design C_l is designed close to $C_{l,\max}$. This prevents excessive loading during wind gusts [60] and ensured a high C_l/C_d for angles of attack below stall [21]. Moreover small chord lengths can be used leading to lower storm loads [60].

[3] C_l at the point of $(C_l/C_d)_{\max}$.

- *Gentle post stall characteristics.* Traditional stall controlled wind turbines rely on aerodynamic stall for speed control. To prevent large stall-induced blade vibrations yielding high dynamic loading C_l post-stall should not drop too suddenly. Such a requirement generally dictates a lower $C_{l,\max}$ impeding high power extraction. However most modern pitch controlled wind turbines typically do not operate in stall such that higher $C_{l,\max}$ at some expense of "gentleness" [21].
- *Low aeroacoustic noise generation.* As wind turbines are increasingly placed in inhabited area's the noise emitted from rotor blades, which is a broadband trailing edge noise, should be minimal. Blade tip sections generally emit the highest noise levels as the free stream flow velocity is highest and the dominant parameter for noise emission [21] (Figure 2.2). The airfoil shape determines the trailing edge boundary layer thickness and can be designed for the most acute conditions for the generation of noise.

Fuglsang and Bak [21] and van Rooij [64] both give an overview of desirable airfoil characteristics for use in wind energy applications (Table 2.1)

Table 2.1: Properties considered desirable for airfoils in wind turbine applications with their importance in difference blade regions [21, 64].

	Root	Mid part	Tip
Thickness/Chord ratio (t/c)	$> .27$	$.27 - .21$	$.21 >$
High max lift/drag ratio (C_l/C_d)	+	++	+++
Max. C_l and gentle post stall		+	+++
Roughness sensitivity on max. C_l	+	+	+++
Low noise			+++
Geometric compatibility	++	++	++
Structural demands	+++	++	+
Design C_l near max. $C_{l,\text{off design}}$		+	+++

3 Aerodynamic theory and concepts

3.1 Fluid dynamics

Before the concepts and theory of aerodynamics is explained a brief introduction on fluid dynamic concepts is given. The Reynolds number, essential for distinguishing flow characteristics, is explained after which viscous and inviscid flow are discussed followed by the connecting element between the two flow types, the boundary layer. The concepts of viscosity, boundary layer thicknesses, transition and separation are treated as well. Full derivations of the fluid dynamic equations (e.q. Navier-Stokes, Prantl Boundary layer equations etc.) are omitted here. For an in-depth treatment of this theory the reader is referred to specialized books on fluid dynamics [11, 25, 31]

3.1.1 Reynolds number

The Reynolds number is a ratio of two forces acting within a fluid resulting in certain distinguishable flow patterns, *viscous forces* and *interia forces*. This ratio arises naturally when writing the conservation equations for fluids in a dimensionless form by scaling. The conservation of mass and momentum for a fluid (Navier-Stokes equations) can be written in these forms as follows[1] :

$$\rho \frac{\partial u_i}{\partial x_i} = 0 \quad \rightarrow \quad \frac{\partial \bar{u}_i}{\partial \bar{x}_i} = 0 \tag{3.1}$$

$$\underbrace{\rho \frac{\partial u_i}{\partial t} + \rho u_j \frac{\partial u_i}{\partial x_j}}_{\substack{\text{Advective acceleration} \\ (ma)}} = \underbrace{\frac{\partial p}{\partial x_i} + \mu \left(\frac{\partial^2 u_k}{\partial x_k^2} \right)}_{\substack{\text{Forces} \\ (F)}} \quad \rightarrow \quad \frac{\partial \bar{u}_i}{\partial \bar{t}} + \bar{u}_j \frac{\partial \bar{u}_i}{\partial \bar{x}_j} = \frac{\partial \bar{p}}{\partial \bar{x}_j} - \frac{1}{\mathrm{Re}_L} \left(\frac{\partial^2 \bar{u}_k}{\partial \bar{x}_k^2} \right) \tag{3.2}$$

With (3.1) the conversation of mass and (3.2) the conservation of momentum. The equations are written using Einstein's summation convention where $u_{(i,j,k)}$ are the velocity terms and $x_{(i,j,k)}$ are the spatial terms in x, y, z direction $(i, j, k \in [x, y, z])$. The density is denoted by ρ and the dynamic viscosity μ. The over bars in the right equations $(\bar{})$ indicate dimensionless variables obtained by scaling. The term Re_L indicates the *Reynolds number*[2] and is defined as:

$$\mathrm{Re}_L \equiv \frac{\rho U L}{\mu} = \frac{UL}{\nu} = \frac{\text{Inertial forces}}{\text{Viscous forces}} \tag{3.3}$$

Where U is a reference velocity for scaling, in case of aerodynamics this usually is the free stream velocity flowing around the object to be studied. L is an appropriate length scale for the matter at hand which for aerodynamics commonly is the objects length. $\nu = \mu/\rho$ is the kinematic viscosity of the fluid. The implication of the Reynolds number causes the conservation of momentum equation (3.2) to approach two distinct forms depending its value: Equations for viscous and inviscid flows.

3.1.2 Viscous and inviscid flow

For $\mathrm{Re}_L \ll 1$ viscous forces dominate the flow as $\nu \gg (UL)$. One may then rather safely simplify the momentum equation by neglecting the advective acceleration terms all together (left-hand-side of (3.2)) resulting in the mass and momentum equations for viscous flows known as Stokes flow:

$$\frac{\partial u_i}{\partial x_i} = 0 \quad \text{and} \quad \frac{\partial p}{\partial x_i} = \mu \frac{\partial^2 u_k}{\partial x_k^2} \tag{3.4}$$

For $\mathrm{Re}_L \gg 1$ the flow is dominated by inertial forces as $(UL) \gg \nu$. Now the momentum equation can be simplified differently by neglecting the viscous force terms $(\partial^2 u_k)/(\partial x_k^2)$ yielding the inviscid momentum

[1] This discussion limits itself to flows of constant density (ρ = constant), constant viscosity (μ = constant), constant entropy (s = constant) and neglecting the effects of gravity ($g_i = 0$). Only Newtonian fluids are considered ($\lambda = -(2/3)\mu$)

[2] After Osborne Reynolds (1842-1912)

equations known as the (incompressible) Euler equations:

$$\frac{\partial u_i}{\partial x_i} = 0 \quad \text{and} \quad \frac{\partial u_i}{\partial t} + u_j \frac{\partial u_i}{\partial x_j} = \frac{1}{\rho} \frac{\partial p}{\partial x_i} \tag{3.5}$$

The significance of these two types of flow becomes apparent when one wants to describe the external fluid motion around objects either far away or close to the object at hand.

Inviscid flow

The flow far away from an object can be considered inviscid as the effects of frictional forces in the fluid are negligible for describing its velocity components in the domain. Inertial forces play a much larger role in "shaping" the flow field such that this region can be described fairly accurate using the Euler equations (3.5).

Further simplification of the Euler equations can be achieved by assuming the flow to behave *irrotational*, meaning the circulation Γ anywhere in the flow equals zero ($\Gamma = 0$, see Section 3.2.2). One can show that a irrotational flow implies that the curl of the velocity field equals zero ($\nabla \times \boldsymbol{u} = 0$) which allows the field to be written as the gradient of a scalar function[1] $u_i = (\partial\phi)/(\partial x_i)$ termed a *potential function* ϕ. The consequence of this is a further simplification to the equations yielding the potential flow equations for mass and momentum conservation respectively:

$$\frac{\partial^2 \phi}{\partial x_i^2} = 0 \quad \text{and} \quad \frac{\partial \phi}{\partial t} + \frac{u_i u_j}{2} = -\frac{p}{\rho} + f(t) \tag{3.6}$$

The conservation of mass equation equals the heavily studied Laplace equation for which many elementary solutions exist. Superimposing a multitude of these solutions allows one to model a vast variety of flow fields that may be assumed inviscid, such as external flows around objects. In the study of aerodynamics much use is made of software codes utilizing this technique (XFOIL, see section 3.3). For further details on the study of potential flow the reader is referred to the book of Katz and Plotkin [27].

Viscous flow

Close to solid boundaries the approximation for inviscid flow does not hold. Viscous friction forces imposed on the fluid by the solid boundary causes the flow to adhere and retard. No slip is present between the surface and fluid which is the key reason why moving objects in fluids experience a resisting force along the stream wise direction, *drag*. As the fluid adheres to the surface its velocity changes from zero at the surface to the free stream velocity U_∞ away from the surface. The region in which this velocity gradient persists is termed the *boundary layer*.

3.1.3 Boundary layer

The magnitude of shear stress acting on a surface, given by Newton's law of friction, is proportional to the dynamic viscosity μ and the velocity gradient at the wall which in a two-dimensional case reads:

$$\tau = \mu \frac{\partial u}{\partial y} \tag{3.7}$$

The magnitude of the dynamic viscosity in air rather small ($\mu \approx 1.81 \times 10^{-5}$ Pa s at 20°C). However at very large fluid velocities the velocity gradient $\partial u/\partial y$ increases significantly in the boundary layer. Shear stresses therefore become non-negligible resulting in a significant force resisting the motion of the object. At the "start" of the object just downstream of the *stagnation point* the velocity gradient in the boundary layer is largest. Further downstream flow more away the wall retards causing the boundary layer thickness $\delta(x)$ to increase as schematically shown in Figure 3.1.

The increase in thickness occurs as the loss of momentum by the no-slip condition at the boundary diffuses into the stream. In other words, as the fluid flows over the surface more and more fluid particles normal to the stream-wise direction are affected by the friction force of the stationary surface. These particles are retarded resulting in a reduction of the velocity gradient over the boundary layer which lowers the shear stress and increases the boundary layer thickness.

[1] Due to the mathematical identity $\nabla \times \nabla\phi = 0$ with ϕ a scalar function.

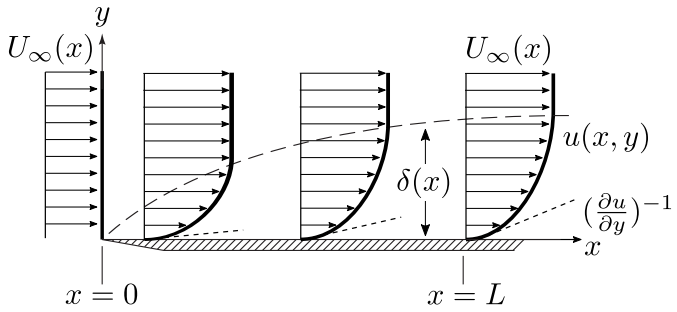

Figure 3.1: Schematic representation of the boundary layer near a solid wall

Displacement and momentum thickness

As the stream-wise velocity varies asymptotically from zero, at the surface, to the free stream velocity U_∞, far away, no definite value for the boundary layer thickness can be defined based on U_∞. The usual convention however is to designate the boundary layer thickness δ as the distance at which the stream wise velocity equals 99% of the free stream velocity, $\delta = 0.99U_\infty$ (see Figure 3.2). As this distance is hard to measure experimentally, and the 99% is rather arbitrary, more precise definitions for boundary layer thickness are given based on mass and momentum conservation.

Displacement thickness

The *displacement thickness* of the boundary layer, denoted δ^* is defined as the distance by which the surface needs to move outward in a theoretically inviscid flow to maintain the volume flux of the original viscous flow. Another description would be the distance the outer streamline is displaced outward by the presence of the boundary layer. The decrease in volume flux per unit width is expressed as the velocity loss with respect to the free stream velocity integrated over the boundary layer $\int_0^\infty [U_e(x) - u(x,y)]\, dy$ the displacement thickness δ^* is therefore defined as follows:

$$\delta^*(x)U_e(x) = \int_0^\infty [U_e(x) - u(x,y)]\ dy \quad \rightarrow \quad \delta^* \equiv \int_0^\infty \left[1 - \frac{u(x,y)}{U_e(x)}\right]\ dy \tag{3.8}$$

Momentum thickness

The loss of momentum in the actual flow due to the presence of the boundary layer and is called appropriately the *momentum thickness* denoted by θ. The loss of momentum (per unit width) resulting from the boundary layer is $\rho \int_0^\infty u(x,y)\,[U_e(x) - u(x,y)]\, dy$ yielding the following definition for the momentum thickness θ

$$\rho U_e^2(x)\theta = \rho \int_0^\infty u(x,y)\,[U_e(x) - u(x,y)]\ dy \quad \rightarrow \quad \theta \equiv \int_0^\infty \frac{u(x,y)}{U_e(x)}\left[1 - \frac{u(x,y)}{U_e(x)}\right]\ dy \tag{3.9}$$

Both these thickness definitions are functions of the shape of the velocity profile $u(x,y)$ such that thier ratio, the *momentum shape parameter* $H = \delta^*/\theta$ is a commonly used shape factor to characterize boundary layers

3.1.4 Laminar and turbulent flow

Fluid flows exist in two different regimes: One where fluid particles flow in an orderly fashion adjacent to each other with no interchange of mass between layers of fluid. This regime is termed *laminar flow*. The shear stresses between fluid layers due to their velocity difference are solely dependent on the viscosity of fluid. In order words, the transfer of momentum between fluid layers takes place on a molecular scale only.

The second flow regime is termed *turbulent flow* and is characterised by random velocity fluctuations both in and normal to the stream wise direction leading to intense cross stream mixing. Velocity variations in the direction normal to the undisturbed flow cause large mass transfers between the fluid layers yielding extra momentum exchange. Shear stresses by mass transfer between layers can be several orders of magnitudes larger than the stress due to viscosity alone and are termed *Reynolds stresses*.

As Reynolds stresses cause larger momentum transfer from the upper regions of the boundary layer to the lower regions the mean boundary layer velocity profile becomes more uniform. However as the fluid closest to the surface still adheres to it, the velocity gradient at the surface increases considerably resulting in significant increase in surface shear stress $\tau_w = \mu(\partial u/\partial y)_{y=0}$ as shown in Figure 3.2.

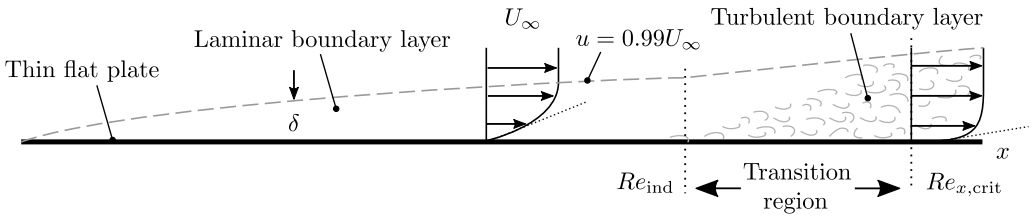

Figure 3.2: Schematic representation of boundary layer development over a flat plate.

Transition and separation

Transition

Laminar to turbulent transition of the boundary layer may be distinguished in three types as discussed by White [67]: *i*) *Natural transition*, *ii*) *Bypass transition* and *Separated-flow transition*.

Natural transition is the process where flow disturbances turn into low-amplitude *Tollmien-Schlichting* waves superimposed onto the main flow and propagate in the boundary layer. Disturbances grow to form three dimensional waves followed by vortex breakdown, turbulent spots and eventually fully turbulent flow as shown in Figure 3.3. Whereas *bypass transition* may occur when the boundary conditions of the flow are "noisy and rough" (e.g. rough walls, whirring free stream or a vibrating surface). Early stages of natural transition are bypassed and the natural instabilities immediately form vortex breakdowns leading to fully turbulent flow.

Separated-flow transition is the term used for transition occurring after a laminar boundary layer separates forming a laminar separation bubble (see below). The separation initiates instability yielding transition. The resulting turbulent boundary layer commonly reattaches due to the gained momentum by mixing (see below).

A fourth type of transition may be distinguished termed *forced transition* in which the flow is intentionally disturbed by some form of artificial roughness. For a high enough roughness particle the initiated disturbances immediately result in fully turbulent flow (see Section 5.3.5).

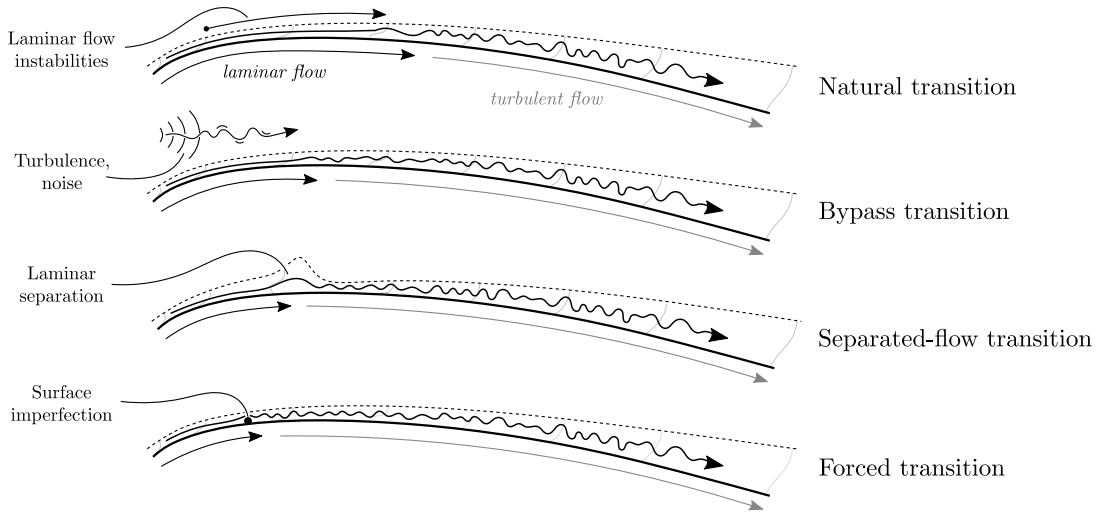

Figure 3.3: Schematic drawing of four types of laminar-to-turbulent transition of the boundary layer.

Transition occurs with a significant increase in boundary layer thickness coupled with a strong change in velocity profile shape. Next to that a strong decrease in the shape factor $H = \delta^*/\theta$ is observed. In case of a flat plate boundary layer $H \approx 2.6$ in the laminar part of the boundary while and drops to $H \approx 1.4$ after transition [52].

Separation

Figure 3.4 shows air flowing over an airfoil resulting in varying local pressure gradients over the top (*suction*) side of the airfoil. The local pressure gradient becomes positive around the point of maximum airfoil thickness. In this adverse pressure gradient the flow is retarded and the shape of the velocity profiles become more and more concave. At some point the velocity near the surface stagnates and forms a *separation point* from which detachment of the boundary layer is initiated. At the separation point the velocity gradient normal to the surface is zero ($(\partial u/\partial y)_{y=0} = 0$) and further downstream flow reversal takes place as the boundary layer is separated from the surface.

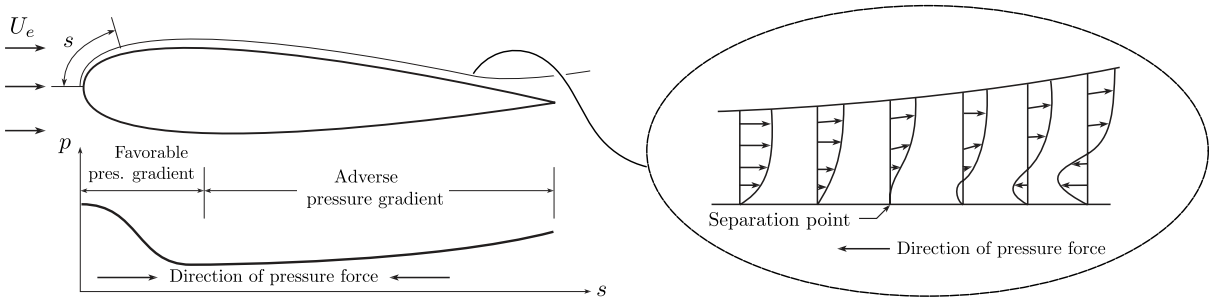

Figure 3.4: Schematic overview of boundary layer separation occurring in the aft region of an airfoil.

The result of boundary layer separation is an effective increase in profile thickness as low-energy recirculatory flows form downstream the separation point. This region of separated flow is termed the *wake*. In the wake no pressure recovery takes place resulting in a nearly constant pressure considerably lower than the total pressure. The formation of the wake increases the pressure unbalance in stream wise direction on the airfoil. This increase in pressure unbalance yields a drag force counteracting the direction of motion which is termed *form drag*. As the separation point moves towards the leading edge due to an increase in angle of attack the size of the wake increases forming a larger region of reduced pressure which further increases drag considerably.

Laminar separation bubble

In low Reynolds number flows over airfoils the laminar boundary layer may separate due to an adverse pressure gradient and form a *laminar separation bubble*. After the point of separation S (Figure 3.5), flow in the free shear layer becomes unstable and transitions to turbulent flow at T. Momentum transfer by mixing of the turbulent shear layer with the boundary layer eliminates the recirculation region allowing the flow to reattach at point R.

The enclosed zone in which flow recirculates displaces the outer streamlines, thereby substantially thickening the boundary layer locally yielding increased drag. Little mass or momentum exchange occurs between the bubble and free shear layer stabilizing the bubble and preventing is from "bursting". The pressure inside the "bubble" is practically constant resulting in flattening of an airfoils pressure distribution (see Section 3.2.3) at the bubble location.

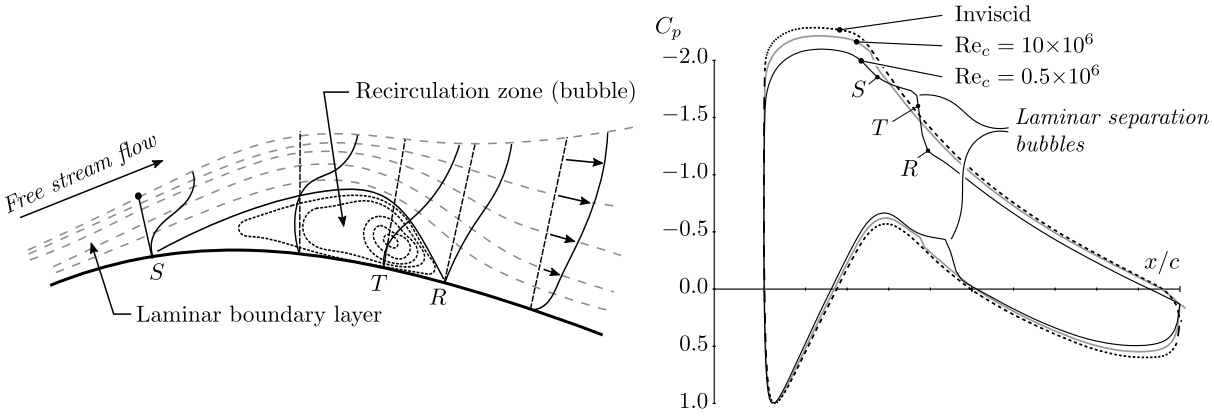

Figure 3.5: (l) Schematic overview of a laminar separation bubble. (r) Airfoil pressure distributions showing the laminar separation bubble occurring at low Reynolds numbers.

3.2 Aerodynamics

This section will lay out the basic aerodynamic concepts of airfoils used within this report. Airfoil nomenclature is discussed as well as the formation of lift and drag forces due to the movement of fluid around it. Next to that typical performance graphs are explained to assist the reader in understanding the subsequent sections.

3.2.1 Airfoil nomenclature

Wings or wind turbine rotor blades are bodies designed to produce a force normal to the flow direction due to fluid flowing around it. Cross sectional areas of any wing or blade are termed wing sections or *airfoils*. The angle at which the relative velocity U_{rel} approaches an airfoil is termed the *angle of attack* α. The distance between the front of the airfoil, the *leading edge* and the rear, the *trailing edge*, is termed the *chord length* 'c'. Most other measures are expressed in terms of this length. Maximum thickness' 't' of most airfoils lies between $0.25x/c$ and $0.5x/c$. In aerospace applications thickness ratios of over $0.18t/c$ are rare, however in wind turbine application thickness ratios up to $0.40t/c$ are used in the root sections of the rotor blades.

Airfoils are either symmetric or have some level of *camber*, in other words they are curved. The *camber line* is the locus of points midway between the upper and lower surface. The maximum camber line height is again expressed in terms of chord length.

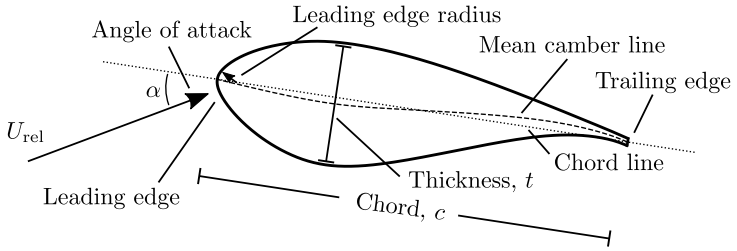

Figure 3.6: Airfoil nomenclature.

3.2.2 Aerodynamic forces

Circulation and lift

To introduce aerodynamic *lift* a brief introduction of the concept of *circulation* is given. The circulation Γ of a velocity field $\boldsymbol{u}(\boldsymbol{x}, t)$ is defined as the path integral of the tangential velocity around a closed curve:

$$\Gamma(C) = \oint_C \boldsymbol{u} \cdot \boldsymbol{\tau} ds \tag{3.10}$$

with $\boldsymbol{\tau}$ the tangential unit vector along the curve C and ds the differential line segment along C. A large number of flow fields in real life are irrational ($\Gamma = 0$). Circulation however is the primary cause of pressure unbalance around and object in a velocity field resulting in a lift force perpendicular the free stream direction. airfoils are bodies specifically designed to impose circulation on a velocity field in which they are suspended.

As fluid in a two-dimensional flow field starts to move over an airfoil two *stagnation points* are formed. The streamline approaching the airfoil "head-on" ends in the front stagnation point. A stream leaving the airfoil surface is always located at the trailing edge. Streamlines moving around the airfoil follow these streamlines in close proximity assuming no flow separation.

Inviscid flow theory is matched to this observed flow phenomena by stating that the right amount of circulation Γ on the flow is induced by the airfoil to move the rear stagnation point to the trailing edge - this is termed the *Kutta condition*. Analysing inviscid flows around airfoils to which the Kutta condition is applied yields very good agreements with observed flow patterns and pressure distributions. The lift per unit span of a wing is then given by the *Kutta-Joukowski theorem*,

$$L = -\rho U_\infty \Gamma \tag{3.11}$$

Aerodynamic coefficients

A body submerged in a flowing fluid is subject to two kinds of forces; a *pressure distribution* over the surface p, acting normal to the body surface, and a *shear stress distribution* τ acting tangential to the surface (Figure 3.7(a)) as explained by Anderson (2011) [5] . The net result of the pressure and shear stress distributions is a resultant aerodynamic force R and moment M as shown in Figure 3.7(b). One can decompose the force in two sets of components related to different reference frames as shown in Figure 3.7(c). In the airfoil reference frame the force N is normal to the chord and the axial force A is parallel to it. In the stationary reference frame we define the *lift* L as the force normal to the free stream direction U_∞ and the *drag* D parallel to it.

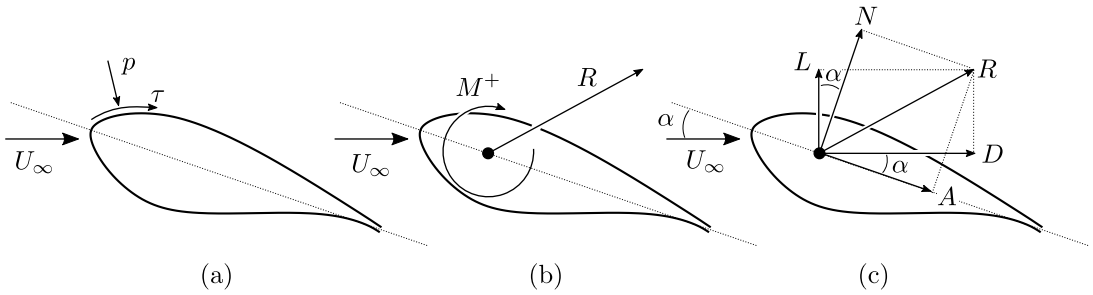

Figure 3.7: Origin of aerodynamic forces and moment acting on an airfoil.

Between the two coordinate systems the following relations exists:

$$L = N\cos\alpha - A\sin\alpha \tag{3.12}$$

$$D = N\sin\alpha + A\cos\alpha \tag{3.13}$$

The normal N and axial A force are evaluated from the airfoil surface pressure and shear stress distribution by integration over the upper and lower surface, explained in the next section. As forces acting on an airfoil depend on the free stream velocity U_∞ and the fluid density ρ they can be made dimensionless by considering the *dynamic pressure* q_0:

$$q_0 \equiv \frac{1}{2}\rho U_\infty^2 \tag{3.14}$$

such that the dimensionless forces or, *aerodynamic coefficients*, per unit span $S = 1$, become:

$$\text{Lift coefficient} : C_l \equiv \frac{L}{q_0 c}, \quad \text{Drag coefficient} : C_d \equiv \frac{D}{q_0 c}, \quad \text{Moment coefficient} : C_m \equiv \frac{M}{q_0 c^2} \tag{3.15}$$

Next to these force coefficients, pressure and shear stresses are generally made dimensionless as well:

$$\text{Pressure coefficient} : C_p \equiv \frac{p - p_0}{q_0}, \quad \text{Friction coeficient} : C_f \equiv \frac{\tau}{q_0} \tag{3.16}$$

3.2.3 Lift, drag and moment from pressure and shear stress distributions

The primary way of describing the characteristics of airfoils is by measuring the lift and drag coefficient, C_l and C_d at varying angles of attack α.

The drag on an airfoil is strictly defined as the force equal to the rate of momentum loss in the free stream around the airfoil. It is the combined effect of shear stresses [25], called *friction drag* and pressure forces termed *pressure drag* or *form drag*. The lift is found to depend predominantly on pressure such that it can be considered a function of the pressure forces only [31]. In Figure 3.8 the pressure distribution around an airfoil is depicted graphically at two angles of attack together with the corresponding plot of the pressure coefficient C_p. Arrows pointing outward represent a negative pressure (vacuum) while inward pointing arrows represent a positive pressure on the surface.

The pressure difference between the upper and lower surfaces is apparent with pressures on the upper surface lower than the lower surface. The net force on the airfoil perpendicular the flow direction is the lift, and the net force parallel to the flow direction is the pressure drag. The C_p vs. x/c graph shows the values of pressure coefficient C_p over the normalized chord length of the airfoil. The y-axis is generally inverted such that the top side of the curve corresponds to the top side of the airfoil at positive angles of attack.

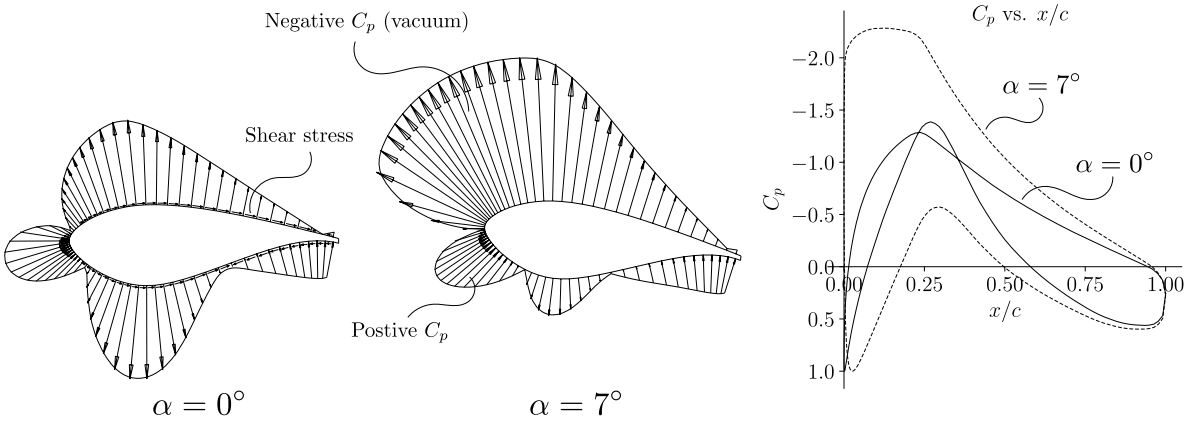

Figure 3.8: Pressure distribution of a DU97-W-300 airfoil at two angles of attack.

lift and drag are the combined effect of the force normal to the chord line N and parallel to the chord line A. Multiplying the normal and axial components with a differential area of the airfoil surface $dA = Sds$, with S the spanwise direction and ds the differential section of the perimeter, yields differential forces in respectively normal and axial direction with respect to the chord line. Integrating the differential forces over the airfoil surfaces yields the normal and axial forces (per unit span, $S = 1$) respectively:

$$N = \int_{\text{top}} (-p\cos\theta - \tau\sin\theta)\, ds + \int_{\text{bot}} (p\cos\theta - \tau\sin\theta)\, ds \tag{3.17}$$

$$A = \int_{\text{top}} (-p\sin\theta + \tau\cos\theta)\, ds + \int_{\text{bot}} (p\sin\theta + \tau\cos\theta)\, ds \tag{3.18}$$

Where θ represents the angle of the airfoil surface with respect to the chord line defined positive in clockwise direction [5]. The s coordinate runs from and to the trailing edge starting over the top side as shown in Figure 3.9(l).

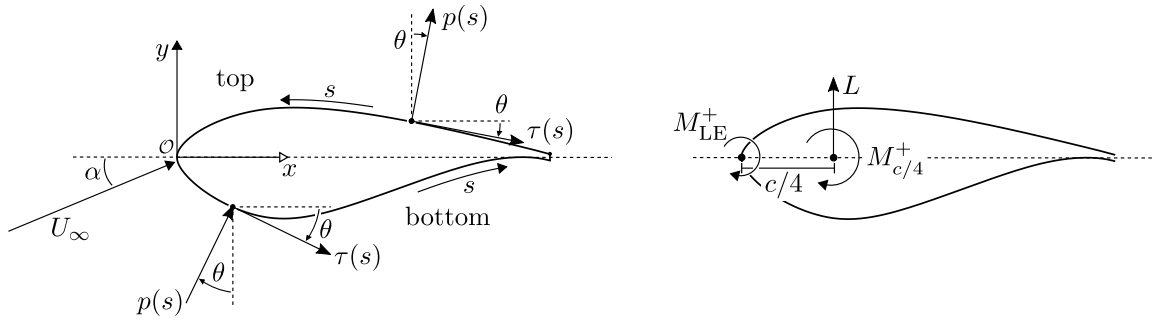

Figure 3.9: (l) Integration of pressure and shear stress distribution over an airfoil surface. (r) Aerodynamic moments around the leading edge and quarter chord point.

In practice the surface shear stress τ is extremely difficult to measure experimentally. Moreover it can be shown that its contribution to the total lift L is much less than that of the pressure p such that it is common practice to neglect it. This yields the following equation for the normal and axial forces based on integration of the pressure alone.

$$N_{(p)} = \int_{\text{top}} (-p\cos\theta)\, ds + \int_{\text{bot}} (p\cos\theta)\, ds \tag{3.19}$$

$$A_{(p)} = \int_{\text{top}} (-p\sin\theta)\, ds + \int_{\text{bot}} (p\sin\theta)\, ds \tag{3.20}$$

In practical experiments the surface of a two-dimensional wing suspended in a free stream (such as a wind tunnel) is equipped with a discrete amount of static pressure tabs distributed around the wing perimeter. Each pressure tap measures the static surface pressure at a discrete location around the perimeter. By numerical integration of the pressures an approximation of equations (3.19) and (3.20) is found after which the lift and drag can be computed from Equations (3.12) and (3.13). The mathematical procedures for numerical integration of the pressure distribution will be discussed in detail in Appendix B.

As shear stress at the surface is proportional to the velocity gradients perpendicular to the surface, $\tau_w = \mu(\partial u/\partial y)_{y=0}$, which at high Reynolds number grow substantially its influence on the total drag force D may not be neglected. Nevertheless the pressure drag D_p and pressure drag coefficient C_{dp} may still be computed from the pressure distribution by considering the streamwise component of the pressure normal to the airfoil surface computed using Equation (3.13). As the forces in axial direction are an order of magnitude lower than those in normal direction the sensitivity to errors in θ is high. Numerical approximation of the integrals defining D_p is therefore prone to large errors as shown in Appendix B.

The aerodynamic moment generated on the airfoil by the pressure and shear stress distributions is generally taken around the *quarter chord point*, denoted by $M_{c/4}$, as shown in Figure 3.9(r). In case of low speed aerodynamics this point coincides with the *aerodynamic center* at which the moment generated is independent of the angle of attack α. To determine the moment around the quarter chord we first compute the moment around the leading edge (based on pressure alone) where moments that increase α are considered positive by convention.

$$M_{\mathrm{LE}(p)} = \int_{\mathrm{top}} [(p\cos\theta)x - (p\sin\theta)y]\,ds + \int_{\mathrm{bot}} [(-p\cos\theta)x + (p\sin\theta)y]\,ds \tag{3.21}$$

The moment around the leading edge is related to the moment around the quarter chord as follows (see Figure 3.9(r)) [5]:

$$M_{\mathrm{LE}} = M_{c/4} - \frac{c}{4}L \tag{3.22}$$

From which $M_{c/4}$ can be computed.

3.2.4 Drag from wake surveys

The inability of measuring the shear stress directly prevents accurate determination of the total drag from static surface pressure measurements alone such that other means of experimental drag determination are used. To determine the total drag D of an airfoil the momentum loss in the free stream is to be determined. Fluid passing over an airfoil suffers a loss in momentum equal to:

$$D = \rho \int_{w_2} u_2\,(U_\infty - u_2)\,dy_2 \quad \text{with} \quad u_2 = \sqrt{\frac{2(H_2 - p_\infty)}{\rho_\infty}} \tag{3.23}$$

Where ρ is the density, U_∞ is the free stream velocity and u_2 the velocity profile in the wake far downstream of the body as shown in Figure 3.10. H_2 is the total pressure that would be measured at this position. Far downstream static pressure recovery has taken place such that $p_2 = p_\infty$.

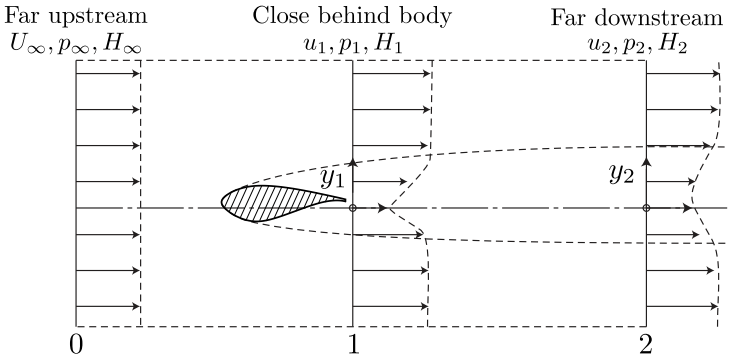

Figure 3.10: Control volume for drag analysis

Close behind the body, the velocity and static pressure vary from those in the free stream ($p_1 \neq p_\infty$ and $u_1 \neq U_\infty$). B.M. Jones [26] allowed for this phenomena by making the assumption that the total pressure between planes 1 and 2 can be considered constant, so $H_1 = H_2$ as referred to by Houghton et al. [25]. Using the Bernoulli equation we then obtain:

$$H_\infty = p_\infty + \frac{1}{2}\rho U_\infty^2 \quad \text{and} \quad H_1 = p_1 + \frac{1}{2}\rho u_1^2 = p_\infty + \frac{1}{2}\rho u_2^2 \tag{3.24}$$

The velocities U_∞, u_1 and u_2 are then given by,

$$U_\infty = \sqrt{\frac{2(H_\infty - p_\infty)}{\rho_\infty}}, \quad u_1 = \sqrt{\frac{2(H_1 - p_1)}{\rho_\infty}} \quad \text{and} \quad u_2 = \sqrt{\frac{2H_1 - p_\infty}{\rho_\infty}} \tag{3.25}$$

Which when substituted in (3.23) yields

$$D = 2\int_{w_2} \sqrt{H_1 - p_\infty}\left(\sqrt{H_\infty - p_\infty} - \sqrt{H_1 - p_\infty}\right) dy_2 \tag{3.26}$$

By considering the conservation of mass between planes 1 and 2 one can show that the drag D can then be computed using the following relation [25].

$$D = 2\int_{w_1} \sqrt{H_1 - p_1}\left(\sqrt{H_\infty - p_\infty} - \sqrt{H_1 - p_\infty}\right) dy_1 \tag{3.27}$$

We express this in dimensionless form as the (total) drag coefficient C_d as:

$$C_d \equiv \frac{D}{q_0 c} = \frac{D}{\frac{1}{2}\rho U_\infty^2 c} = \frac{D}{c\,(H_\infty - p_\infty)} \tag{3.28}$$

such that Equation (3.27) becomes

$$C_d = \frac{2}{c}\int_w \left(\sqrt{\frac{H_1 - p_1}{H_\infty - p_\infty}} - \frac{H_1 - p_1}{H_\infty - p_\infty}\right) dy_1 \tag{3.29}$$

Switching to the derivation by Barlow et al. [7] this can be written more compactly as:

$$C_d = \frac{2}{c}\int_w \left(\sqrt{\frac{q}{q_0}} - \frac{q}{q_0}\right) dy_1 \quad \text{where} \quad \begin{cases} q \equiv \frac{1}{2}\rho u_1^2 = H_1 - p_\infty \\ q_0 \equiv \frac{1}{2}\rho U_\infty^2 = H_\infty - p_\infty \end{cases} \tag{3.30}$$

By using the pressure coefficient of the pressures in the wake C_{pw} (Equation (3.16)) We can write this expression more conveniently:

$$C_d = \frac{2}{c}\int_w \left(\sqrt{C_{pw}} - C_{pw}\right) dy_1 \quad \text{where} \quad C_{pw} \equiv \frac{H_1 - p_\infty}{q_0} \tag{3.31}$$

The total and static pressure H_1 and p_1 are determined experimentally by using a *wake rake* positioned just downstream of the airfoil. A wake rake is a bank of total pressure tubes spaced a certain distance apart and located a short distance downstream the object under test. The total pressure in each tube is individually measured such that its distribution over the wake is obtained (Figure 3.11). By making the measured pressures dimensionless followed by application of Equation (3.31) one obtains the drag coefficient.

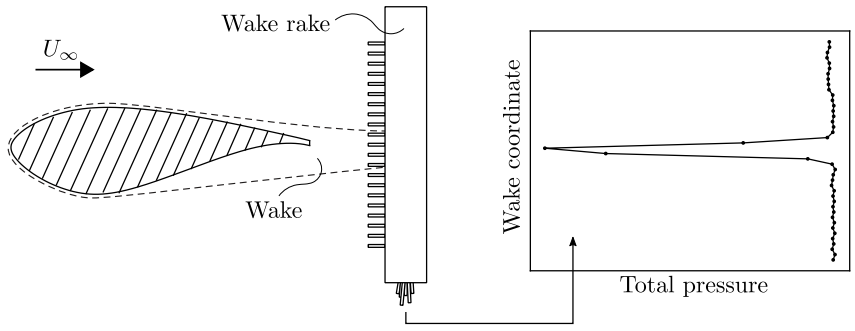

Figure 3.11: Wake survey using a wake rake

The integral of Equation (3.31) is generally solved numerically as the wake rake is composed of a discrete number of total pressure tubes. Let the rake have N tubes such that the integral may be approximated using the trapezoidal rule:

$$C_d \approx \frac{2}{c}\sum_i^N \left(\sqrt{\bar{C}_{pw,i}} - \bar{C}_{pw,i}\right) dy_i \quad \text{where} \quad \begin{cases} \bar{C}_{pw,i} = \frac{1}{2}\left(C_{pw,i} + C_{pw,i-1}\right) \\ dy_i = y_i - y_{i-1} \end{cases} \tag{3.32}$$

3.2.5 C_l and C_d Representation

Aerodynamic characteristics of airfoils are generally expressed as function of lift coefficient C_l in so called *polar plots*. A classical source of airfoil aerodynamic characteristics data is given by Abbot and von Doenhoff [1] who collected data of most standard NACA airfoils. Figure 3.12 shows aerodynamic characteristics of a DU97-W300 airfoil. The left graph shows the lift coefficient C_l plotted versus the drag coefficient C_d, this representation allows one to easily distinguish airfoils with the highest lift-over-drag ratio ($(C_l/C_d)_{\max}$) as it equals the gradient of a line leaving the origin tangent to the curve. The maximum C_l/C_d ratio takes place at approximately $\alpha = 9.3°$ for this airfoil.

The right graph shows C_l versus the angle of attack α. The maximum amount of lift is generated at $\alpha = 12.4°$. At small angles of attack C_l increases approximately linearly with increasing α following thin section theory according to the relation $C_l = 2\pi \sin(\alpha - \alpha_0)$. Due to the level of camber of the DU97-W-300 airfoil zero lift is achieved at a negative angle of attack $\alpha \approx -2.4°$.

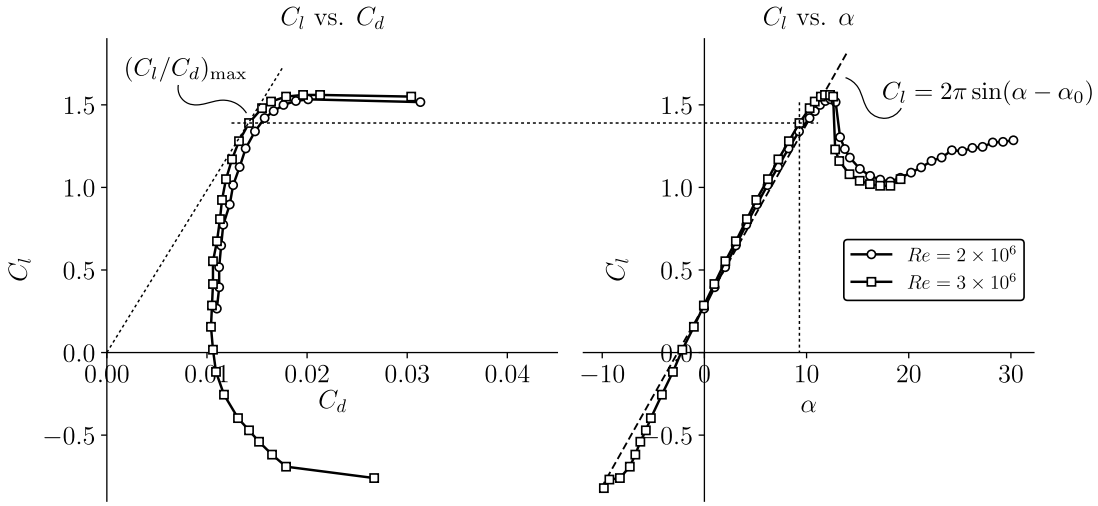

Figure 3.12: Drag an lift polar plots of a DU97-W-300 airfoil. Data from Timmer and van Rooij (2003) [60] and Baldacchino (2018) [6]

The Moment coefficient C_m is generally represented in a similar fashion as function of C_l. In contrast to aerospace applications however C_m is considered less important in wind turbine aerodynamics as it has less influence on wind turbine efficiency compared to the lift and drag coefficients.

3.3 XFOIL

XFOIL is a software program for designing and analysing subsonic isolated airfoils. It is written by Mark Drela in 1986 and the last update XFOIL 6.99 was published in 2013 [16]. The software consists of a collection of menu-driven routines which can perform viscous and inviscid analysis of airfoils and provide options for airfoil (re)design, either via direct method or inverse calculation. XFOIL is freely available making it a primary software tool for two-dimensional airfoil analysis.

The basis of XFOIL makes use of an inviscid linear-vorticity panel code with a Karman-Tsien compressibility correction as described by Drela [15]. Using source distributions superimposed on the airfoil and its wake the code is able to model influence of the viscous layer on the inviscid flow field (potential flow). Laminar and turbulent boundary layers are treated with an e^N-type amplification formulation for determining the transition point. An in to depth treatment of the theoretical background on XFOIL is beyond the scope of this thesis and interested readers are referred to the work of Katz and Plotkin [27].

Inviscid formulation

The inviscid formulation of the panel code uses a linear stream function for describing the two-dimensional flow field. The stream function is constructed by the superposition of the freestream flow, a vortex sheet of strength γ together with a source sheet of strength σ on the surface of the airfoil. The source sheet is applied to the wake as well as shown in Figure 3.13. This yields the following expression for the stream function:

$$\Psi(x,y) = \underbrace{u_\infty y - v_\infty x}_{\text{free stream flow}} + \underbrace{\frac{1}{2\pi}\int \gamma(s)\ln r(s;x,y)ds}_{\text{vortex sheet}} + \underbrace{\frac{1}{2\pi}\int \sigma(s)\theta(s;x,y)ds}_{\text{source sheet}} \tag{3.33}$$

Where s is the arc length coordinate along the vortex and source sheets and r is the magnitude of the vector between the point at s and the field point (x, y). θ is the angle of vector r with the y-axis.

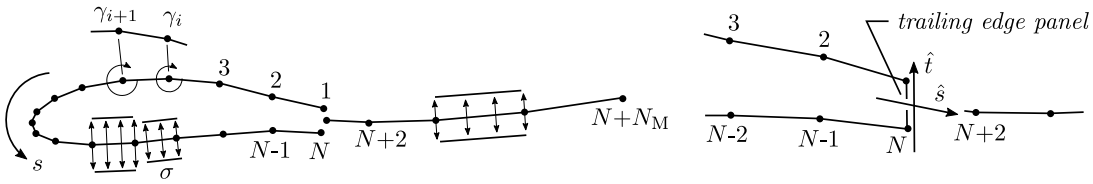

Figure 3.13: Airfoil and wake panelling showing vorticity and source distributions (left) and trailing edge detail (right). Figure courtesy of [15]

Viscous formulation

The boundary layer and the wake are modelled with the following two-equation integral boundary layer formulation:

$$\frac{d\theta}{d\xi} + (2 + H - M_e^2)\frac{\theta}{U_e}\frac{dU_e}{d\xi} = \frac{C_f}{2} \tag{3.34}$$

$$\theta\frac{dH^*}{d\xi} + (2H^{**} + H^*(1-H))\frac{\theta}{U_e}\frac{dU_e}{d\xi} = 2C_D - H^*\frac{C_f}{2} \tag{3.35}$$

Where ξ is the streamwise coordinate and the *density thickness shape parameter* H^{**} is defined as:

$$H^{**} = \left(\frac{0.064}{H_k - 0.8} + 0.251\right)M_e^2 \quad \text{with} \quad H_k = \frac{H - 0.290M_e^2}{1 + 0.113M_e^2} \tag{3.36}$$

For a more detailed description on the mathematical formulations in XFOIL the reader is referred to Drela [15].

4 Model fabrication

In this chapter the design and fabrication of a wind tunnel model for aerodynamic experiments is discussed. First an introduction is given to the type of airfoil considered and the motivation for its choice. The aerodynamic properties are presented forming a reference for the experimental and numerical work. Next the design and fabrication of the wind tunnel model for use in the wind tunnel facilities of the Engineering Fluid Dynamics group is discussed.

4.1 DU97-W-300 wind turbine airfoil

The wind turbine airfoils designed by the Delft University of Technology (TU Delft) are at present used by various wind turbine manufacturers for blade lengths between 14.5 m and 50 m for turbines in the range of 350 kW to 3.5 MW [60]. The range of TU Delft wind turbine airfoils stretches between airfoils of $0.15t/c$ to $0.40t/c$ and are designated using a common notation $DUyy\text{-}W\text{-}xx$. Where DU indicates Delft University, yy indicates the year in which the airfoil was designed, W denotes that the airfoil is designed for Wind energy applications and lastly xxx represent 10 times the airfoil relative thickness followed by a design iteration number (e.g. 350 denotes an airfoil of $0.35t/c$ of the first design iteration).

The DU97-W-300 airfoil type is specifically developed for wind turbine applications in 1997 and forms a base for thick airfoil designs. Figure 4.1 shows the geometry of the DU97-W-300 airfoil. Timmer and van Rooij [60] give a thorough background on the design of the airfoil which is intended for span wise locations up to 40% of the blade length, a so called *inboard* airfoil. To ensure structural integrity of long blades, inboard sections are required to be relative thick, typically between 30% and 40% of the chord length. A high lift coefficient is required for segments of the blade close to the hub to deliver sufficient torque at relative lower wind speeds.

Next to this a low sensitivity to contaminations and contour imperfections at the leading edge was required. This is accomplished by limiting the upper surface thickness, assuring low velocities on the suction side. A lower adverse pressure gradient is hereby achieved allowing the flow to better resist disturbances as a result of leading edge roughness. In case of the DU97-W-300 airfoil a maximum of 25% performance penalty due to the effects of surface roughness was allowed. To still achieve the desired thickness the bottom side of the airfoil is thickened. Sufficient lift is accomplished by applying an *under camber* (or *S-shaped*, tail which produces more aft loading (a larger portion of the lift force acting on the rear of the airfoil) [65]. The location of the maximum thickness of $t/c = 0.3$ is located at $x/c = 0.3$ preventing early transition and turbulent separation on the lower surface while simplifying the structural design [65].To assure further increases in bending stiffness a thick trailing edge of $1.5\%c$ is maintained. The section is designed to be smoothly transferable to the DU91-W2-250 airfoil.

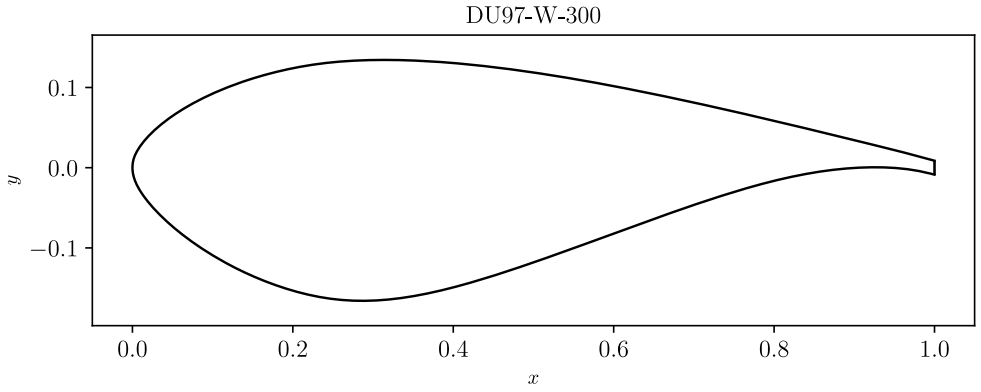

Figure 4.1: Geometry of the DU97-W-300 airfoil. The maximum thickness is $30\%c$ *which is located at* $0.3c$*. Low roughness sensitivity is achieved by keeping the upper side thin. Early flow separation at lower and negative angles of attack is achieved by thickening the bottom side.*

4.1.1 Reference aerodynamic data

Reference data of the DU97-W-300 airfoil is obtained from Timmer and van Rooij and Baldacchino et al. [60, 6] at $\mathrm{Re}_c = 3{\times}10^6$ and $\mathrm{Re}_c = 2{\times}10^6$ respectively. Both datasets have been measured in the closed-loop, low turbulence wind tunnel at the TU Delft having a test section with width$\times$height of 1250×1800 mm in which the airfoil is positioned vertically. The free stream turbulence in the test section ranges between 0.02% to 0.07% at 25 m/s to 75 m/s respectively. The model chord length in the experiments by Timmer and van Rooij was 600 mm and is constructed using a polyester gel-coat. Surface pressures where measured using 100 pressure taps of diameter 0.4 mm around the airfoil perimeter. The dimensional accuracy of the contour is expected to be below 0.1mm [60]. In the measurements by Baldacchino et al. the model chord length was 650 mm and includes 102 pressure taps. Drag was measured in both experiments using a 540 mm wide traversing wake rake comprising of 67 total pressure tubes and 16 static tubes.

Free transition conditions

Figure 4.2 shows the lift and drag polar plots at free boundary layer transition (or "clean" conditions). The maximum lift coefficient $C_{l,\max}$ is 1.56 and 1.53 for Reynolds numbers of 3 and 2 million respectively. These values are reached around an angle of attack $\alpha = 12.3°$. The maximum lift-over-drag ratio $(C_l/C_d)_{\max}$ is reached at $\alpha = 9.3°$ and reads 97.9 for Reynolds equals 3 million and 90.5 for a Reynolds number of 2 million. The increase in drag coefficient with reduction in Reynolds number (due to the increase in boundary layer momentum thickness) is visible in the drag polar causing the reduction of the lift-over-drag ratio. The angle of attack for which the lift coefficient is zero lies around $\alpha_0 = -2.3°$ for both $\mathrm{Re}_c = 3{\times}10^6$ and $2{\times}10^6$.

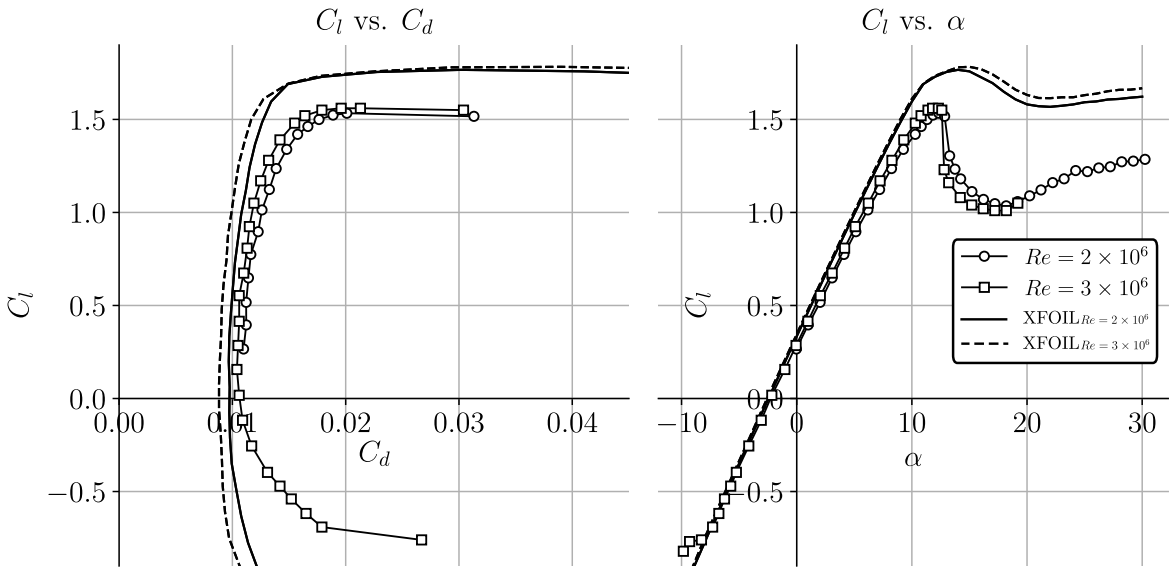

Figure 4.2: Lift and drag characteristics of the DU97-W-300 airfoil with free transition from laminar to turbulent flow at varying Reynolds numbers.

Comparison with XFOIL

XFOIL predictions are cross plotted on the polars revealing that lift and drag are over- and under-predicted respectively. These discrepancies in lift and drag prediction by XFOIL have been found by other researchers as well. Ramanujam and Özdemir [45] found that these effects can be contributed to *i*) the trailing edge panel formulation used by XFOIL combined with *ii*) the wake trajectory prediction and *iii*) the free stream turbulence conditions which are not accounted for by XFOIL.

The trailing edge panel formulation in XFOIL comprises of a source strength associated to the trailing edge panel forming a streamline downstream from the trailing edge. This results in a jet-like behaviour where mass is constantly ejected from the trailing edge to assure the Kutta condition is met (see Section 3.2.2). The consequence of this method is a reduction in pressure at the trailing edge affecting the pressure distribution all together with the net effect of increased lift prediction [45].

Besides over-prediction of the lift, the gradient of the lift with respect to the angle of attack is too steep. In XFOIL the wake trajectory is taken from an inviscid solution at a given angle of attack which is not deemed correct as viscous effects tend to decrease lift and change the wake trajectory. At higher angles of attack this effect could become more pronounced as explained by Ramanujam and Özdemir [45] such that at high angles of attack the discrepancies increase yielding a steeper gradient.

The under-prediction of drag by XFOIL is attributed to the difference in definition of the momentum thickness θ used in XFOIL as explained by Ramanujam, Özdemir and Hoeijmakers [46]. Instead of the free stream velocity U_∞ (see Equation (3.9)) the velocity at the edge of the boundary layer U_e is used. As $U_e > U_\infty$ the momentum thickness based on the assumption that $U_\infty = U_e$ is smaller. Since the drag coefficient equals the momentum loss in the wake ($C_d = 2[\theta]_{x\infty}/c$) A lower momentum thickness yields an under-prediction in drag coefficient.

The steep drop in lift coefficient post stall observed in experiments is not captured very well by XFOIL. The viscous-inviscid interaction method is not designed to treat the heavily separated flows. When the boundary layer becomes too thick (as in the onset of flow separation) to computational method fails such that predictions in the post-stall regime are deemed inaccurate[1]. [46]

Measured surface pressure distributions at $\mathrm{Re}_c = 3{\times}10^6$ and $\mathrm{Re}_c = 2{\times}10^6$ for three angles of attack are shown in Figure 4.3 together with XFOIL predictions. A total of 102 static pressure taps were used including one in the centre of the thick trailing edge of the airfoil. XFOIL predicts the C_p rather well apart besides the predictions being slightly lower on the suction side and higher on the pressure side. The mentioned trailing edge formulation in XFOIL affects this behaviour resulting in higher calculated lift coefficients. Reducing the trailing edge thickness artificially[2] yields better agreement with experimental results [60].

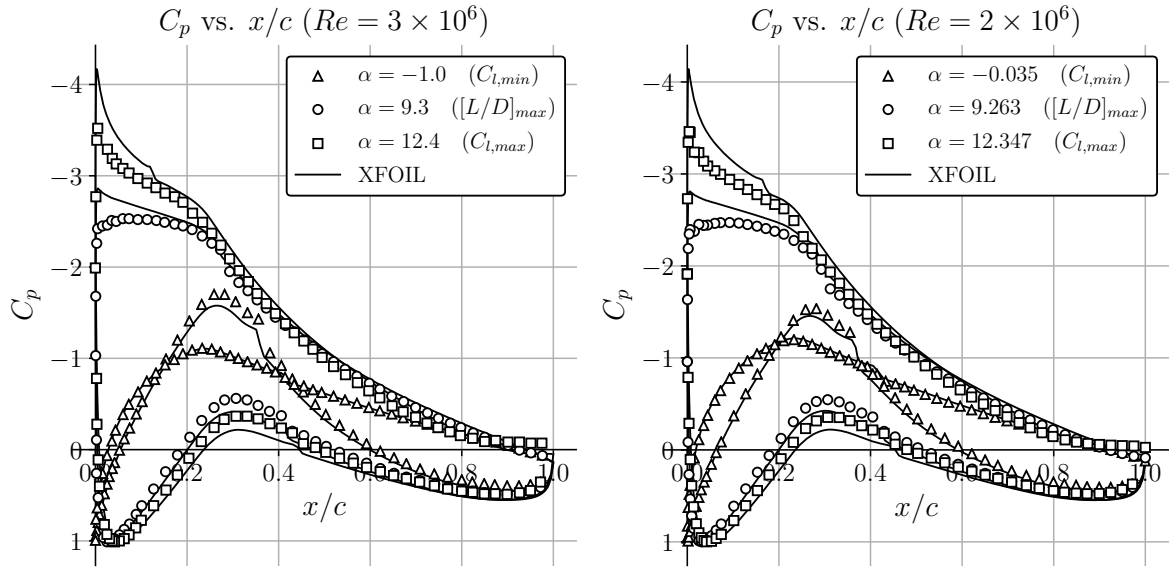

Figure 4.3: Measured and predicted pressure distributions at three angles of attack for $Re = 3{\times}10^6$ (l) and $Re = 2{\times}10^6$ (r).

Rough conditions

More so than in aerospace applications rotor blades of wind turbines are subject to constant contamination as insects and other foreign matter collides and adheres to the blades. Leading edge contamination causes premature boundary layer transition, eventually causing early turbulent separation, resulting in a significant decay in aerodynamic performance. To account for fouling over lifetime aerodynamic performance of airfoils is typically measured and predicted both in a "clean" and a "fouled" state.

To simulate this effect of leading edge fouling the boundary layer is "tripped" by applying an artificial roughness patch at a distinct location on the airfoil nose. Due to the roughness patch the laminar

[1] Care should therefore be taken when designing airfoils for stall characteristics as one can't rely on XFOIL predictions in the regime under consideration.

[2] By using XFOIL's `GDES/TGAP` routine

boundary layer is disturbed ensuring direct transition to turbulent flow at the tape's location. Tripping is generally realized by application of *zigzag-* or *tubulator tape* at the surface of the model. An example of the zigzag tape used is given in Figure 4.4 and is applied at $0.05x/c$ from the leading edge at the upper side. Experiments from Timmer and van Rooij ((a) in Figure 4.4) were measured using 0.35 mm thickness [65] while data from Baldacchino (b) was obtained using only 0.17 mm thick tape [6].

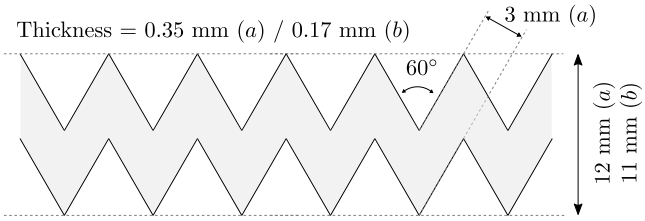

Figure 4.4: Zigzag tape to simulate the performance under forced transition of the boundary layer due to leading edge roughness applied at $0.05x/c$ *on the airfoil suction side.*

Polar plots showing the lift and drag coefficients under conditions of early, or *forced*, turbulent transition are shown in Figure 4.5. The maximum lift coefficient $C_{l,\max}$ at a Reynolds number of 3 million reduces to 1.16 (-25% with respect to clean conditions) at an angle of attack of $\alpha = 9.0°$ ($-3°$). The maximum C_l/C_d drops considerably to 52.6 (-46%) occurring at $\alpha = 6.2°$ ($-3°$). At a Reynolds number of 2 million the effects are very similar. $C_{l,\max}$ drops to 1.11 (-27%) taking place at $\alpha = 9.2°$ ($-3°$). $(C_l/C_d)_{\max}$ in forced transition conditions shows a decay of 45% down to 50.0 occurring at $\alpha = 6.2°$ ($-3°$).

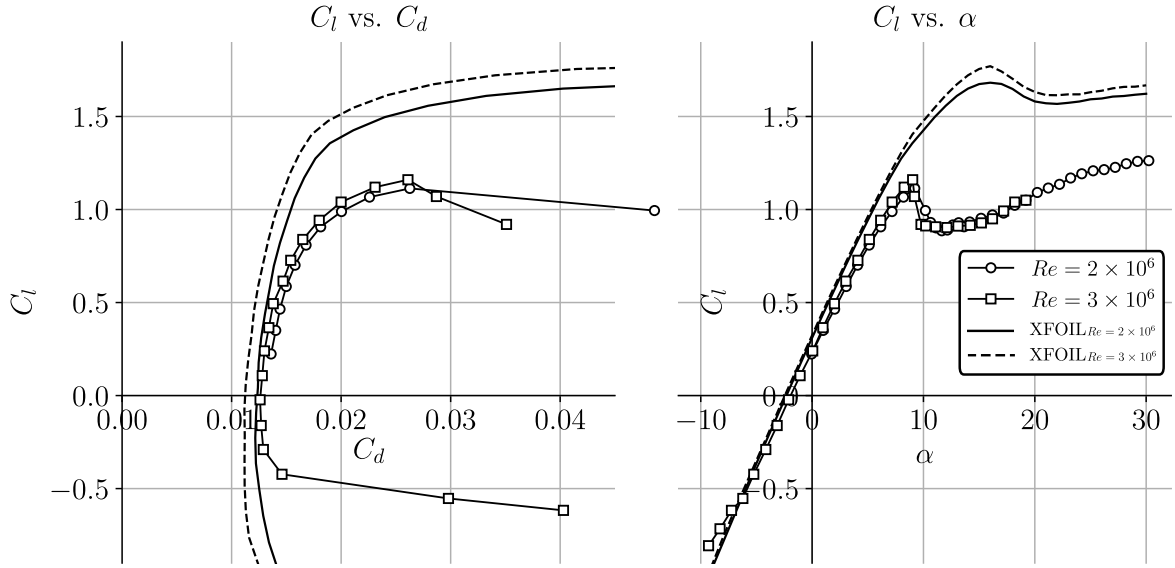

Figure 4.5: Aerodynamic performance of the DU97-W-300 airfoil under "rough" conditions as measured by Timmer and van Rooij [60] and Baldacchino et al. [6].

Comparison with XFOIL

Even more so than under free transition conditions XFOIL over-predicts lift and under-predicts drag. A combination of i) the difference in definition of the momentum thickness by XFOIL yielding smaller θ, as discussed above, and ii) The excessive thickness of the zigzag tape for the purpose of forcing transition.

Transition due to a given type of surface roughness is found to occur at a given *critical roughness Reynolds number*[1] $\mathrm{Re}_{kc} = u_k k_c/\nu$. For zigzag tape Re_{kc} is estimated to lie around 50 [23]. Roughness Reynolds numbers of 0.35/0.17 mm zigzag tape, applied at $0.05x/c$ on a 600/650 mm chord model can be computed described in Section 5.3.5 resulting in $\mathrm{Re}_k \approx 1900$ for data at $\mathrm{Re}_c = 3{\times}10^6$ and $\mathrm{Re}_k \approx 330$ when $\mathrm{Re}_c = 2{\times}10^6$. These values are higher than $\mathrm{Re}_{kc} \approx 50$ resulting in excessive thickening of the momentum thickness causing both an increase in drag and earlier separation yielding a low $C_{l,\max}$. Applying thinner zigzag tape should probably have the effect of increasing the maximum lift coefficient and reducing the drag, meeting the predictions of XFOIL better.

[1] More details in Section 5.3.5

4.2 Airfoil model

For experimental research in the University of Twente wind tunnel a physical model of the DU97-W-300 airfoil is designed and manufactured. This section discusses the main features of the airfoil model, lays out its specifications and describes the building process.

4.2.1 Model design

Sizing

As operating conditions in a wind tunnel differ considerably from those experienced in unbounded flows certain design aspects must be considered to mimic open air conditions as close as possible. Contrary to open air conditions, wind tunnel flows are confined causing the free stream to behave differently compared to real life conditions. Measured performance in a wind tunnel is therefore subject to corrections as discussed in Section 5.4.6.

For airfoil experiments in wind tunnels it is customary to use models that completely span the tunnel. The walls eliminate any trailing vortices coming from the wing tips yielding a closer representation of two-dimensional flow over the section. These wall effects however impose restrictions to the maximum model size. As the through flow area is reduced the velocity around objects spanning the tunnel increases according to the Bernoulli principle.

The *blockage ratio*, defined as the ratio of model projected area over the wind tunnel cross sectional area ($A_{\text{model}}/A_{\text{tunnel}}$) is a measure of the velocity increase in the tunnel due to objects spanning the tunnel. The maximum blockage ratio is usually chosen to be 10% (Barlow et al. [7]) as to minimize the effect of increasing velocity. For airfoil experiments maximum obtainable chord length is desired to allow the highest possible Reynolds numbers to be tested such that the maximum blockage ratio is always preferred. The blockage ratio of the experimental set-up used for measuring the reference data (Section 4.1.1) was 10.8% and this value was taken as benchmark for sizing the model.

The channel dimensions of the wind tunnel at the University of Twente are 900 mm width and 700 mm height. The chord length of an airfoil of 30% thickness ($t/c = 0.3$) when mounted either horizontally or vertically in the wind tunnel can then be determined according to:

$$c = \frac{0.108 A_{\text{tunnel}}}{S(t/x)} \quad \rightarrow \quad \begin{cases} \text{Horizontal} & c = \dfrac{0.108(900 \times 700)}{900(0.3)} = 252\,\text{mm} \\ \text{Vertical} & c = \dfrac{0.108(900 \times 700)}{700(0.3)} = 324\,\text{mm} \end{cases}$$

A chord length of 250 mm was chosen as it allows the model to be placed both horizontally and vertically in the tunnel[3] resulting in overall dimensions of $900 \times 250 \times 75$ mm (span×chord×thickness). The highest obtainable free stream velocity of the wind tunnel lies between $55 - 60$ m/s yielding a maximum chord Reynolds number between $\text{Re}_c \approx 0.9{\times}10^6 - 1.0{\times}10^6$ at a temperature of 20°C. Characteristic Reynolds numbers for wind turbine applications lie between $0.5{\times}10^6$ and $10.0{\times}10^6$ according to Manwell et al. [36] making a model of this size representative for real life conditions in the lower Reynolds number range.

Overall design

To ease installation of static pressure taps and to simplify the manufacturing process the choice was made to compose the full model from multiple sections shown in Figure 4.6. Three different section types are used in the model: Fourteen standard sections of 50 mm wide containing two 6.1 mm through holes and four 5 mm dowel pin holes (two on each side) (b). Two end-sections of 43 mm wide closing off the wing and providing support for the suspending rods (c) and a 100 mm wide measurement section composed of 3 subsections housing the static pressure taps (a). All sections are aligned using a total of thirty-five 5×24 mm dowel pins (f) for accurate orientation and two 900 mm M6 threaded rods (e) for securing the whole model.

[3] A horizontal mounting position was intended at the time of designing the model. Later a vertically mounted setup was adopted which would have allowed an increase in chord length to 324 mm, enabling Reynolds numbers between $\text{Re}_c \approx 1.18{\times}10^6 - 1.29{\times}10^6$ to be reached considering maximum wind speeds between $55 - 60$ m/s.

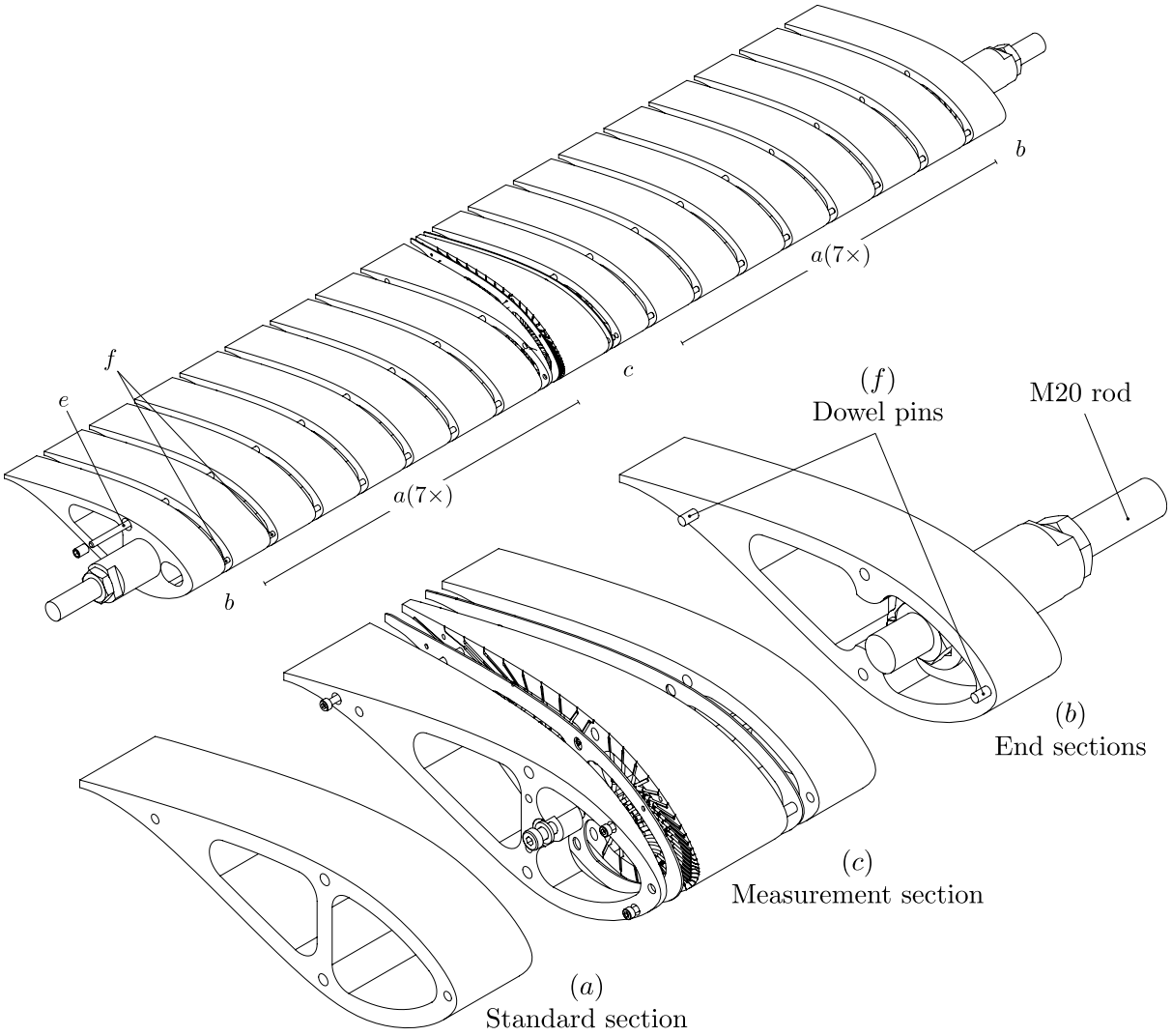

Figure 4.6: Overview of the wing model and its sections from which it is composed.

Figure 4.7 shows a detailed view of the left end-section. Two M20 rods (a) suspend the model in the wind tunnel. The model is fixed to the tunnel on the ¼-chord point. To ensure the ¼-chord point is concentric with the tunnel mounting points a 40×63 mm bushing (b) is fitted over the M20 rod. The bushing is tightly concentric with the 40 mm pocket (c) in the end sections. Two M20 lock nuts (d) secure the rods in the end sections. The inner lock nut is secured by a locking plate (e) fastened by an M5 bolt (f).

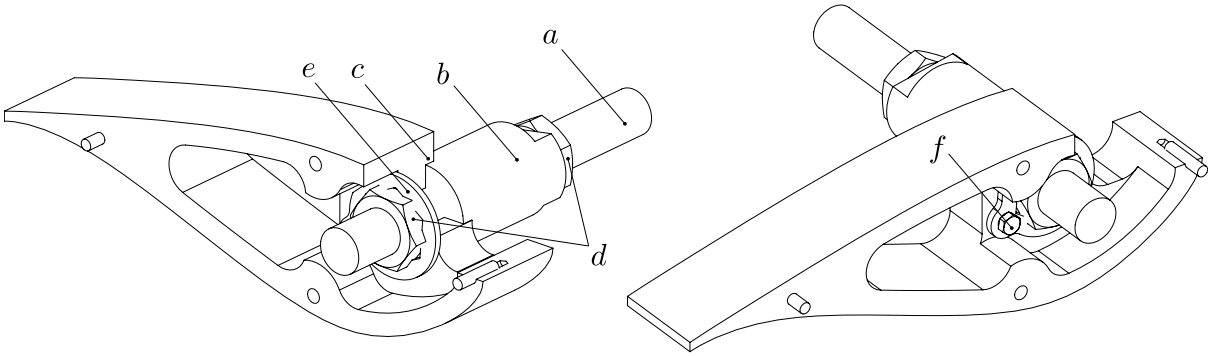

Figure 4.7: Left end-section showing the M20 rod (a), the 40 mm bushing (b), lock nuts (c), locking plate (d) and plate fastening bolt (e).

Pressure taps

To determine the section lift the surface pressure distribution is measured using an array of 47 static pressure taps located around the full perimeter of the wing section[1]. Static pressures at boundaries are measured by connecting pressure sensing elements to small holes in the surface. Considerations must be made on the orientation and dimensions of these holes as they influence the measured pressures as shown by Shaw [54], Rayle [47]. Kuester et al. [30] found that 0.5 mm diameter pressure taps in an DU96-W-180 airfoil of 0.8 m chord allowed better deduction of the lift compared to 1.0 mm holes.

Furthermore the holes should be sharp edged, normal to the surface and free of burs to obtain the most accurate measurements [54]. Diameters of the holes should ideally by infinitely small as not to disrupt the flow. As this is physically impossible the smallest possible hole size is preferred considering it is sharp edged and free of burs. A hole size of 0.3 mm is chosen for the model based on the above mentioned considerations and personal conversations with dr. L.D. de Santana of the Engineering Fluid Dynamic department. Timmer and van Rooij [60] used pressure taps of 0.4 mm diameter in their models of 600 mm chord length at the Delft University wind tunnel.

A two-dimensional flow approximation is best obtained by placing the pressure taps in a single plane parallel to the direction of flow. In case the flow is disrupted by the presence of a pressure tap though, subsequent measurements downstream should not be influenced. The relative position of a pair of pressure taps should be such to prevent disruptions by the upstream tap influencing the downstream tap. For this reason the taps are arranged in a slightly staggered pattern. The stagger angle is chosen larger than the angle generated by a turbulent spot , $\alpha \approx 9.3^\circ - 11.3^\circ$, as discussed by White [67] referring to Emmons [18]. For the airfoil model a stagger angle of $\alpha_{\text{stg}} = 12^\circ$ is chosen.

Manufacturing limitations inhibited the possibility of drilling the pressure taps from the airfoil surface inward. A novel approach is used to circumvent the problem by milling the holes from interfaces of the measurement subsection (a) as shown in Figure 4.8.

The primary interface ($a-b$), housing pressures taps No. 4 till 45 and 47, is placed at an angle α_{stg} with respect to the flow direction such to prevent interference between the taps as discussed. A secondary interface ($a-c$) is needed to accommodate the remaining pressure taps near the trailing edge, No. 1 till 3 and 46.

The milling process results in square shaped taps of width$\times$height of 0.3$\times$0.3 mm (f) as shown in the detail view A. The channels are sealed by a rubber gasket (d) between the opposing sections (b, c). Further inwards the channels widen (g) to accommodate 0.063 inch (1.6 mm) Scanivalve tubulations (h). PVC tubing (j) is subsequently connected, secured with tubing clamps (i), and routed to the data acquisition system. The subsections are secured using bolts (e) assuring a homogeneous clamping force over the interfaces.

The distribution of points is such that 28 taps are placed on the top side and 20 are placed on the bottom side of the airfoil. The arguments for this ratio are twofold: *i)* The used distribution must results in an accurate approximation of the section lift when numerically integrating the measured pressures. And *ii*), a denser distribution on the top side increases the measurement resolution and hence provides a "better view" on the flow phenomena.

The distributions of the top and bottom side respectively are derived from XFOIL. Appendix A describes the background of the procedure used followed by the physical spatial coordinates of the pressure taps. Figure 4.9 presents the result of numerically integrating a given pressure distribution (300 panels with XFOIL) with the chosen distribution (28 top / 20 bottom). The result shows that the chosen distribution provides an adequate resolution considering the errors due to measurement uncertainties, geometrical inaccuracy and experimental randomness are significantly larger as discussed in Section 5.6.3.

[1] Only three 16-channel pressure scanners where available in the EFD group when designing the model. Currently the group has access to six 16-channel pressure scanners, four with a range of ± 1.0 psi and two of ± 2.5 psi. This would have allowed more surface pressure taps to be installed in the model.

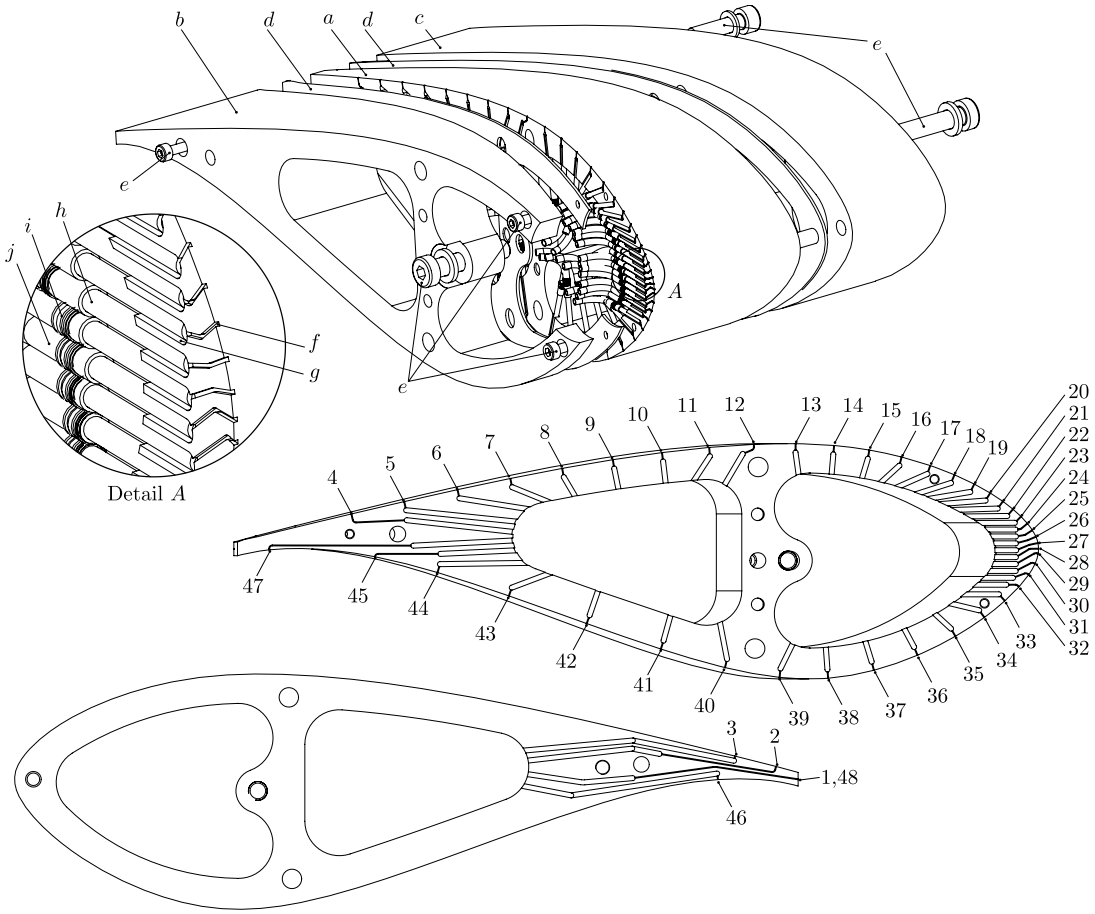

Figure 4.8: Surface pressure measurement block containing the static pressure taps. The cut-out reveals the channels forming the square shaped pressure taps.

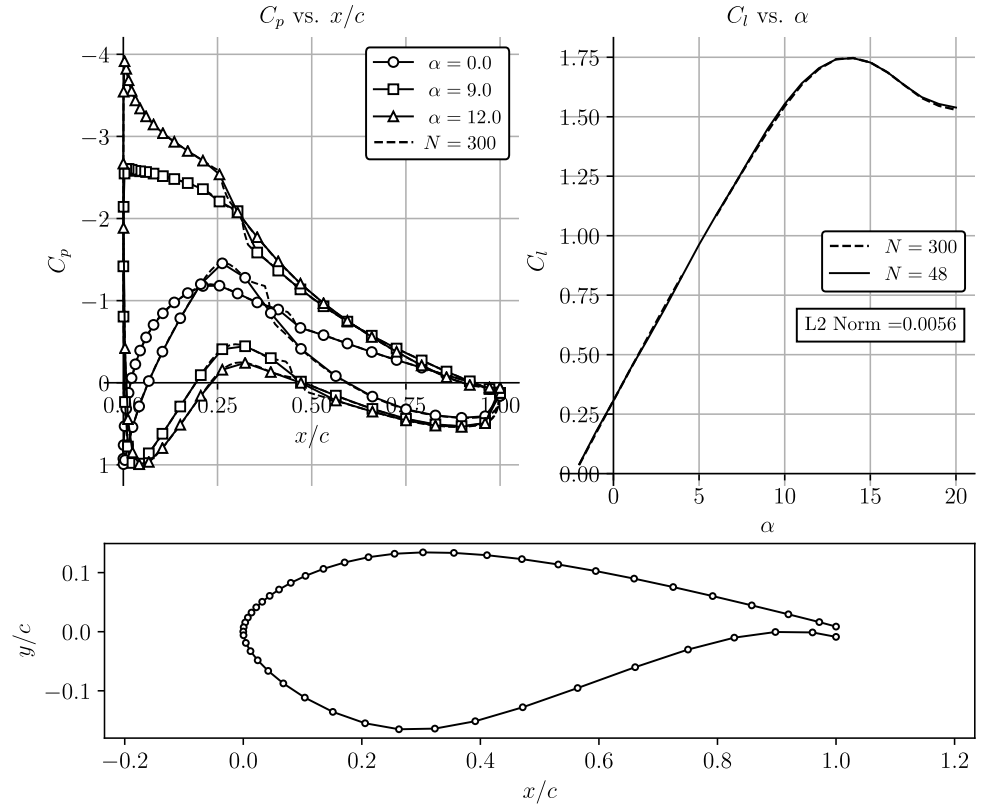

Figure 4.9: Results of numerically integrating the pressure using a distribution of 28 panels on top and 20 panels on the bottom side of the airfoil.

4.2.2 Fabrication and assembly

Measurement section manufacturing and assembly

Al model sections are manufactured from 6082 (51ST) aluminium alloy using CNC milling (Figure 4.10). Machining from aluminium allows the Ra surface roughness of the airfoil to be low without sanding and polishing thereby improving geometric accuracy of the wing sections. The surface roughness of machined parts (Sa according to ISO 25178) is measured to be around 0.3 µm using a Sensofar® S Neox confocal optical profiler at the University of Twente Tribology group.

Figure 4.10: CNC milling of the parts at the University of Twente's "Techno Centrum voor Onderwijs en Onderzoek" (TCO).

The assembly of the measurement section is done prior assemblage of the complete wing. First the dowel pins are fitted to assure correct alignment of the parts. Then all the Scanivalve tubulations are pre-bend, to allow all tubes to fit in the available space. The tubulations are then fitted with PVC tubes and tubing clamps prior installation in the model (Figure 4.11).

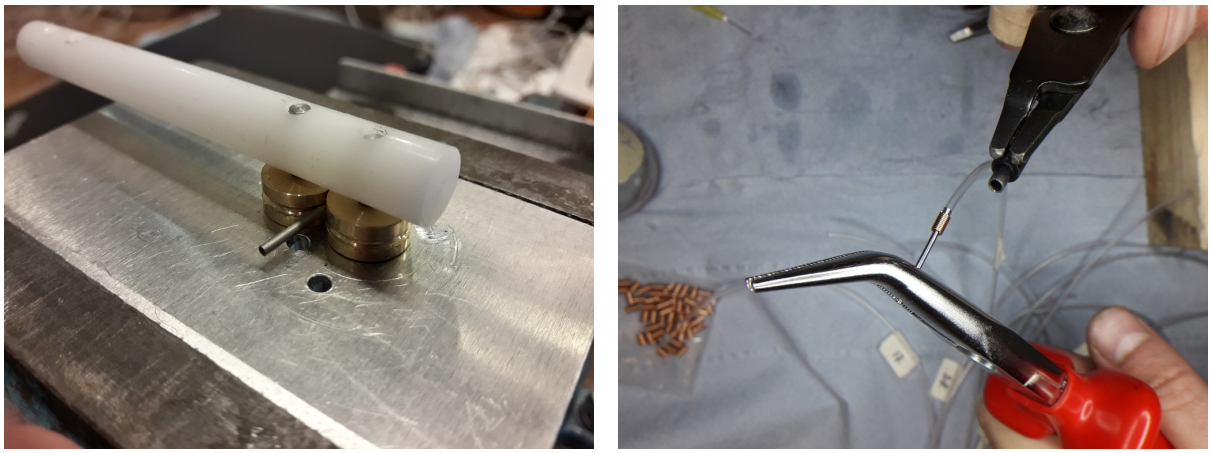

Figure 4.11: Preparing Scanivalve tubulations for fitting: (l) Bending of tubulations using a custom tube bender. (r) Fitting the tubes and tubing clamps using dedicated pliers.

Installation of the tubulations is done using a cyanoacrylate adhesive (Loctide® 401) where care is taken not to spoil the sealing surfaces. As the tubulations (diameter 1.59 mm) fit tightly in the rounded pockets with radius 0.8 mm (Figure 4.12(l)), no further sealant is required on the this side, referred to as the 'bottom' side. To assure the tubulations are flush with (or are slightly below) the sealing surface some material is occasionally removed from the tubulations by filing (Figure 4.12(r))

As the geometry of the 'top' side, mating with the opposing section, is square shaped some form of sealing is required to seal the gap between the circular tubulation and the square edges of the containing pocket (Figure 4.12(l)). Natural bees wax (Dutch: *bijenwas*) is used to seal these gaps by heating the whole section on a laboratory heating plate to approximately 60°C and scrubbing a bees wax candle over the surface (Figure 4.13). This fills the gaps with wax assuring a proper seal when cooled down. Excess wax is removed carefully prior cooling down the parts.

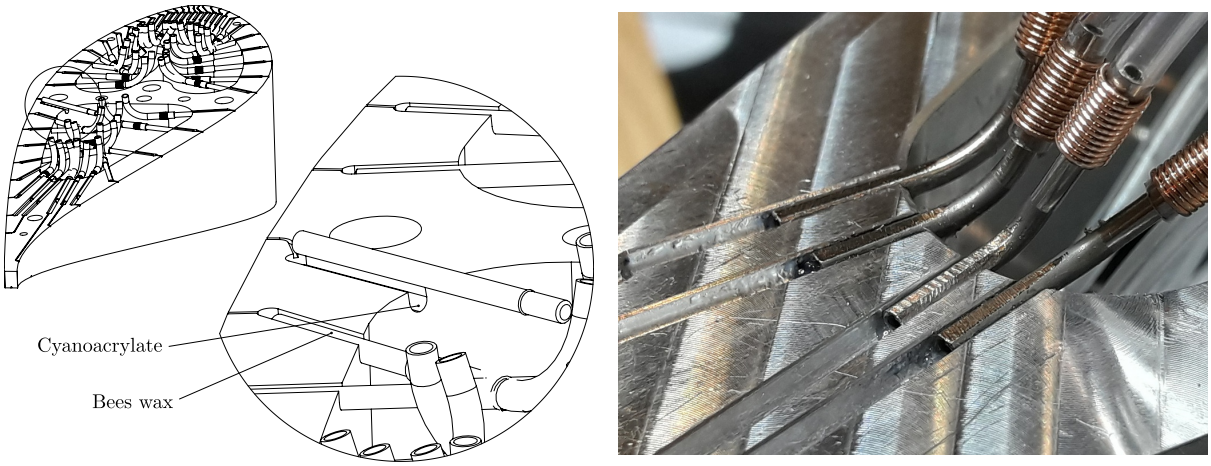

Figure 4.12: Fitting tubulations: (l) Tubulations fit tightly in rounded pockets and are secured with cyanoacrylate adhesive. (r) Fitted tubulations flush with sealing surface by filing off some material

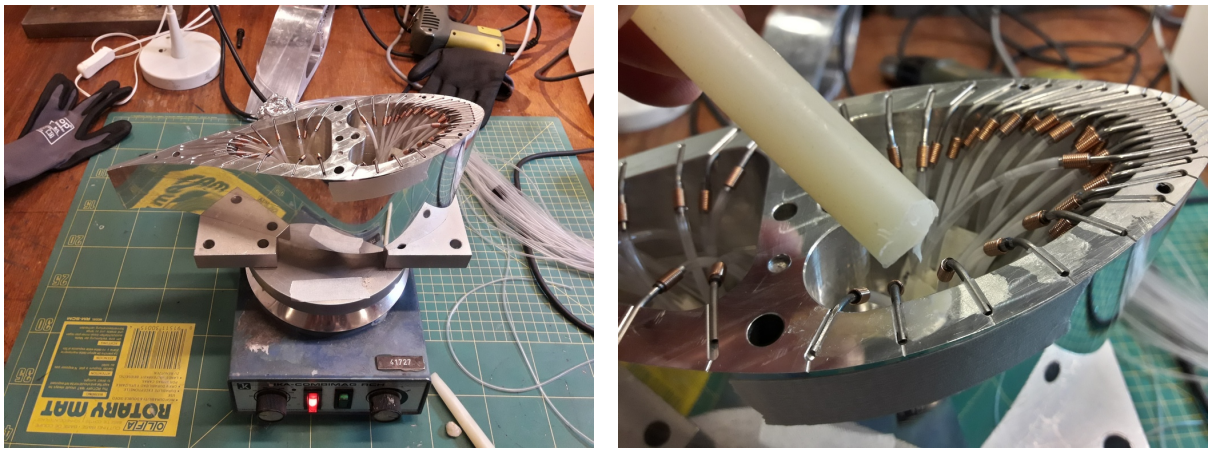

Figure 4.13: Sealing top side of tubulations: (l) Heating measurement section using heating plate. (r) Scrubbing bees wax candle over the surface to fill gaps between tubulations and square edged pockets.

Gaskets are cut from 1.0 mm thick rubber to compensate for unevenness between the sealing surfaces (Figure 4.14(l)). Before installing the rubber gaskets Dow Corning® high vacuum grease is applied to both sides of the gasket to improve airtightness (Figure 4.14(r)). The gasket is then installed in between the two sections of the primary interface. Excess rubber, squeezed out by tightening the two sections, is carefully removed with a sharp blade assuring a flush transition between the sections (Figure 4.16(l)).

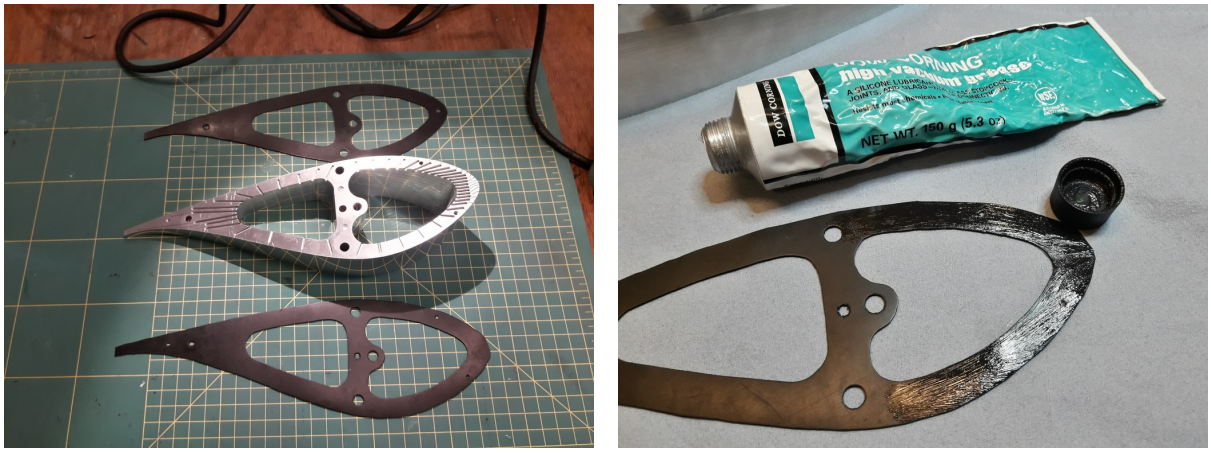

Figure 4.14: Assembly sealing surfaces: (l) Rubber gaskets cut to compensate unevenness. (r) Application of vacuum grease to fully seal the pressure circuits.

The pressure taps, connected tubulations and tubes are checked for airtightness by submerging the measurement section in water and pressuring each pressure tap with compressed air of maximum 2 bar (Figure 4.15(l)). airtightness of the circuits to the outside is checked by looking for bubbles to appear in the water (Figure 4.15(r)). Internally (in between adjacent taps) airtightness is checked by keeping adjacent tubes in the mouth and sensing any air escaping with the tongue.

Figure 4.15: Checking airtightness of circuits: (l) Submerging measurement section in water. (r) Looking for bubbles appearing in water.

Grease, dirt and minor scratches that spoiled the surface during assembly are removed by carefully wet sanding the measurement section with grid 2000 sandpaper and polishing with soft car polish (Innotec® Easy Polish, Figure 4.16(r)). The resulting surface roughness Sa was again measured using the confocal optical profiler and proved to be around 0.25 µm.

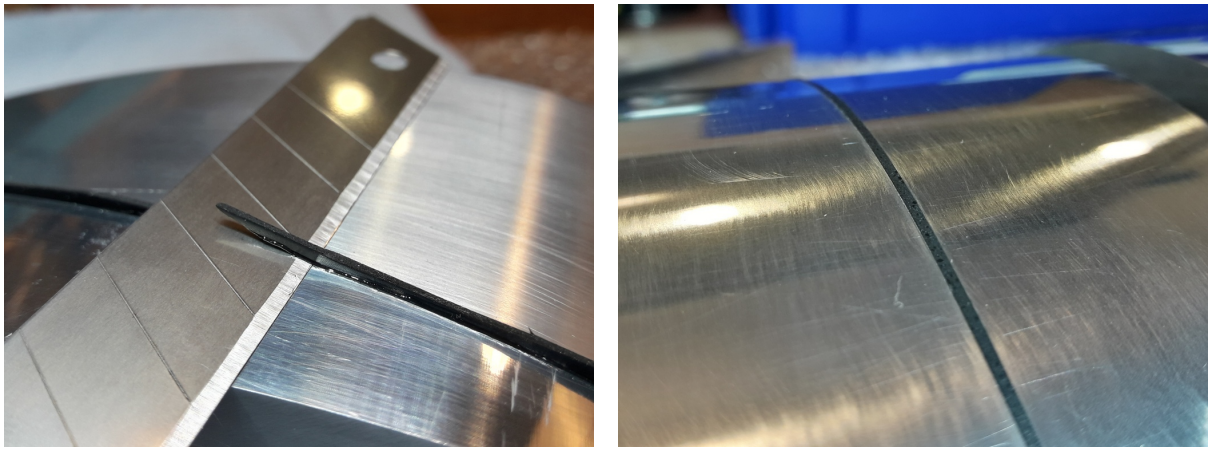

Figure 4.16: Removing excess rubber and finishing: (l) Rubber is removed by scraping a sharp blade carefully over the surface. (r) Finishing is done with grid 2000 sandpaper and polishing using car polish.

Wing assembly

Following assembly of the measurement section both end sides are assembled. The complete wing is then built were grease is applied on all dowel pins to allow for easy disassembly of the parts. The assembled measurement section is placed in the middle of the wing as the tubes are routed through the standard sections enclosing it (Figure 4.17). The rest of the wing is further assembled after which the wing is cleaned to remove grease and dirt from the assembly process.

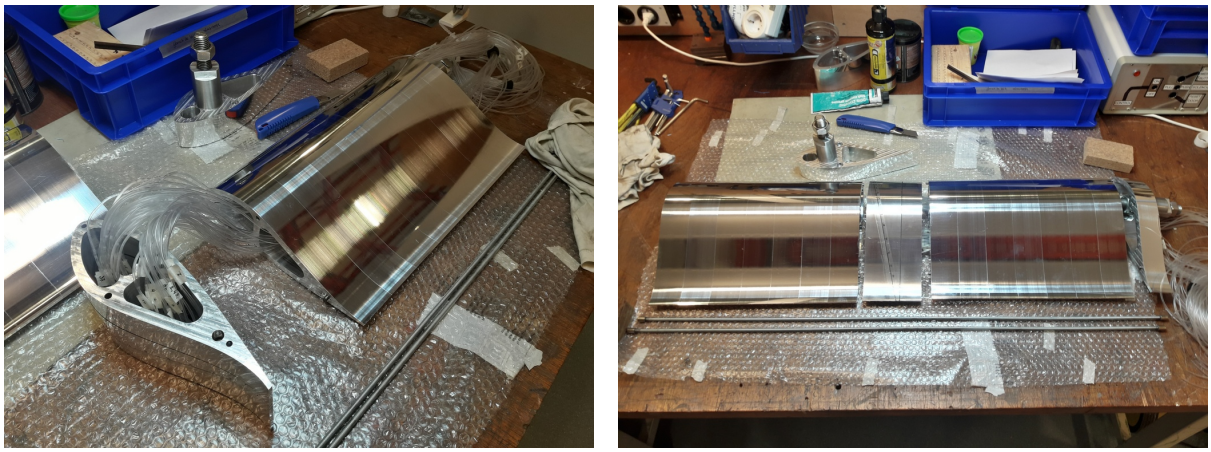

Figure 4.17: Wing assembly: (l) Routing of tubing through the wing. (r) Final assembly of the wing.

Installation in test section

The wing is installed in the open test section of the wind tunnel in the Engineering Fluid Dynamics laboratory. Wherefor plywood end-plates, enclosing the wing in the test section, are manufactured using laser cutting (Figure 4.18(l)). The plates are finished by painting and sanding to assure a smooth wall surface near the wing.

Installation of the wing is done from below by lifting the wing through the end-plate cut outs and hanging it on the top mounting point using the M20 suspending rod (see Section 4.2.1). The bottom mounting point is subsequently moved under the wing after which the wing is fixed from below by adjusting the M20 rods accordingly (Figure 4.18(m)). The mounting points are secured and the PVC tubes coming from the pressure tabs are routed to the pressure scanners which finishes the installation.

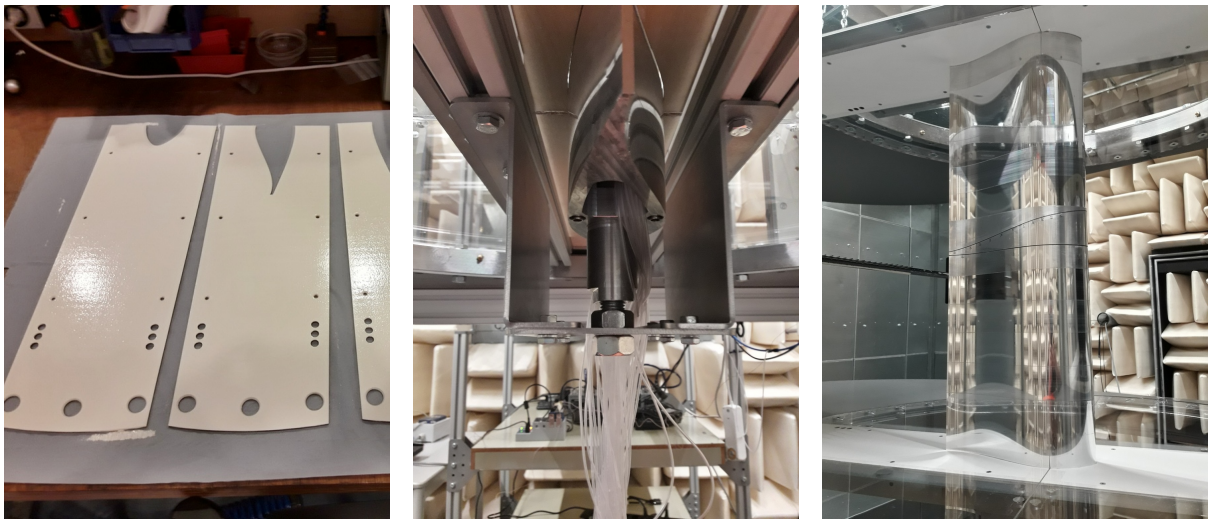

Figure 4.18: Wooden end-plates enclosing the wing in the test section (l). Installing the wing in the test section from below (m) and the wing suspended in the test section enclosed by the wooden end-plates (r).

5 Experimental work

5.1 Wind tunnel

The "silent" wind tunnel at the department of Engineering Fluid Dynamics at the University of Twente is used for all experiments in this thesis. The wind tunnel is of an closed return, open-jet, type of which the open-jet test section is situated in an anechoic chamber with dimensions $6 \times 6 \times 4$ m. The test section cross sectional area is 0.63 m^2 with a width×height of 900×700 mm (Figure 5.4). The air is propelled by a 1250 mm radial fan powered using a 132kW electric motor which allows for a maximum test section velocity of 60 m/s with a maximum turbulence intensity $I \equiv u'/U$ of 0.08% [12]. A schematic overview of the wind tunnel facility and the test section is shown in Figures 5.1 and 5.4.

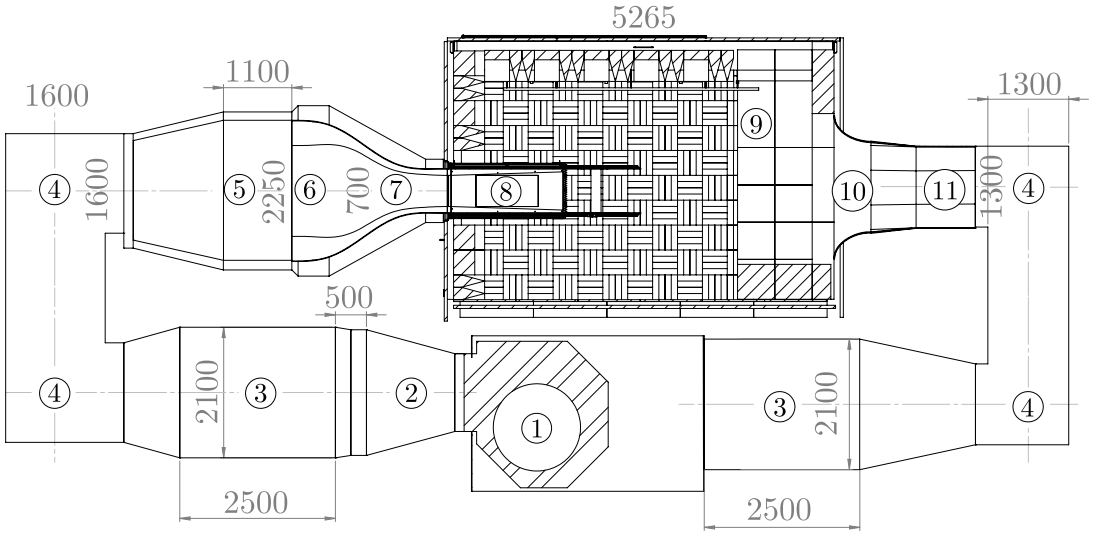

Figure 5.1: Overview of the University of Twente wind tunnel facility: (1) Centrifugal fan. (2) Heat exchanger. (3) Acoustic baffles. (4) 90° guide vanes. (5) Settling chamber. (6,7) 10:1 contraction. (8) Test section. (9) Anechoic chamber. (10,11) Bell mouth shaped collector. Figure courtesy of de Santana et al. [12]

5.2 Experimental setup

The experimental setup, shown in Figures 5.2 5.3 and 5.4, consists of the airfoil model (1) suspended vertically in the open test section connected to the tunnel jet. The jet dynamic pressure ($q_0 = \frac{1}{2}\rho U^2$) is measured using a pitot-static tube (2a), suspended 185 mm from the top in the middle of the jet, connected to a pressure transducer (2b). Temperature of the air stream is measured using two thermocouples (3) in the stream located on the left and right side of the jet at 40 mm from the wall. Signals of the pitot-static tube and thermocouples are connected to an NI cDAQ-9174 data acquisition chassis (4) with suitable I/O modules which in turn are connected to an NI PXI-1024Q data acquisition computer (5). The relative humidity of the air in the anechoic chamber is measured using a humidity probe (10) positioned in the test cell.

The surface pressures on the model are measured using the 47 pressure tabs. Tubes from all circuits are connected to three of five NetScanner 9116 pressure scanners (6) which are coupled in a local network with the NI PXI-1024Q computer using a simple RS232 hub (14). A wake rake (8) is used to measure the loss in stagnation pressure downstream of the airfoil. 21 pitot tubes distributed over a width of 300 mm ($\Delta y = 15$ mm) are connected to the remaining two NetScanner pressure scanners. All signals are processed using the National Instruments LabVIEW software which both monitors and collects the data. The angle of attack is changed by manually rotating the tooted plates suspending the wing in the tunnel (9).

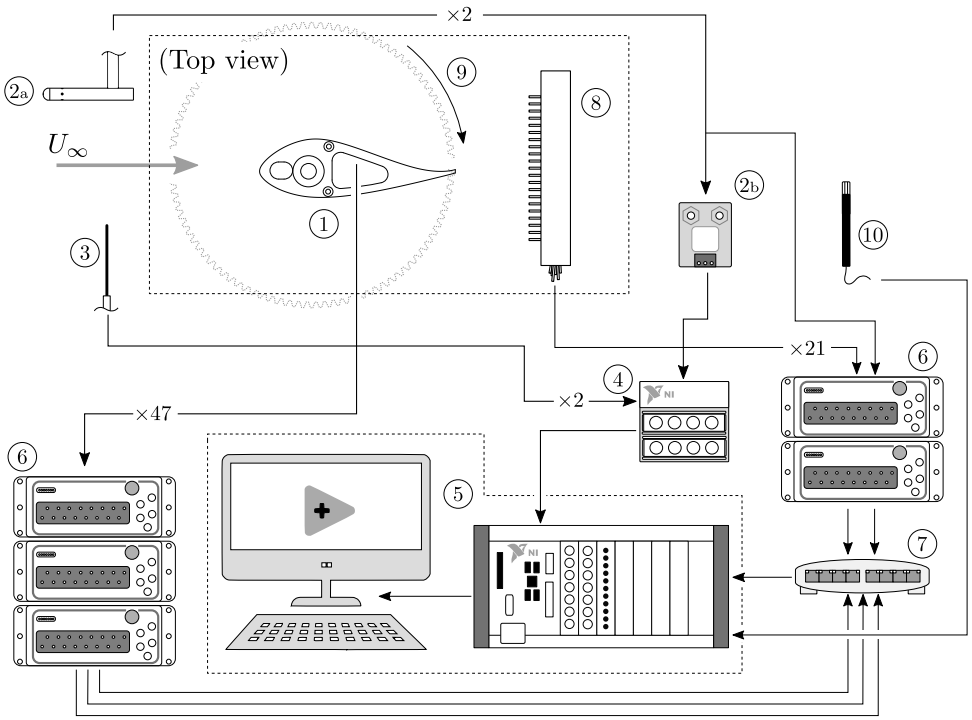

1.	Wing section with 48 pressure tabs	6.	NetScanner 9116 pressure scanners
2a.	Pitot tube	7.	RS232 network hub
2b.	Pressure transducer	8.	Wake rake with 21 pressure tabs
3.	Thermocouple	9.	Toothed disks suspending wing
4.	National Instruments cDAQ-9174	10.	Rotronic Humidity probe
5.	NI PXI-1024Q Computer & LabVIEW®		

Figure 5.2: Overview of the experimental setup showing all equipment. Numbers indicating the describe components will be used throughout this chapter.

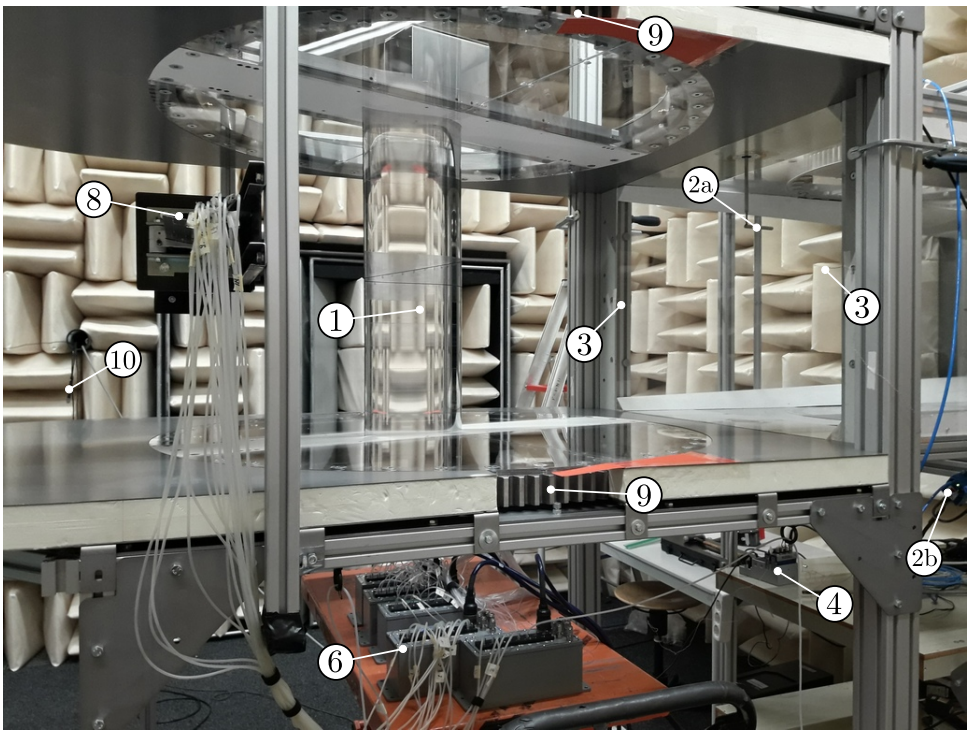

Figure 5.3: Picture of measurement setup inside anechoic chamber. Numbers correspond to the overview given in Figure 5.2. The data acquisition computer, number (5), is situated outside the anechoic chamber and the RS232 hub, number (7), is outside this picture.

The leading edge of the wing is positioned 665 mm from the jet exit as shown Figure 5.4. The measurement section containing the 47 pressure taps is positioned at $h/2 = 350\,\text{mm}$ from the floor/ceiling as well as the pitot tubes of the wake rake. The rake is positioned at 260 mm ($= 1.04c$) from the trailing edge. Figure 5.4 shows the dimensions of the setup and wake rake installation.

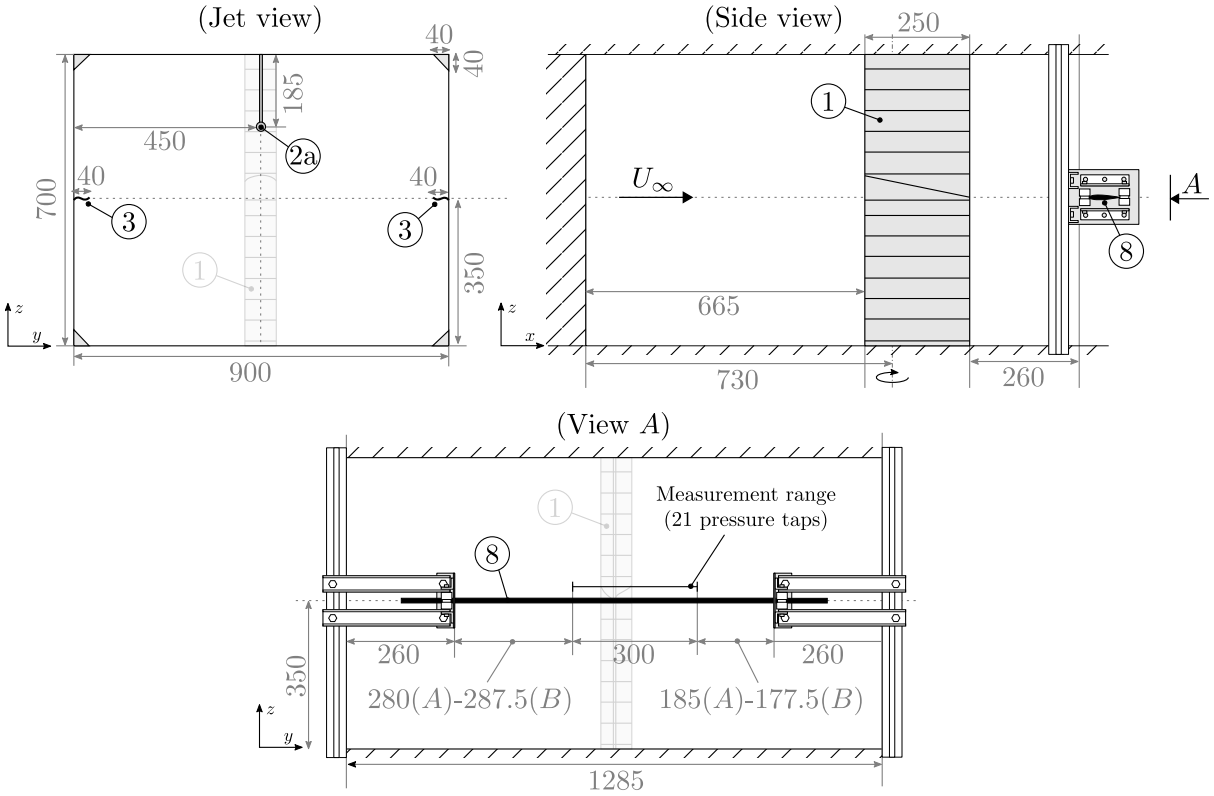

Figure 5.4: Jet, test section and wake rake installation dimensions. Again numbers correspond to the overview given in Figure 5.2.

To increase the measurement resolution the rake is let to traverse $\Delta y/2 = 7.5\,\text{mm}$ in the y-direction in two discrete positions, doubling the resolution. Two adjusters are fixed on both side of the wake rake allowing one to move the rake using two M4 bolts (Figure 5.5). Two measurements denoted as A and B are subsequently taken and combined to obtain a 42 point reading over a range of 307.5 mm.

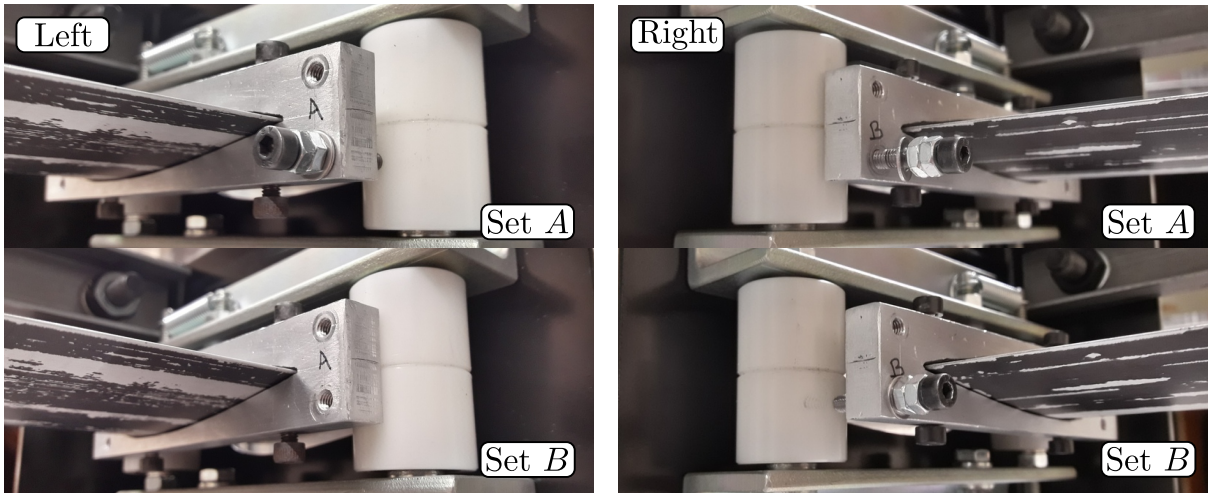

Figure 5.5: Adjusting the wake rake: (l) Left side of the wake rake (top side airfoil) showing the adjuster for setting either measurement set A or B (bold in = A). (r) Right side of the wake rake.

5.3 Equipment specifications

5.3.1 Pressure

Free stream pressures

The dynamic pressure in the jet is measured via a pitot tube suspended in the free stream at 185 mm from the top and 450 mm from the side walls. The differential pressure between the static and stagnation tap of the pitot tube are connected to two sensors: An AE Sensors DPTI/CXLdp low pressure differential transmitter and a Measurement Specialties™ NetScanner™ 9116 pressure scanner. Two sensors are used to allow compensation for differences in sensor calibration. The technical properties of both sensors are summarized in Table 5.1

Table 5.1: Specifications of dynamic pressure sensors

Parameter	Sensor Type	Range	Accuracy	Output
Dynamic pressure	AE DPTI/CXLdp	+2,500 Pa	±0.25%FS (±6.3 Pa)	0-10 VDC
Static/Stagnation pressure	NetScanner™ 9116	±6,894 Pa (1.0 psi)	±0.15%FS (±10.3 Pa)	TCP-IP

Surface pressures

Surface pressures over the airfoil are measured using three Measurement Specialties™ NetScanner™ 9116 pressure scanners, each consisting of 16 silicon piezoresistive pressure transducers. Two scanners have a full scale range of ±1.0 Psi (±6895 Pa). One has a range of ±2.5 Psi (±17237 Pa). The sensors have a TCP-IP data output providing the readings in engineering units (kPa) directly. Multiple scanners are placed in a local network and connected to the data acquisition system.

To prevent the measured pressures to exceed the specified range of the sensors. Pressure taps No. $1-16$ and $33-47$ are connected to a ±1.0 Psi scanner and the surface pressures at the leading edge $(17-32)$ are connected to a ±2.5 Psi version. The maximum possible pressure coefficient C_p is considered at $U_\infty = 60$ m/s which corresponds to $\mathrm{Re}_c = 0.99{\times}10^6$ for a chord length of 250 mm. The upper limit for the ±1.0 Psi pressure scanner is $C_{p,\mathrm{lim}} = -3.2$ and for the ±2.5 Psi version it is $C_{p,\mathrm{lim}} = -8.0$. As the ranges differ accuracies of the surface pressure readings vary. Table 5.2 gives details on the accuracy of each type of scanner.

Table 5.2: Specifications of surface pressure sensors

Parameter	Sensor Type	Range	Resolution	Accuracy
Surface pressure	NetScanner™ 9116	±6,894 Pa (1.0 psi)	±0.003 %FS (±0.2 Pa)	±0.15 %FS (±10.3 Pa)
		±17,236 Pa (2.5 psi)	±0.003 %FS (±0.5 Pa)	±0.15 %FS (±25.9 Pa)

Cp accuracy

The surface pressure readings are converted to the pressure coefficient $C_p = 2(p-p_\infty)/(\rho U_\infty^2)$ as function of the free stream velocity and fluid density. The accuracy of the used sensors is converted to a ΔC_p considering air at 20°C ($\rho = 1.2047\,\mathrm{kg/m^3}$) at varying free stream velocities. The accuracy in C_p reduces with the square of the velocity increase.

Table 5.3: C_p accuracy of pressure sensors at $U_\infty = 60$ m/s and $\rho = 1.2047$ kg/m^3.

Sensor type	Accuracy	$\Delta C_p \times 10^3$ at U_∞			
		10 m/s	20 m/s	40 m/s	60 m/s
AE DPTI/CXLdp	±6.3 Pa	±104	±25.9	±6.49	±2.88
NetScanner™ 9116 (1.0 psi)	±10.3 Pa	±180	±42.8	±10.7	±4.75
NetScanner™ 9116 (2.5 psi)	±25.9 Pa	±430	±108	±26.9	±11.9

5.3.2 Temperature

Temperature of the free stream is measured using two standard K-type thermocouples suspended in the jet at both 40 mm from the left and right side of the tunnel walls. Accuracy of K-type thermocouples at temperatures between $-40°$C and 375°C are $\pm 2.2°$C. Variation in temperature throughout the free stream are assumed to be negligible such that the measured temperature is considered the average temperature in the stream.

5.3.3 Relative humidity

The relative humidity, defined as the ratio (expressed as percentage) of the actual vapour pressure over the saturation vapour pressure at a given temperature, is measured using a Rotronic HC2-WIN-USB humidity probe. The unit has a measurement range of 0-100%RH from $-40°$C till $+85°$C and an accuracy of ± 2%RH and $\pm 3°$C at 23°C.

5.3.4 Ambient pressure

The ambient pressure is not measured directly in the tunnel. Instead barometer measurements at the local weather station (KNMI Vliegveld Twente 52°16'N 6°54'E), updated every 10 minutes at www.knmi.nl/nederland-nu/weer/waarnemingen, are consulted prior each measurement. The readings have a 10 Pa resolution of which the error is assumed negligible.

5.3.5 Tripping device

To force transition of the boundary layer from laminar to turbulent, simulating the effect of increasing surface roughness due to fouling (as explained in Section 4.1.1), tripping of the boundary layer is required. To trip the boundary layer a two or three-dimensional artificial roughness of height k is applied at a given location on the surface. Zigzag tape is most commonly used for this purpose as explained in Section 4.1.1 (see Figure 4.4). To this end the roughness Reynolds number Re_k is defined as [23, 56]:

$$\mathrm{Re}_k \equiv \frac{u_k k}{\nu} \tag{5.1}$$

Where u_k is the velocity at height k at the location of the roughness and ν is the kinematic viscosity of the fluid. The value of Re_k at which transition is triggered immediately is termed the *critical roughness Reynolds number*, Re_{kc}. It ranges from approximately $\mathrm{Re}_{kc} = 50$ to $\mathrm{Re}_{kc} = 800$ depending on the roughness type used. Zigzag tape was first mentioned by Hama [23] and induces three-dimensional vortex loops in the flow, triggering transition directly at the tapes location. The value of Re_{kc} for zigzag tape is estimated to lie around $\mathrm{Re}_{kc} = 50$ [23, 56].

The thickness used during the experiments is 0.3 mm such that $k = 3{\times}10^{-6}$ m and is applied at $0.05c$ from the leading edge ($(x, y) = (12.5, 0.3){\times}10^{-3}$m). Streamwise velocity at that location, for $\mathrm{Re}_c = 0.87{\times}10^{6}$[1] and $\alpha = 0°$, is estimated by approximating the boundary layer velocity profile by the method of Pohlhausen [44] (consulted from [20]) who approximates the dimensionless velocity profile $f(\eta) = f(y/\delta(x))$ by the following 4^{th} order polynomial:

$$f(\eta) = 2\eta - 2\eta^3 + \eta^4 + \Lambda\left(\frac{\eta}{6} - \frac{\eta^2}{2} + \frac{\eta^3}{2} - \frac{\eta^4}{6}\right) \quad \text{for} \quad \begin{cases} f(\eta) \in [0, 1] \\ \eta \in [0, 1] \\ \Lambda \in [-12, 12] \end{cases} \tag{5.2}$$

Where Λ, the Pohlhausen parameter can be determined from the boundary layer shape parameter $H = \delta^*/\theta$ such that $H = H(\Lambda)$:

$$H(\Lambda) = \left(\frac{3}{10} - \frac{\Lambda}{120}\right) / \left(\frac{37}{315} - \frac{\Lambda}{945} - \frac{\Lambda^2}{9072}\right) \tag{5.3}$$

[1] The maximum obtained Reynolds number during the experiments (see Section 5.6.1)

XFOIL is consulted to find H at the chordwise location $x/c = 0.05$ at $\mathrm{Re}_c = 0.87{\times}10^6$ and $\alpha = 0°$. The boundary layer parameters found using the `VPLO` routine are as follows:

$$\begin{aligned} &\delta^* = 29.58{\times}10^{-5}c, \quad \theta = 12.62{\times}10^{-5}c \\ &H = 2.3440, \qquad\quad U_e = 1.2028U_\infty \end{aligned} \quad \text{for} \quad \begin{cases} U_\infty = 52.4\,\mathrm{m/s} & \alpha = 0° \\ \nu_{20°\mathrm{C}} = 15.06{\times}10^{-6}\,\mathrm{m^2/s} & x/c = 0.05 \\ c = 0.25\,\mathrm{m} \end{cases} \tag{5.4}$$

By substituting $H = 2.3440$ in Equation (5.3) and solving for Λ we find two solutions, one of which is unphysical as $\Lambda \notin [-12, 12]$. The physical solution is found to be $\Lambda = 5.5998$ which, when substituted in Equation (5.2), yields the dimensionless velocity profile $f(\eta)$. The profile is made dimensional by stating:

$$y = \eta\delta(x) \quad \text{and} \quad u(y) = (0.99U_e) f\left(\frac{y}{\delta}\right) U_\infty \tag{5.5}$$

Which requires the boundary layer thickness $\delta = y(0.99U_e)$ for which the following relations are known in terms of the Pohlhausen parameter Λ and the displacement and momentum thickness δ^* and θ respectively:

$$\begin{aligned} \delta^* &= \delta \int_0^\infty (1 - f)\, d\eta = \delta \left(\frac{3}{10} - \frac{\Lambda}{120}\right) \\ \theta &= \delta \int_0^\infty f(1 - f)\, d\eta = \delta \left(\frac{37}{315} - \frac{\Lambda}{945} - \frac{\Lambda^2}{9072}\right) \end{aligned} \tag{5.6}$$

Both relations from (5.6) can be used to find δ allowing to compute (5.5). Figure 5.6 plots the boundary layer velocity profile $u(y)$ against the distance from the surface y together with the roughness height $k = 0.3\,\mathrm{mm}$. The intersection of both curves indicates the streamwise velocity at the roughness height location $u_k = 36.4\,\mathrm{m/s}$.

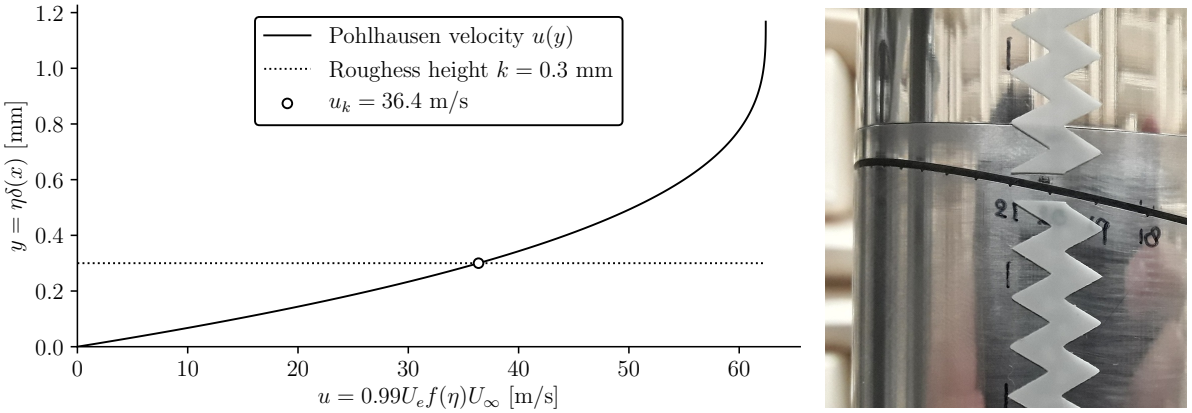

Figure 5.6: (l) Boundary layer velocity profile at $x/c = 0.05$ by the Pohlhausen method. (r) Zigzag tape applied to the model

The velocity u_k allows the roughness Reynolds number Re_k to be computed as:

$$\mathrm{Re}_{k=0.3\mathrm{mm}} = \frac{36.4(0.3{\times}10^{-3})}{15.06{\times}10^{-6}} = 725.1 \tag{5.7}$$

Which is (significantly) larger than the critical roughness Reynolds number $\mathrm{Re}_{kc} \approx 50$ for zigzag tape as estimated by Hama [23]. This allows the assumption that laminar-turbulent transition of the boundary layer occurs immediately at the location of the zigzag tape. As $\mathrm{Re}_k > \mathrm{Re}_{kc}$ an increase in drag is expected due to the roughness applied. The minimum height required for immediate transition using zigzag tape ($\mathrm{Re}_k = \mathrm{Re}_{kc} = 50$) was found to be $k = 0.072$ mm. Thinner tapes, although commercially available, were however not present within the EFD laboratory.

5.4 Data reduction

The experiments are carried out at relatively low wind speeds (60 m/s max.) where the influence of compressibility is negligible. The most important parameter describing the type of flow around airfoil is the chord Reynolds number which is defined as:

$$\mathrm{Re}_c = \frac{\rho U_\infty c}{\mu} = \frac{U_\infty c}{\nu} \tag{5.8}$$

Where ρ is the free stream density, U_∞ is the jet velocity, c is the chord length of the airfoil (0.25 m), μ is the dynamic viscosity of the free stream and $\nu = \mu/\rho$ is the kinematic viscosity. None of these parameters can be measured directly and thus need to be deduced from quantities that we can measure.

5.4.1 Dynamic viscosity

The dynamic viscosity of air may safely be assumed to behave as a function of temperature only for which a good approximation is given by Sutherland's law [58]:

$$\frac{\mu}{\mu_0} = \left(\frac{T}{T_0}\right)^{3/2} \frac{T_0 + S}{T + S} \quad \text{with} \quad \begin{cases} \mu_0 = 1.7894{\times}10^{-5} & \text{kg/(ms)} \\ T_0 = 273.11 & \text{K} \\ S = 110.56 & \text{K} \end{cases} \tag{5.9}$$

Where μ_0 and T_0 are a reference viscosity and temperature and S is the so called *Sutherland temperature*. T is the measured temperature of the air stream in Kelvin.

5.4.2 Density

The density must be computed from a gas law. In these experiments the density of air is determined by considering moist air of which the relative humidity RH is measured. Multiple relations exist for computing the density of moist air. In these experiments the formula for calculating the density of moist air by Picard et al. in the CIPM-2007[2] [43] is used:

$$\rho_\infty = \frac{pM_a}{ZRT}\left[1 - x_v\left(1 - \frac{M_v}{M_a}\right)\right] \quad \text{where} \quad \begin{cases} M_a = 28.96546{\times}10^{-3} & \text{kg/mol} \\ M_v = 18.01652{\times}10^{-3} & \text{kg/mol} \\ R = 8.314472 & \text{J/(molK)} \end{cases} \tag{5.10}$$

Here p and T are the static pressure and temperature in the stream. M_a and M_v are the molar masses of dry air and water vapour respectively and R is the universal gas constant. Z is the compressibility factor which for low speeds (Ma$<$ 0.3) can be considered equal to unity. x_v is the molar mass fraction of water vapour in the air which is determined from the relative humidity RH by the following relation [43]:

$$x_v = hf(p,T)\left[\frac{p_{sv}(T)}{p}\right] \tag{5.11}$$

Where $h = RH/100\%$ is the relative humidity expressed as fraction, $f(p,T)$ is the enhancement factor for which the following relation is given

$$f(p,T) = \alpha + \beta p + \gamma T^2 \quad \text{with} \quad \begin{cases} \alpha = 1.00062 & \\ \beta = 3.14{\times}10^{-8} & \text{Pa}^{-1} \\ \gamma = 5.60{\times}10^{-7} & \text{K}^{-2} \end{cases} \tag{5.12}$$

and p_{sv} is the saturation vapour pressure for water in air for which the following formula gives a good approximation:

$$p_{sv}(T) = \exp\left[AT^2 + BT + C + D/T\right] \quad \text{with} \quad \begin{cases} A = 1.2378847{\times}10^{-5} & \text{K}^{-2} \\ B = -1.9121316{\times}10^{-2} & \text{K}^{-1} \\ C = 33.93711047 & \\ D = -6.3431645{\times}10^{3} & \text{K} \end{cases} \tag{5.13}$$

[2] CIPM: *Comité International des Poids et Mesures* (English: International Committee of Weights and Measures)

In the relations for $x_v, f(p,T)$ and $p_{sv}(T)$ the temperature is measured by thermocouples suspended in the stream. The ambient pressure p can be taken from measurements of a local weather station where we make the assumption that the ambient pressure outside is equal to the pressure in the wind tunnel.

5.4.3 Free stream velocity

The last variable in the Reynolds number definition is the jet velocity U_∞ which can be determined from the Bernoulli equation:

$$p_0 = p_\infty + \frac{1}{2}\rho U_\infty^2 \quad \rightarrow \quad U_\infty = \sqrt{\frac{2(p_0 - p_\infty)}{\rho}} = \sqrt{\frac{2q_0}{\rho}} \tag{5.14}$$

Where the dynamic pressure $q_0 = \frac{1}{2}\rho_\infty U_\infty$ is measured from the pitot-static tube.

5.4.4 Lift, pressure drag and moment coefficient

Calculation of the section lift and pressure drag is done by numerically integrating the measured surface pressures on the airfoil perimeter as briefly explained in Section 3.2.3. To this end the normal and axial components of the resultant force, N and A respectively, are determined after which the lift and drag forces are determined using Equations (3.12) and (3.13). The whole procedure for numerically integrating the pressures over the airfoil surface, using both a trapezoidal rule or a modified version of the Simpson rule is discussed in Appendix (B).

5.4.5 Total drag coefficient

The airfoil drag is determined by calculating the momentum deficit in the wake measured by the pitot tubes in the wake rake. Section 3.2.4 described the mathematical details on this procedure. To compute however the pressure coefficient in the wake C_{pw} (Equation (3.31) but repeated here for convenience),

$$C_d = \frac{2}{c}\int_w \left(\sqrt{C_{pw}} - C_{pw}\right) dy_1 \quad \text{where} \quad C_{pw} \equiv \frac{H_1 - p_\infty}{q_0} = \frac{H_1 - p_\infty}{\frac{1}{2}\rho U_{\infty,w}^2} \tag{3.31}$$

the dynamic pressure q_0 is <u>not</u> measured from the pitot-static tube but taken from the wake rake itself. As the jet velocity U_∞ changes slightly when air moves over the wing correct integration of the momentum deficit in the wake requires U_∞ to be known at the wake rake location, so $U_{\infty,w}$. Figure 5.7 shows a measured C_{pw} distribution at two distinct angles of attack with both the $C_{p\infty}$ measured at the pitot-static tube (at measurements A and B) and $C_{pw\infty}$ at the wake rake. The free stream velocity increases slightly as the air moves over the wing resulting in $C_{pw\infty} < C_{p\infty}$.

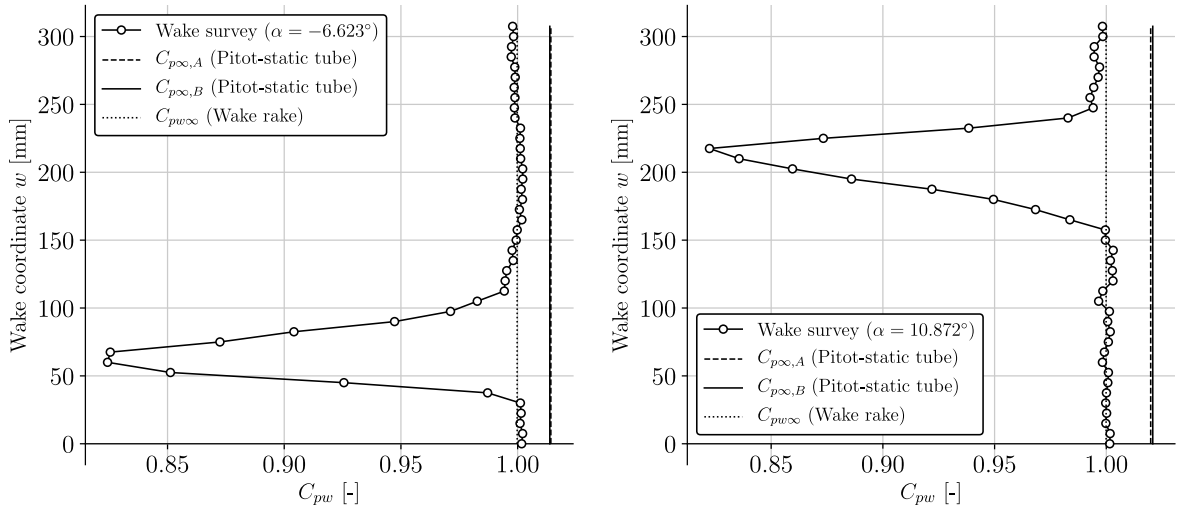

Figure 5.7: Differences in free stream velocity U_∞ at two angles of attack shown as variations in $C_{pw\infty}$.

The $C_{pw\infty}$ at the wake rake location is taken as the algebraic average C_{pw} of the two outer measurement probes so,

$$C_{pw\infty} = \frac{C_{pw,1} + C_{pw,N}}{2} \quad \text{where} \quad \begin{cases} N = 21 & \text{for } A \text{ or } B \text{ only} \\ N = 42 & \text{for } A \text{ and } B \end{cases} \tag{5.15}$$

To numerically perform the integration in Equation (3.31) first the measurements of set A and B are combined to give a resolution of $dw = 7.5$ mm. When the full set of total pressure measurements at the wake rake exists integration via either the trapezoidal rule or the (classical) Simpson rule can commence. C_d in case of both methods is approximated as follows:

$$C_d \approx \sum_{i=1}^{N-1} dC_{di} \quad \text{where} \quad \begin{aligned} dC_{di} &= \frac{2}{c}\left(\sqrt{\bar{C}_{pwi}} - \bar{C}_{pwi}\right) dw_i \qquad \text{for } \bar{C}_{pwi} > 0 \\ dC_{di} &= \frac{2}{c}\left(-\sqrt{|\bar{C}_{pwi}|} - \bar{C}_{pwi}\right) dw_i \quad \text{for } \bar{C}_{pwi} < 0 \end{aligned} \tag{5.16}$$

In case of the trapezoidal rule the terms $\bar{C}_{pwi}$ and dw_i are computed as:

$$\bar{C}_{pwi} = \frac{1}{2}\left(C_{pwi} + C_{pwi-1}\right) \quad \text{and} \quad dw_i = w_i - w_{i-1} \tag{5.17}$$

When using the Simpson rule these terms are computed differently.

$$\bar{C}_{pwi} = \frac{1}{6}\left(C_{pwi} + 4C_{pwi-1} + C_{pwi-2}\right) \quad \text{and} \quad dw_i = w_i - w_{i-2} \tag{5.18}$$

Since 42 total pressure taps are used, so N is even, the last part of the integral, between $N-2$ and $N-1$ is performed using a trapezoidal rule. Also the summation for approximation of C_d starts at $i = 2$.

5.4.6 Boundary corrections

Flow conditions in wind tunnels differ from those in unbounded streams. The presence of walls (or stationary fluid in case of an open test section) confine the air stream, producing lateral flow boundaries at finite distances from the model. Flow boundaries cause a variety of effects on the flow. When considering a two-dimensional situation these include [7]:

- *Horizontal buoyancy* refers to the change in static pressure in the streamwise direction over an empty test section. It produces a drag force similar to the hydrostatic force on bodies subjected to a uniform gravitational field. In open test sections this effect may become negligible [13]
- *Solid blockage* is the relative size of the test object to the wind tunnel test section which was briefly toughed upon in Section 4.2.1. This ratio is usually chosen between 0.01-0.10 with 0.05 being a typical value. The blockage of an object in the tunnel causes the incoming flow velocity to change locally around the object. The resulting effect in open test sections in a reduction in surface stresses
- *Wake blockage*, a somewhat similar effect as solid blockage, is the effect the wake has on the change in velocity locally around and downstream of the object under test. In open test sections this effect is often considered negligible as the jet is free to expand.
- *Streamline curvature* refers to a change in curvature of the flow stream-lines about the object under test compared to the those in the corresponding free stream condition. The resulting effect in an open test section is a decrease in moment coefficient, lift coefficient and angle of attack (C_m, C_l, α).
- *Normal downwash change* is the alteration to the component of induced flow in the direction of lift due to finite distances of the boundaries (quiescent fluid in an open section). In an open section the effect results in lower lift and larger drag because of a larger downwash compared to conditions in an unbounded stream.

In order to obtain results valid for unbounded streams, measurements in wind tunnels should be corrected for (most of) these effects. Correction models based on potential flow theory have been developed for open-jet wind tunnels by Glauert [22] and Brooks et al. [10]. Both authors use approximately the same derivation however the method of representing of the airfoil is different; Glauert utilized a line vortex at the centre of pressure while Brooks uses a vortex sheet along the camber line. The results are a correction to the angle of attack and the drag while assuming equal lift measured in the open-jet wind tunnel and real life conditions, $C_l = C_{lt}$.

We define

$$\sigma = \frac{\pi^2}{48}\left(\frac{c}{h}\right)^2 \tag{5.19}$$

Where c is the chord and h is the tunnel height[1]. The following effective angle of attack (in radians) follows then from Brooks et al. [10]

$$\alpha = \alpha_t - \frac{\sqrt{3\sigma}}{\pi}C_{lt} - \frac{2\sigma}{\pi}C_{lt} - \frac{4\sigma}{\pi}C_{m\frac{1}{4}t} \tag{5.20}$$

$$C_{dp} = C_{dpt} + \left(-\frac{\sqrt{3\sigma}}{\pi}C_{lt}\right)C_{lt} \tag{5.21}$$

α and α_t represent the effective and measured (tunnel) angle of attack. C_{lt} is the measured section lift coefficient and $C_{m\frac{1}{4}t}$ the measured moment coefficient around the 1/4-chord. C_{dp} and C_{dpt} represent the corrected and tunnel pressure drag. Results from Faleiros et al. [19], who measured drag, lift and effective angle of attack by using PIV measurements, show that the correction on the angle of attack by the method of Brooks et al. is fairly accurate (difference $< 1°$).

5.5 Experimental procedure

Monitoring and recording of the pressures, temperatures and relative humidity is done with the help of National Instruments LabVIEW® installed on the NI PXI-1024Q data acquisition computer. Next to that some of the data reduction steps are performed consecutively in LabVIEW® during the measurements such to control the boundary conditions (predominantly the Reynolds number) during tests.

Prior a test the airfoil is set at the desired (geometric) angle of attack and the position of the wake rake (A or B) is noted. The air velocity is increased until the desired Reynolds number is roughly reached. The jet temperature is let to stabilize before the values of ambient pressure p_∞ and relative humidity RH are manually inputted in LabVIEW®. Fine tuning of the tunnel velocity is done to obtain the desired Reynolds number as accurately as possible. In each measurement data is collected for 30 seconds at a sampling frequency of 10 Hz yielding 300 data points per measurement. Figure 5.8 gives an overview of the data streams during the experiments.

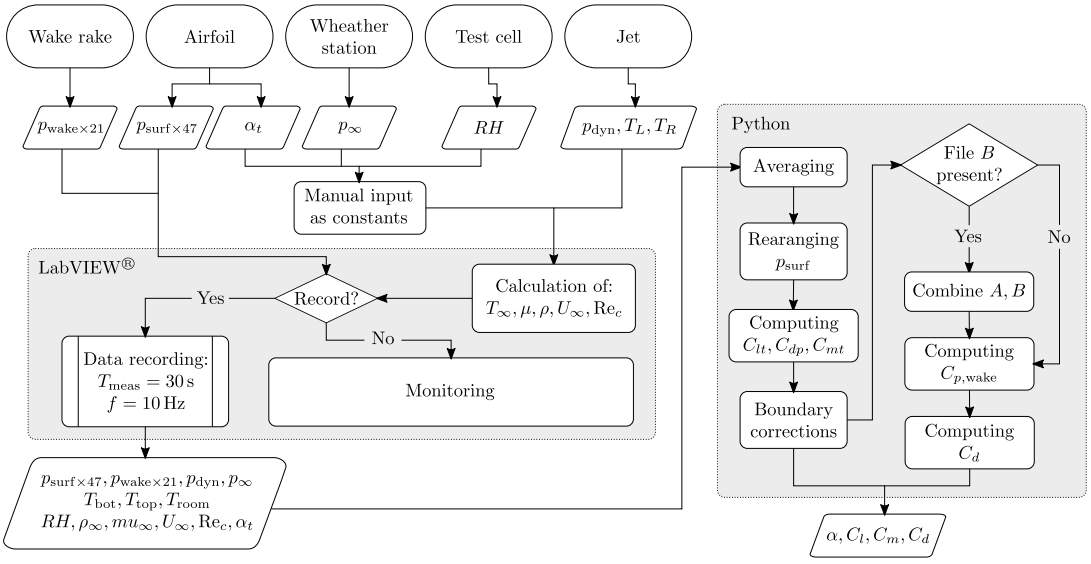

Figure 5.8: Data streams during experiments

After data has been collected in LabVIEW® it is stored as a `.txt` file on the computer of which the structure is explained in Appendix C. Further data processing is performed with Python in which the aerodynamic variables are calculated. Samples of the most important pieces of Python code are given in Appendix B.

[1] The definition of tunnel height h in an open test section may be subject to debate as no solid boundary is present and the jet is free to expand. Nevertheless in these boundary corrections the tunnel height is taken equal to the jet width (900 mm) considering the object is positioned vertically in the test section.

5.6 Measurement results

This section presents results of the measurements after data reduction and post-processing. Notable findings in the data are discussed and graphs are shown comparing the measured data with simulations by XFOIL at corresponding Reynolds numbers. Four datasets at Reynolds numbers of 870,000 and 350,000, in conditions of both free and forced boundary layer transition have been measured. In case of forced transition turbulence is enforced from $0.05x/c$ on the suction side. The boundary layer on the pressure side of the airfoil is left to transition naturally. So summarizing:

(*a*) $\mathrm{Re}_c = 0.87{\times}10^6$ free/natural transition. Angles of attack α between $-12.8°$ and $25.3°$.

(*b*) $\mathrm{Re}_c = 0.87{\times}10^6$ forced transition at suction side at $0.05x/c$. α between $-14.5°$ and $21.9°$.

(*c*) $\mathrm{Re}_c = 0.35{\times}10^6$ free/natural transition. α between $-8.8°$ and $17.1°$

(*d*) $\mathrm{Re}_c = 0.35{\times}10^6$ forced transition at suction side at $0.05x/c$. α between $-8.8°$ and $17.6°$

Key aerodynamic performance figures of all measurements are summarized in Tables 5.4, 5.5 and 5.6 together with data from XFOIL, Timmer and van Rooij [60] and Baldacchino et al. [6]. Tabulated data of the four datasets mentioned can be found in Appendix E.

Table 5.4: Key performance figures measured at $\mathrm{Re}_c = 0.87{\times}10^6$ *compared to reference data.*

	XFOIL		Measured		Timmer et al.		Baldacchino et al.	
$\mathrm{Re}_c{\times}10^{-6}$	0.87		0.87		3.00		2.00	
Transition	Free	Forced	Free	Forced	Free	Forced	Free	Forced
$C_{l,\max}$	1.75	1.49	1.37	1.00	1.56	1.16	1.53	1.11
α at $C_{l,\max}$	13.8°	15.0°	12.9°	9.1°	12.3°	9.0°	12.3°	9.2°
$(C_l/C_d)_{\max}$	91.3	55.1	77.9	40.0	98.0	52.6	90.5	50.0
α at $(C_l/C_d)_{\max}$	10.3°	7.3°	8.0°	6.4°	9.3°	6.2°	9.3°	6.2°
α at $C_l = 0$	$-2.2°$	$-2.1°$	$-2.3°$	$-2.1°$	$-2.3°$	$-2.0°$	$-2.2°$*	$-1.9°$*

*By extrapolation

Table 5.5: Key performance figures measured at $\mathrm{Re}_c = 0.35{\times}10^6$ *compared to XFOIL predictions.*

	XFOIL		Measured	
$\mathrm{Re}_c{\times}10^{-6}$	0.35		0.35	
Transition	Free	Forced	Free	Forced
$C_{l,\max}$	1.68	N.A.	1.38	0.89
α at $C_{l,\max}$	14.5°	N.A.	13.4°	8.1°
$(C_l/C_d)_{\max}$	64.5	36.7	52.5	31.6
α at $(C_l/C_d)_{\max}$	10.8°	7.0°	10.3°	6.4°
α at $C_l = 0$	$-2.0°$	$-2.4°$	$-1.7°$	$-1.9°$

The reductions in aerodynamic performance by the effects of simulating leading edge roughness are summarized in Table 5.6. The observed reductions correspond very well with the reference data. The relative reductions in maximum lift coefficient $C_{l,\max}$ and maximum lift-over-drag ratio $(C_l/C_d)_{\max}$ at $\mathrm{Re}_c = 0.87{\times}10^6$ agree with the values found at the TU Delft. Reductions found at $\mathrm{Re}_c = 0.35{\times}10^6$ are found to deviate more from the reference data. Relative reductions of $C_{l,\max}$ in XFOIL at $\mathrm{Re}_c = 0.35{\times}10^6$ could not be obtained as no maximum lift coefficient is predicted (see Section 5.6.2).

Table 5.6: Performance reductions due to boundary layer tripping at $0.05x/c$.

	XFOIL		Measured		Timmer et al.	Baldacchino et al.
$\mathrm{Re}_c{\times}10^{-6}$	0.35	0.87	0.35	0.87	3.00	2.00
$C_{l,\max}$	N.A.	-15%	-36%	-27%	-26%	-27%
α at $C_{l,\max}$	N.A.	$+1.2°$	$-5.3°$	$-3.8°$	$-3.3°$	$-3.1°$
$(C_l/C_d)_{\max}$	-43%	-40%	-40%	-49%	-46%	-45%
α at $(C_l/C_d)_{\max}$	$-3.8°$	$-3.0°$	$-3.9°$	$-1.6°$	$-3.1°$	$-3.1°$

5.6.1 Reynolds number: 870,000

The highest obtainable Reynolds number during experiments for the desired angles of attack was limited to $0.87{\times}10^6$ corresponding to a jet velocity of approximately 52 m/s at air temperatures between 18°C and 20°C. Deflection of the wake downstream of the wing limits the maximum air speed for the given maximum power delivered by the wind tunnel fan (132 kW).

Lift and drag polars

Figure 5.9 shows the lift and drag polars at $\mathrm{Re}_c = 0.87{\times}10^6$ in both free and forced transition conditions cross-plotted with results obtained from XFOIL. The maximum lift coefficient $C_{l,\max}$ under free transition conditions was found to be 1.374 and dropped to 1.002 (-26%) when forcing the transition location at $0.05x/c$ due to the effects of early boundary layer separation, a decay comparable with the reference data (see Section 4.1.1).

Because of the premature transition and corresponding increase in momentum thickness θ stall takes place earlier from 12.9° to 9° ($-2.9°$) in tripped conditions. An increase in drag is observed when tripping the boundary layer as θ is increased (heavily) by the presence of the (relatively thick, 0.35 mm) zigzag tape. The maximum lift-over-drag ratio reduces to 40 in tripped conditions compared to 77.9 in clean state, a reduction of 48% which is comparable to the findings of Timmer and van Rooij and Baldacchino et al. (Section 4.1.1)

The slope of the linear part of the lift characteristic reduces under forced transition conditions due to the smaller extend of laminar flow. Flow separation is initiated at lower angles of attack resulting in lower lift. As the angle of attack increases the separation point moves upstream, increasing the effect resulting in a lift gradient that is less steep.

Measured range, plotted as error bars in the lift polar, under stalled conditions is rather large due to continuous intermittency between detached and attached flow. As explained in Section 4.1.1 the steep decline in lift in the post-stall regime is the result of heavy flow separation, increasing the suction side surface pressure.

The minimum total drag is predicted surprisingly well by XFOIL when compared to the results of the wake survey. In both free and forced transition conditions XFOIL predicts the minimum drag well within the standard deviation of the experimental results. Error bars in the drag polar indicate the sample standard deviation $\pm 1s$ of the measured data, elaborated further on in Section 5.6.3.

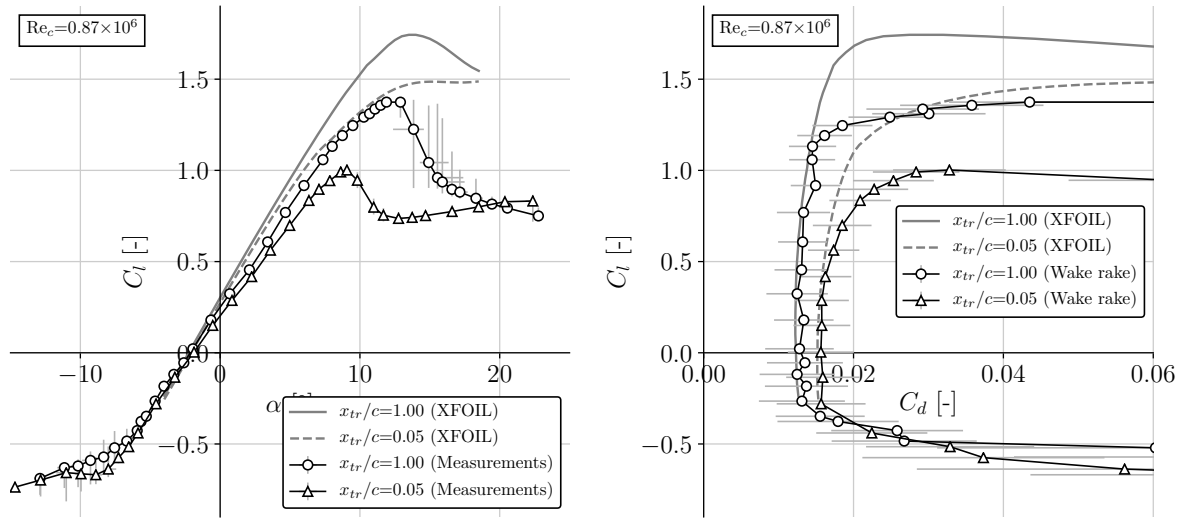

Figure 5.9: Lift (l) and drag (r) polars for $\mathrm{Re}_c = 0.87{\times}10^6$ *in case of free and forced transition cross-plotted with results from XFOIL at the corresponding Reynolds number. Error bars in the lift polar represent the measured range while the error bars in the drag polar represent the standard deviation* $\pm 1s$ *of the measured data (see Section 5.6.3).*

Pressure and total drag

Pressure drag, computed via numerical integration of the surface pressures, is plotted in Figure 5.10 together with the XFOIL prediction[1]. The odd shape of the "drag bucket" is believed to be the result of numerical noise rather than being the actual pressure drag mainly because the pressure drag exceeds the total drag between $C_l \approx 0.45$ and $C_{l,\max}$. Appendix B, Section B.2 discusses the anomalies of determining the drag by integration of surface pressures. Differences in numerical integration scheme did not resolve the found behaviour. Further effort is required to find the exact cause(s) of the anomalies in the pressure drag characteristic.

.

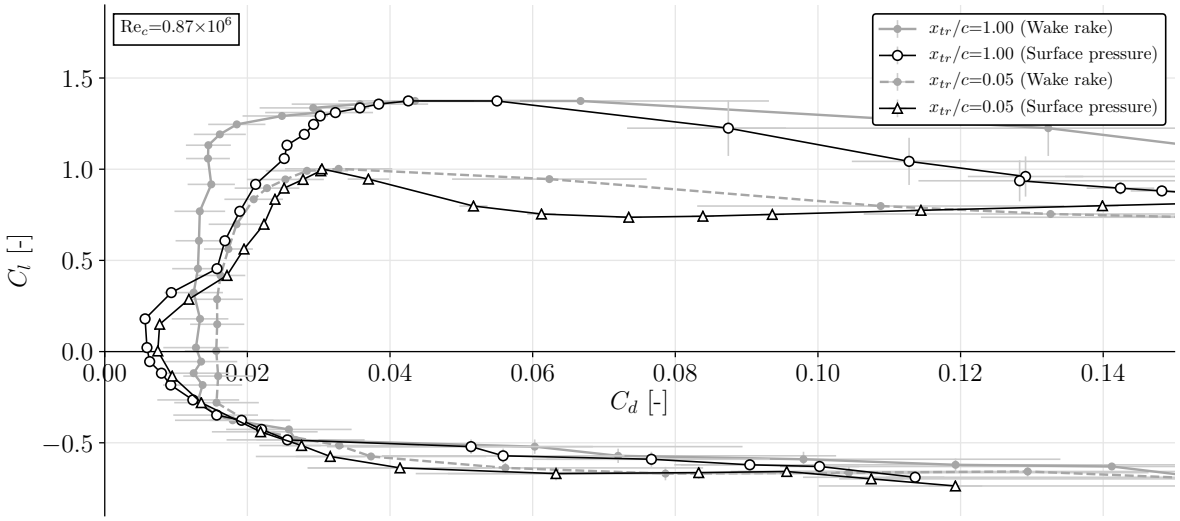

Figure 5.10: Pressure drag C_{dp} computed via numerical integration of surface pressures and total drag C_d determined using the wake survey as shown in Figure 5.9(r). Pressure drag values shown have been computed using the trapezoidal rule.

5.6.2 Reynolds number: 350,000

Next to measurements at $\mathrm{Re}_c = 0.87{\times}10^6$, tests at a Reynolds number of $\mathrm{Re}_c = 0.35{\times}10^6$ were performed corresponding to a jet velocity of about 21 m/s at air temperatures between 18°C and 20°C. This Reynolds number was chosen as attached flow was still maintained at slightly negative angles of attack combined with the possibility of XFOIL solutions to converge. At lower Reynolds numbers XFOIL would not give converged solutions at $\alpha < 0$ inhibiting any comparison.

Lift and drag polars

Figure 5.11 shows the measured lift and drag polars at $\mathrm{Re}_c = 0.35{\times}10^6$ compared to predictions by XFOIL. Immediately one notices a hysteresis regime at low and negative angles of attack occurring both in free and forced transition conditions which is discussed in more detail hereafter. The maximum lift coefficient $C_{l,\max}$ at free transition was found to be 1.38 occurring at an angle of attack of 19.5°. Tripping the boundary layer again at $0.05x/c$ yields a drop in $C_{l,\max}$ of 36% to 0.886 at an angle of attack of 8.1°. The drop in maximum lift coefficient is accompanied with a significantly smoother stall behaviour yielding an almost constant lift coefficient in the post stall regime.

Under forced transition conditions the flow starts to separate gradually from the trailing edge moving upstream as the angle of attack increases as shown in Figure 5.12(r) (see Appendix F for more pressure distribution plots). Simultaneously the suction peak at the leading edge increases, hereby compensating for the loss in lift due to flow separation resulting in an almost constant lift with varying angle of attack. This behaviour is predicted rather well by XFOIL apart from the significantly higher lift.

[1] XFOIL computes pressure drag not by numerical integration of the surface pressure ($\int p^a ds$) but by means of algebraically subtracting the friction drag from the total drag $C_{dp} = C_d - C_{df}$ as explained in Section 4.1.1

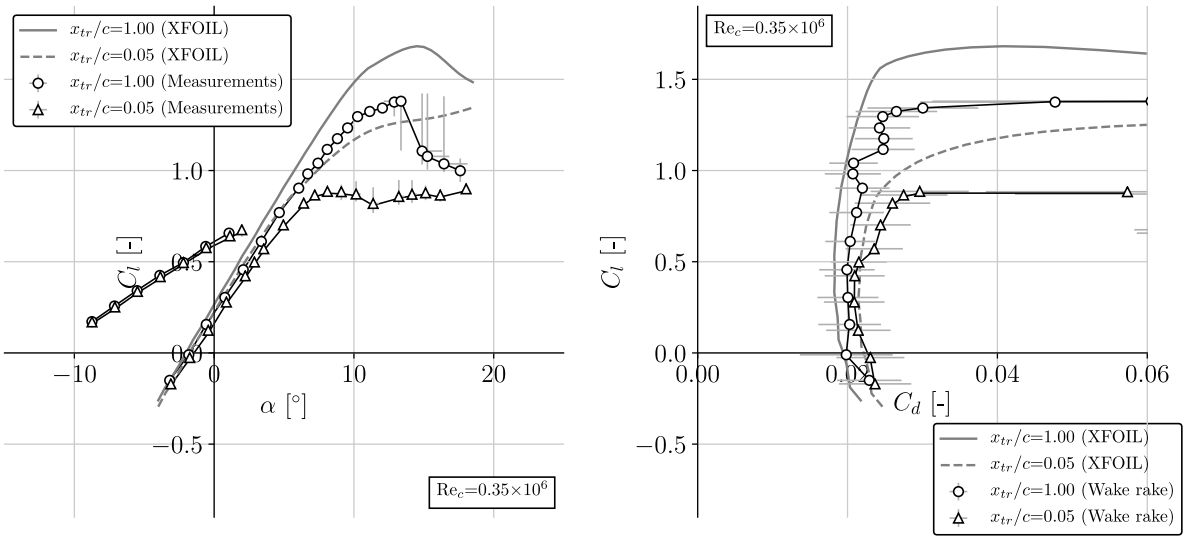

Figure 5.11: Lift (l) and drag (r) polars for $\mathrm{Re}_c = 0.35{\times}10^6$ *in case of free and forced transition cross-plotted with results from XFOIL at the corresponding Reynolds number. Error bars in the lift polar represent the measured range while the error bars in the drag polar represent the standard deviation* $\pm 1s$ *of the range (see Section 5.6.3)*

Hysteresis at low and negative angles of attack

The hysteresis phenomena occurring at low and negative angles of attack is analysed in more detail via the pressure distributions at three approximately constant (effective) angles of attack (Figure 5.12(l)). At $\alpha \approx -3.5°, -2.0°, -0.5°$ the pressure distribution in both the attached and separated state (dashed lines) are shown. The two states were obtained by coincidence as the jet velocity was reduced and increased again in order to adjust the wake rake for each subsequent measurement (see Section 5.2). When approaching the desired Reynolds number from "below" (low $\mathrm{Re}_c \rightarrow$ high Re_c) the bottom surface flow remained separated yielding the dashed pressure distributions in Figure 5.12(l).

If the Reynolds number is increased further bottom surface flow would eventually attach. Probably due to the increase in flow momentum, thinning the boundary layer momentum thickness θ and allowing it to overcome the large adverse pressure gradient. Lowering the Reynolds number again to 350,000 (low $\mathrm{Re}_c \leftarrow$ high Re_c) resulted in the flow remaining attached producing the solid line pressure distributions.

When flow separation occurs at the bottom side the local suction peak (between $0 - 0.4x/c$) and its pressure recovery area ($0.4 - 1x/c$) break down. Lift is increased as the suction peak is reduced. Simultaneously the top side suction peak ($0 - 0.3x/c$) increases, increasing the lift even further. The pressure recovery area on the bottom side vanishes as it is absorbed in the wake. Net effect is a significant lift increase in the opposite direction than intended (Figure 5.11(l)) together with a profound increase in drag as the wake increases in size.

5.6.3 Measurement uncertainty analysis

For each measurement data is collected during a 30 second time frame at a sampling frequency of 10 Hz such that 300 data points for a single measurement are obtained. Each operating condition is measured using both the A and B position of the wake rake (see Section 5.2) yielding a total of 2 times 300 data points per operating condition. Pressure and temperature variations during these measurements result in variability of the calculated lift and drag. Moreover the measurement uncertainties imposed by the sensors used (see Section 5.3) produce an extra uncertainty in the acquired data.

A detailed statistical analysis of the error propagation of sensor uncertainties on the data would be desired at this point. Time constrains in this thesis work prevented such an analysis from being performed though. The variability of sampled data could however easily be shown such that bands of a given confidence level can be drawn around the results.

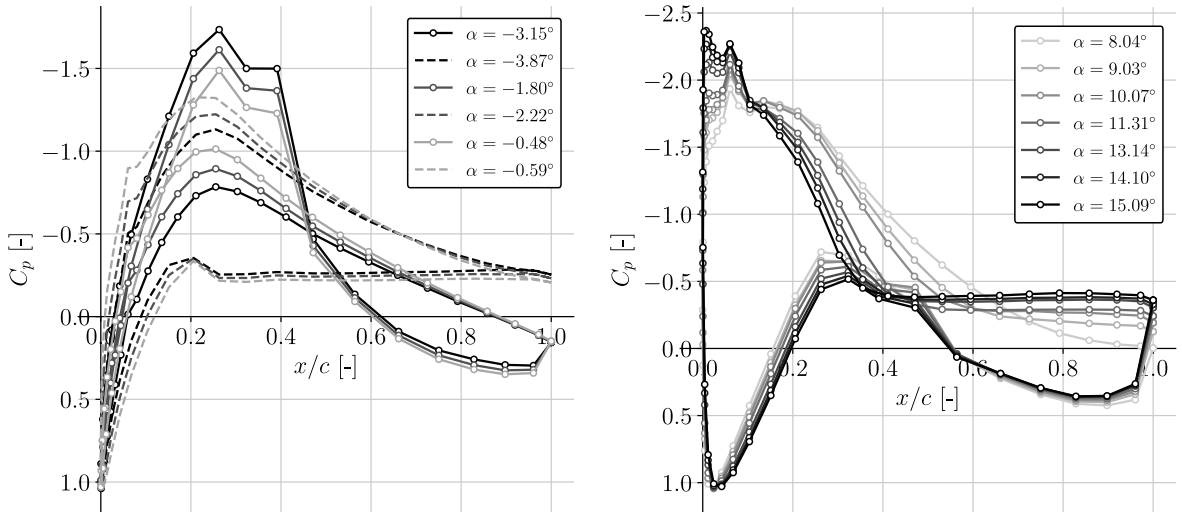

Figure 5.12: (l) Hysteresis phenomena at low and negative effective angles of attack at $\mathrm{Re}_c = 0.35{\times}10^6$ *under clean conditions. Dotted lines are states where flow separation has occurred at the bottom side. (r) Pressure distributions post "stall" in the tripped state where flow separation is initiated in the aft section moving upstream as* α *is increased.*

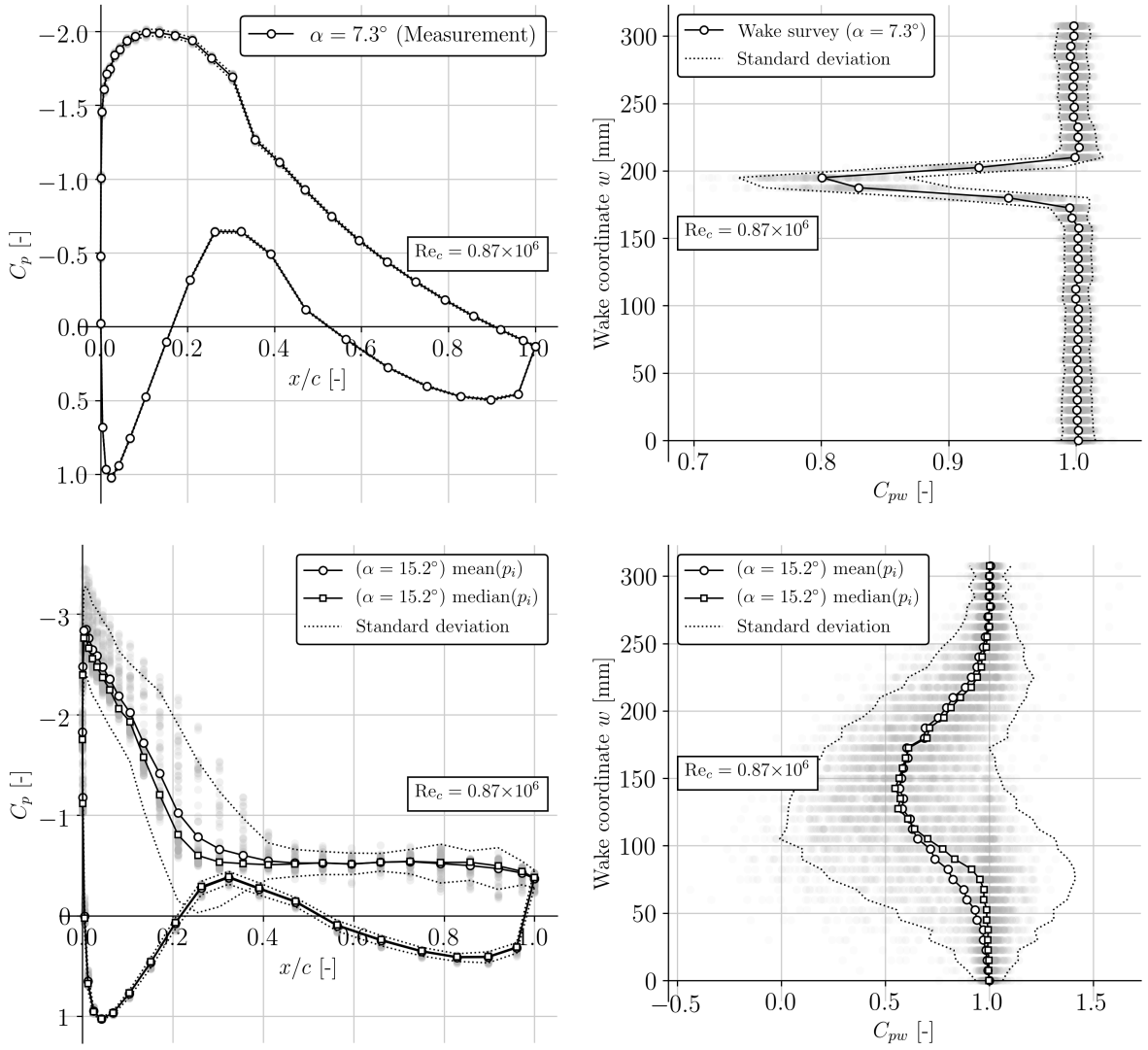

Figure 5.13: Surface pressures (l) and wake pressure (r) measurements at two angles of attack at $\mathrm{Re}_c = 0.87{\times}10^6$ *under free transition conditions showing the individual measurements as grey transparent dots. The dotted lines indicate the 95% confidence band as twice the sample standard deviation,* $\pm 2s$.

In statistics the *sample standard deviation* of data from a population s, in this case measured pressures at a given location p_i, is a measure of the amount variability in the data expressed in the unit of measure. A low standard deviation indicates most sampled values are close to the mean, a large s specifies a greater dispersion. If a *normal distribution of the population is assumed* then 95% of the values tend to fall between $\pm 2s$ from the mean. The sample standard deviation of the measured pressures $s_{\bar{p},i}$ is computed as

$$s_{\bar{p},i} = \sqrt{\frac{1}{N-1}\sum_{j=1}^{N}(p_{i,j} - \bar{p}_i)^2} \quad \text{for} \quad i = \begin{cases} 1...47 \text{ (Surface pressures)} \\ 1...42 \text{ (Wake rake)} \end{cases} \tag{5.22}$$

Where N equals the amount of samples (300) and $\bar{p}_i$, the mean value obtained at each measurement location, is computed as

$$\bar{p}_i = \text{mean}(p_i) = \frac{1}{N}\sum_{j=1}^{N} p_{i,j} \tag{5.23}$$

The dotted lines in Figure 5.13 represent the $\pm 2s$ range around the mean, indicating the region of 95% confidence. At moderate angles of attack (e.g. $\alpha = 7.3°$) the assumption of a normal distribution in the data seems to hold for both the surface and wake pressures such that the sample standard deviation forms a reasonable measure of dispersion. The variability of pressures measured in the wake was found to be much higher compared to the surface pressures.

In the post stall regime, e.g. at $\alpha = 15.2°$ the flow is highly turbulent resulting in violent pressure fluctuations on both the surface as in the wake. Individual data points in the lower plots of Figure 5.13 reveal that the assumption of a normal distribution of the sample data is not really justified. In this case the *median* of individual pressures might be more representative for indicating the "true" pressure. The median is defined as the middle value of the sorted data and is indicated in the plots by square makers. Total drag values C_d (computed from the wake rake) in this thesis have however been computed using the sample mean instead of the median. One can argue whether this is the best method for treating the data.

Because of the intermitted character of the surface pressures in the regime around stall the error bars plotted in the lift and drag polars (Figures 5.9 and 5.11) represent different deviations. The full measured range is plotted in the lift polars as in the stall region ether attached or detached flow is present, inhibiting the assumption of a normal distribution in the data.

In case of the drag polar the data can (roughly) be assumed to form a normal distribution such that ± 1 times the sample standard deviation $s_{\bar{p},i}$ is plotted, indicating a 68% confidence band around the mean. However as discussed above the use of either the mean or median for computing the drag can be a topic of debate.

6 Numerical analysis

6.1 Problem description

A numerical analysis of the DU97-W-300 airfoil is carried out using the commercial CFD software ANSYS Fluent (2019 R1). For the analysis a two-dimensional computational domain is composed including the airfoil and a surrounding far field on which the boundary conditions are imposed. Figure 6.1 gives an overview of the computational domain. The left semi-circular section combined with the top and bottom edge form the *velocity inlet* boundary whereas on the right side a *pressure outlet* boundary condition is imposed. The semi-circular section has a radius of 12.5 m (corresponding to $50c$) with its centre located at the $^1/_4$-chord point. The outlet of the domain extents to 17.5 m downstream the $^1/_4$-chord point which equals $70c$.

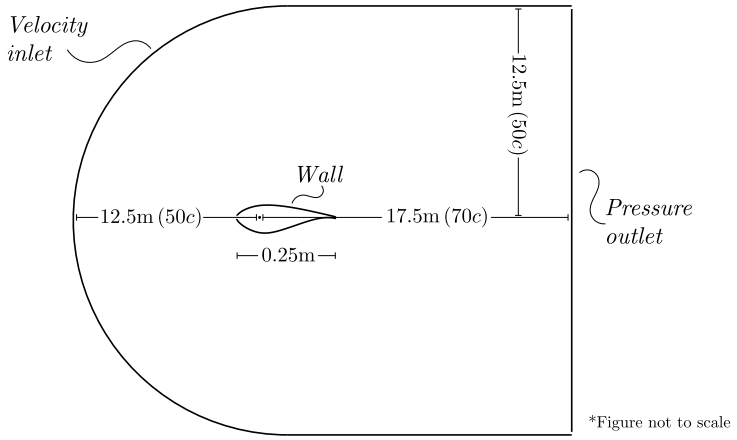

Figure 6.1: Computional domain

6.1.1 Grid generation

The domain is discretized with an O-type quadrilateral grid using ANSYS ICEM CFD. The grid is composed of multiple blocks of which the topology is schematically shown in Figure 6.2. A grid refinement study was carried out to monitor the solution dependency on the grid size. Seven different grid sizes, utilizing the same block-structure, are used of which the properties are summarized in the table in Figure 6.2. A grid size parameter h_k is defined to quantify the cell size of each grid as:

$$h_k = \sqrt{\frac{A_{\text{domain}}}{N_k}} \quad \text{for} \quad A_{\text{domain}} = \pi/2(12.5)^2 + 2(17.5)(12.5) - A_{\text{airfoil}} \tag{6.1}$$

and where N_k is the total number of grid cells on the k^{th} grid. The cell expansion ratio normal to the airfoil surface is set to 1.2 such that increases in cell heights take place gradually.

Grid density near walls

To assure proper calculation of the flow inside the (turbulent) boundary layer a sufficiently high grid resolution near the airfoil surface is required in combination with a suitable turbulence model. To simulate transition from laminar to turbulent flow the *Transition SST (Shear Stress Transport)* turbulence model is used. To obtain an adequate resolution for resolving the viscous sublayer, cells adjacent to the airfoil should be as thick such that the centres are located at a maximum non-dimensional wall distance $y^+ = 1$ [2]. This allows the viscous sublayer, over which the dimensionless flow velocity $u^+ = U/u_\tau$ varies approximately linear, to be solved with sufficient resolution such that the no-slip condition may be directly applied on the wall interface. The cell height Δy of cells adjacent to the walls can be estimated from the definition of non-dimensional wall distance y^+:

$$y^+ = \frac{\Delta y u_\tau}{\nu} \quad \rightarrow \quad \Delta y = \frac{y^+ \nu}{u_\tau} \tag{6.2}$$

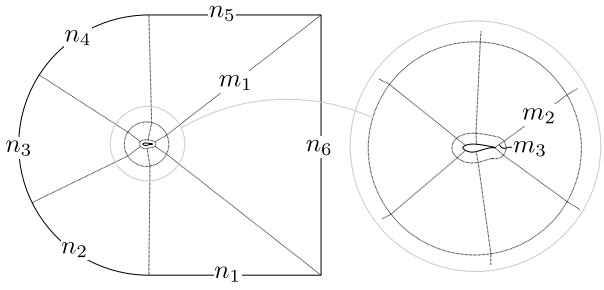

Number of elements and wall spacing

k [−]	h_k [−]	n_{1-6} [−]	m_{1-2} [−]	m_3 [−]	Δy_{wall} [$\times 10^6$ m]
1	0.1548	50	40	20	5.80
2	0.0764	100	80	40	2.90
3	0.0507	150	120	60	1.93
4	0.0380	200	160	80	1.45
5	0.0303	250	200	100	1.16
6	0.0252	300	240	120	1.00
7	0.0094	400	320	160	0.92

Figure 6.2: Topology of the computational grid and grid sizes used in grid refinement study

The friction velocity $u_\tau = \sqrt{\tau_w/\rho}$ is a function of the wall shear stress τ_w which can be approximated using a suitable law for the friction coefficient $C_f = \tau_w/(\frac{1}{2}\rho U^2)$. This work uses the empirical relation of Schlichting [51] (Eq. 21.16) which is strictly valid only for a flat plate boundary layer with zero pressure gradient,

$$C_f = (2\log_{10}(\mathrm{Re}_x) - 0.65)^{-2.3} \quad \text{for} \quad \mathrm{Re}_x < 10^9 \tag{6.3}$$

In the derivation of this relation the boundary layer velocity profiles are assumed similar to those in pipe flow and have been approximated using the universal logarithmic law for use with arbitrarily large Reynolds numbers. The flow in this case is however subject to a pressure gradient as it moves over the airfoil, therefore violating these assumptions.

The relation could nevertheless be used a first approximation, proving an initial Δy, on which an initial solution is computed providing the local C_f and allowing an improved estimate for the locally required y^+ yielding the necessary local Δy. This iterative approach, providing a better grid topology for the boundary layer flow, is however not applied in this thesis.

The Δy is computed using (6.3) utilizing the chord Reynolds number $\mathrm{Re}_c = U_\infty c/\nu$ followed by (6.2). This value is used in the coarsest grid followed by systematic reduction based on the corresponding grid refinement ratio.The table shown in Figure 6.2 shows the cell height adjacent to the surface for each of the used grids. Applying all the settings shown in Figure 6.2 yields the computational grids resembling the one shown in Figure 6.3.

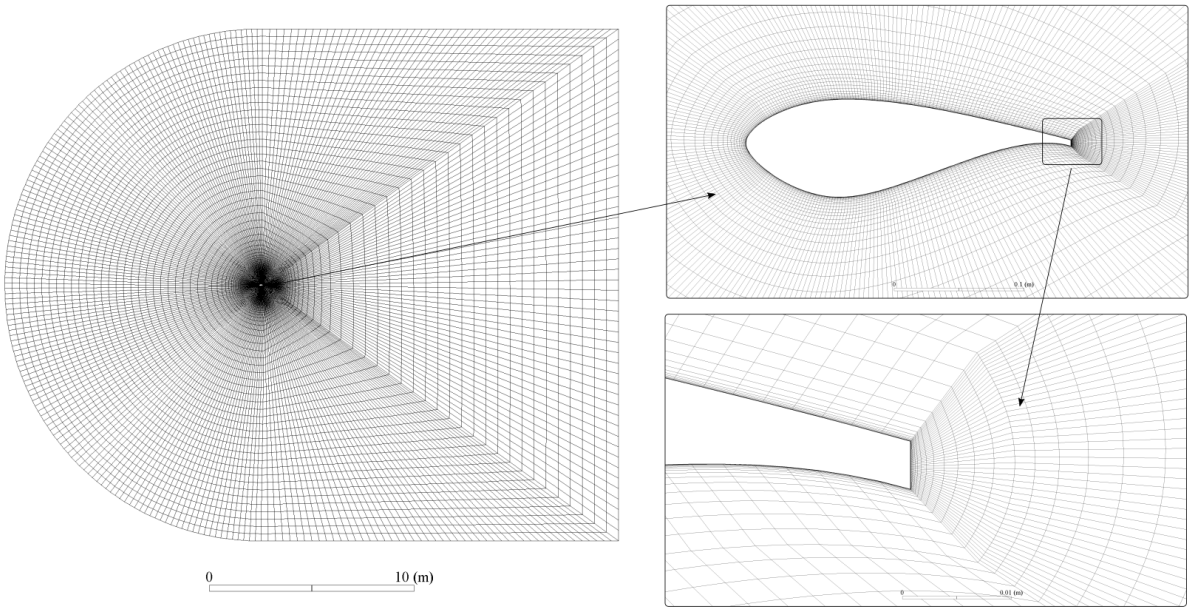

Figure 6.3: Overview of the computational grid $k = 1$ of size $h_1 = 0.1548$ showing details of the airfoil and trailing edge meshes.

Little amount of smoothing has been applied to the computational grids due to problems arising in the regions near the trailing edge. Rather skew cells reside around the trailing edge area as shown in Figure 6.3 causing the various smoothing routines of ANSYS ICEM CFD to worsen the quality of the mesh significantly.

6.1.2 Modelling settings

The governing equations are solved using the Reynolds Averaged Navier-Stokes (RANS) approach considering steady flow and using a pressure-based solver, treating the working fluid as being incompressible. The incompressibility assumption may safely be taken since the Mach number Ma is small such that the relative change in density ρ_0/ρ is only 1.5% in this case [5].

$$\frac{\rho_0}{\rho} = \left(1 + \frac{\kappa - 1}{2}\mathrm{Ma}^2\right)^{\frac{1}{\kappa-1}} \approx 1.015 \quad \text{with} \quad \mathrm{Ma} = \frac{U_\infty}{\sqrt{\kappa R_{\text{air}} T_\infty}} = \frac{60}{\sqrt{1.4(287)(293)}} \approx 0.17 \tag{6.4}$$

Where $\kappa \equiv c_p/c_v$ is the specific heat ratio and $R_{\text{air}} = R/M$ is the specific gas constant of air in $\mathrm{J/kgK^{-1}}$. Heat and mass transfer are neglected in the simulations omitting the need to solve the energy and species transport equations. Air is considered the working fluid of which the properties are given in Table 6.1[2].

Table 6.1: Fluid properties CFD

Property	Unit	Value
Density ρ	$\mathrm{kg/m^3}$	1.1986
Dynamic viscosity μ	Pa·s	1.8133×10^{-5}

The *velocity inlet* boundary condition is defined by a magnitude and direction vector in the absolute reference frame. The backflow direction specification at the *pressure outlet* boundary is given by a direction vector equal the velocity inlet. Free stream turbulence at the inlet is specified by its *intermittency*, *intensity* and *viscosity ratio*. Here intermittence t_t/t_T indicates the relative time at which the flow is turbulent with a given turbulence intensity $I \equiv u'/U$. The (eddy) viscosity ratio μ_t/μ indicates the relative importance of turbulent viscosity over the molecular viscosity of the fluid. Tables 6.2, 6.3 and 6.4 give a summary of the boundary condition settings for the inlet and outlet.

Table 6.2: Velocity inlet properties

Property	Unit	Value
Magnitude (U_∞)	m/s	60
Velocity x-component (u_∞)	-	$\cos(\alpha\pi/180)$
Velocity y-component (v_∞)	-	$\sin(\alpha\pi/180)$

Table 6.3: Pressure outlet properties

Property	Unit	Value
Gauge pressure (p_∞)	Pa	0
Backflow x-component	-	$\cos(\alpha\pi/180)$
Backflow y-component	-	$\sin(\alpha\pi/180)$

Table 6.4: Free stream turbulence properties

Property	Unit	Value
Intermittency ($\gamma \equiv t_t/t_T$)	-	1
Turbulent intensity ($I \equiv u'/U$)	%	5
Turbulent viscosity ratio (μ_t/μ)	-	10

Turbulence model

In order to capture transition from laminar to turbulent flow the *Transition SST (Shear Stress Transport)* turbulence model is applied in the simulations. The Transition SST turbulence model is a 4 equation model solving the transport equations for the turbulent kinetic energy k, specific dissipation rate ω, intermittency γ and for the transition onset criteria in terms of the momentum thickness Reynolds number Re_θ. The model is contains an empirical correlation by Langtry and Menter [33] to cover bypass transition together with flows in low free stream turbulence environments [2].

Certain mesh requirements are advised for the model in order to capture the onset of transition accurately. A maximum y^+ value of 1.0 should be maintained at hard boundaries and a normal cell expansion ratio from the wall outwards of < 1.1 is advised. The sensitivity of the model to streamwise mesh density is found to be low, however if only a single cell happens to be present in the transition region the results are found to deviate some from experimental results [2].

[2] Computed using Equations (5.9) and (5.10) considering $p = 101325$ Pa, $T_\infty = 293.15$ K and $RH = 50$ %.

Solver settings

The simulations are solved with a pressure-based solver following the SIMPLEC algorithm for pressure-velocity coupling. Spatial discretization schemes for the gradient, pressure, momentum and turbulent parameters are given in Table 6.5. The pressure and momentum transport equations are discretized using a 2^{nd}-order accurate scheme whereas the turbulence parameters are all solved using a 1^{st}-order upwind discretization.

Table 6.5: Solver settings

Parameter	Spatial discretization
Gradient (∇)	Least squares cell based
Pressure (p)	2^{nd} order
Momentum (ρu)	2^{nd} order upwind
Turbulent kinetic energy (k)	1^{st} order upwind
Specific dissipation rate (ω)	1^{st} order upwind
Intermittency (γ)	1^{st} order upwind
Momentum thickness Reynolds (Re_θ)	1^{st} order upwind

As a mix exists between both 2^{nd}-order and 1^{st}-order accuracy discretization schemes the formal order of accuracy is first order. As the $\mathcal{O}(h)$ error terms start to dominate only for fine enough grids the resulting rate of convergence is expect to lie between 1 and 2.

Convergence criteria

For evaluating convergence of the simulations the normal, axial and momentum coefficients are used:

$$C_n = \frac{N}{q_0 c}, \quad C_a = \frac{A}{q_0 c}, \quad C_m = \frac{M}{q_0 c^2} \quad \text{with} \quad q_0 = \frac{1}{2}\rho U_\infty^2 \tag{6.5}$$

Where N and A represent the forces normal and parallel the chord line respectively and M represents the moment around the $1/4$-chord point. Simulations are considered converged when no significant variation of each coefficient takes place between iterations. No exact criteria have been used such that manual judgement for simulation convergence is utilized.

6.2 Solution verification - grid refinement study

To verify whether the obtained numerical solutions are reliable a grid refinement study is performed the determine the order of accuracy of the numerical solutions. Multiple solutions have be obtained on increasingly finer computational grids as described in Section 6.1.1. From numerical results the *observed order of accuracy* $\hat{p}$ can be determined after which, using Richardson's Extrapolation technique, an estimate of the exact solution can be made (from Oberkampf and Roy (2010) [42]).

6.2.1 Solution generation

Solution functionals in terms of lift and drag forces are obtained from the pressure distribution over the airfoil surface. To this end the *nodal* static pressure solution at the airfoil boundary p_{surf} is obtained together with the nodal coordinates x, y. Obviously amount of nodes covering the airfoil boundary increases with finer mesh sizes resulting in higher resolution pressure distributions. In ANSYS Fluent solution data in ASCII format is obtained via the `File/Export/Solution data...` routine after which post-processing of the data is performed using Python. An example of pressure and velocity fields obtained from ANSYS Fluent are shown in Figure 6.4.

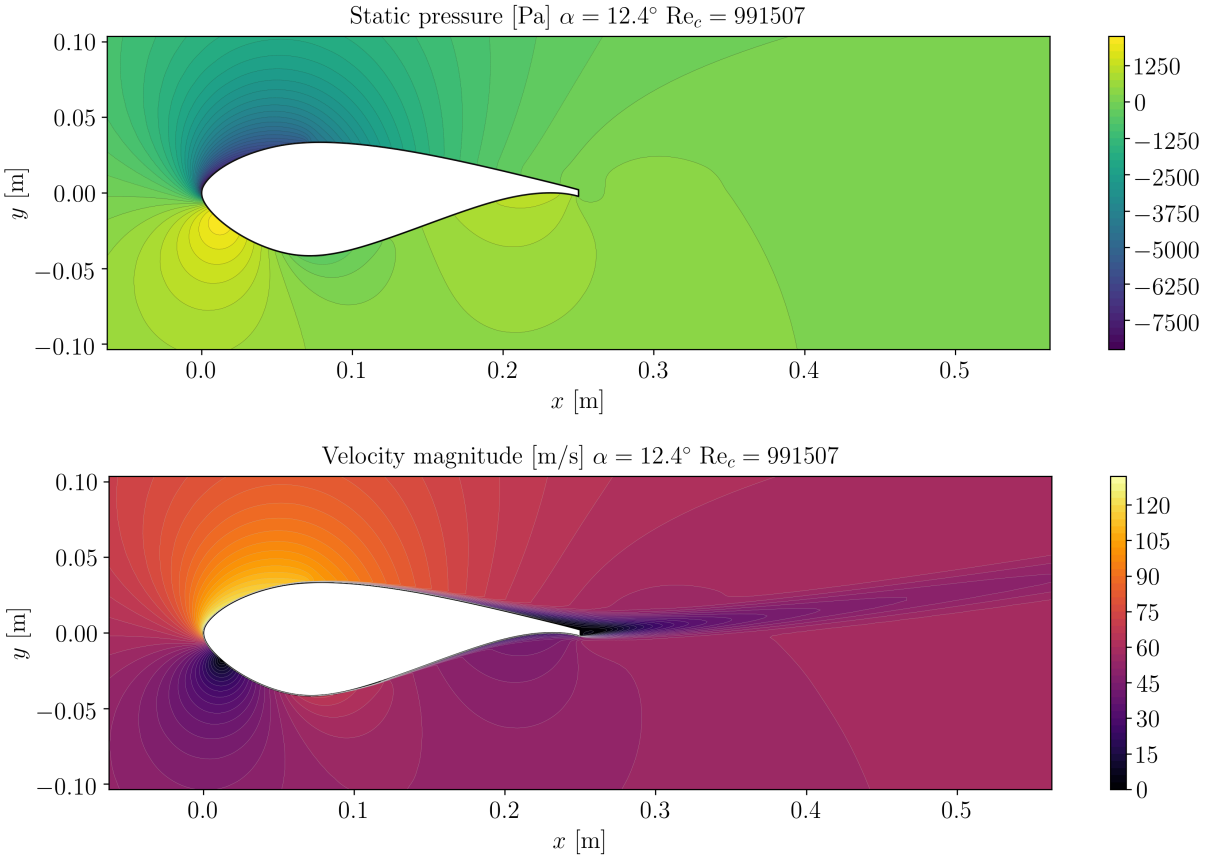

Figure 6.4: Pressure and velocity fields from ANSYS Fluent at $\alpha = 12.4°$ *and* $\text{Re}_c = 991507$ *using Transition SST turbulence model and grid size* $h_4 = 0.038$.

The lift and pressure drag coefficient are again computed via numerical integration of the pressure distribution over the airfoil surface. To this end the surface data from the solution is first rearranged such that points run from the trailing edge over the leading edge down to the trailing edge again. Numerical integration by both the trapezoidal rule and Simpson rule is performed to determine the lift and pressure drag coefficient C_l and C_{dp}.

6.2.2 Rate of convergence

Using solution functionals however to evaluate an order of accuracy can be problematic due to the interplay between errors from determining the functional (e.g. lift/drag), so called *quadrature errors*, and those originating from the numerical scheme discretization, *discretization errors*. Salas and Atkins [50] discuss these problems in detail and suggest that "*the order-of-convergence computed from a norm of the solutions relative error or the functional integrand (e.g. the pressure distribution) is more effective in estimating the average order of convergence, as it is naturally immune to quadrature errors.*"

This suggestion is applied in this work together with the evaluation of solution functionals C_l and C_{dp} by means of numerical integration using both a trapezoidal rule and (modified) Simpson rule (see Appendix B). To compare the computed pressure distribution $p(s)$ on different grid sizes the coarsest grid nodal coordinates are taken as basis of which the finer grid solutions are found by linear interpolation on the corresponding coordinates (Figure 6.5).

As linear interpolation is only first order accurate ($\mathcal{O}(h)$) the approximation of local surface pressures on the finer grids is (negatively) affected. An interpolation method of higher order than the computational scheme could be used such that no the observed rate of convergence not affected. However time constraints on the thesis led for only using a linear scheme to interpolate the surface pressures.

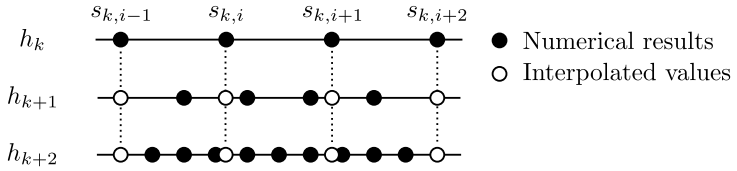

Figure 6.5: Pressure distributions on subsequently finer grids are compared by linear interpolation on the coarse grid coordinates.

After interpolation the relative error norm between pressure distributions $p(s)$ on subsequently finer grids is then determined in the form of an L_2 norm:

$$L_{2(k,k+1)} = \sqrt{\frac{1}{N-1}\sum_{i=0}^{N-1}\left(p_{k,i} - p_{k+1,i}\right)^2} \tag{6.6}$$

where $p_{k,i}$ and $p_{k+1,i}$ are the surface pressures at s-coordinate i on grids with spacing h_k and h_{k+1} where $h_k > h_{k+1}$ as indicated in Figure 6.5 and 6.2. The rate of convergence of the L_2 norm is then determined:

$$\hat{p}_{L2} = \frac{\log\left(L_{2,k}/L_{2,k+1}\right)}{\log\left(h_k/h_{k+1}\right)} \tag{6.7}$$

6.2.3 Observed order of accuracy and exact solution estimation

The *observed* order of accuracy in a grid refinement study is a measure used to asses the level of confidence in the solution estimate obtained via Richardson extrapolation. Ideally the observed order or accuracy should match the formal order of discretization scheme - then one can have high degree of confidence in the solution estimate. Three solutions on systematically refined grids are required to calculate the observed order of accuracy. For this we consider a p^{th}-order accurate scheme with numerical solutions on three grids: fine grid h_1, intermediate grid h_2 and coarse grid h_3. In the case of a constant grid refinement factor r we can find the observed order of accuracy $\hat{p}$ from [42]:

$$\hat{p} = \frac{\ln\left(\frac{f_3 - f_2}{f_2 - f_1}\right)}{\ln(r)} \quad \text{for} \quad r = \frac{h_2}{h_1} = \frac{h_3}{h_2} > 1 \tag{6.8}$$

Where f_1, f_2 and f_3 represent solution functionals (e.g. C_l, C_{dp}) obtained on respectively the fine, intermediate and coarse grid. To estimate then the exact solution Richardson extrapolation's technique is used. To this end two solutions on systematically refined grids with refinement ratio $r = h_2/h_1 > 1$ are used together with the observed order of accuracy $\hat{p}$

$$\bar{f} = f_1 + \frac{f_1 - f_2}{r^{\hat{p}} - 1} \tag{6.9}$$

A more detailed derivation of this equation is given in Appendix H.

6.2.4 Results grid refinement study

The grid refinement study is performed for two cases having a distinct set of boundary conditions. Both cases are intended to simulate flow in the wind tunnel including transition of the boundary layer, possibly causing the formation of laminar separation bubbles (see Section 3.1.4). The characteristic differences between the two cases are summarized in Table 6.6.

Table 6.6: Cases for the grid refinement study

Case	α [°]	Turbulence model	U_∞ [m/s]	Re_c [-]	$C_{l,\mathrm{XFOIL}}$[-]	$C^{\mathrm{TR}}_{l,\mathrm{XFOIL}}$[-]†	$C^{\mathrm{SR}}_{l,\mathrm{XFOIL}}$[-]‡
1	12.4	Transition SST	60.0	991507	1.722	1.729	1.728
2	7.0				1.206	1.214	1.212

†) Via $p(s)$ integration by trapezoidal rule at Re_c with $n = 160$ panels (`PANE` routine applied).

‡) as † but with modified Simpson rule

The results of the grid refinement study include both the pressure distributions and the solution functionals C_l and C_{dp}. Their development with respect to grid refinement is monitored after which the observed order of accuracy $\hat{p}$ is determined for grids of constant grid refinement $r_{k-1,1} \approx 2$. Using $\hat{p}$ an approximation to the exact solution of both C_l and C_{dp} is found using Richardson's extrapolation.

Figures 6.6 and 6.7 shows the development of the pressure distribution of Cases 1 and 2 respectively compared to results from XFOIL. The surface pressures predicted by ANSYS correspond very well with the predictions done using XFOIL. Albeit the surface pressures from XFOIL are predicted slightly lower and higher on the suction and pressure side respectively (presumably due to XFOIL's trailing edge formulation). The time required however for forming a solution in ANSYS is multiple orders of magnitude longer compared to XFOIL ($\mathcal{O}$(hours) vs. $\mathcal{O}$(minutes)) proving that the attractiveness of XFOIL to analyse low-speed flows over airfoils remains evident.

In Figure 6.6, close-up A reveals that XFOIL predicts initiation of the laminar separation bubble earlier compared to ANSYS. This could be due to the differences in free stream turbulence between to two simulations (XFOIL = 0.07%[3] and ANSYS = 5%). However as increasing free stream turbulence should yield earlier transition, and negligible differences in transition location are observed in view B and in Case 2 (Figure 6.7), this theory seems to fail here.

Again the trailing edge formulation from XFOIL seems to have an affect on this phenomena. To investigate this hypothesis a small experiment is performed by the author in XFOIL, artificially thinning the trailing edge. As its thickness is shrunk using the `GDES/TGAP..` routine the resulting effects on the transition location resemble those observed in Figures 6.6 and 6.7. Although this is no definite proof for the discrepancies, it gives an idea of the effect XFOIL's trailing edge formulation on transition prediction.

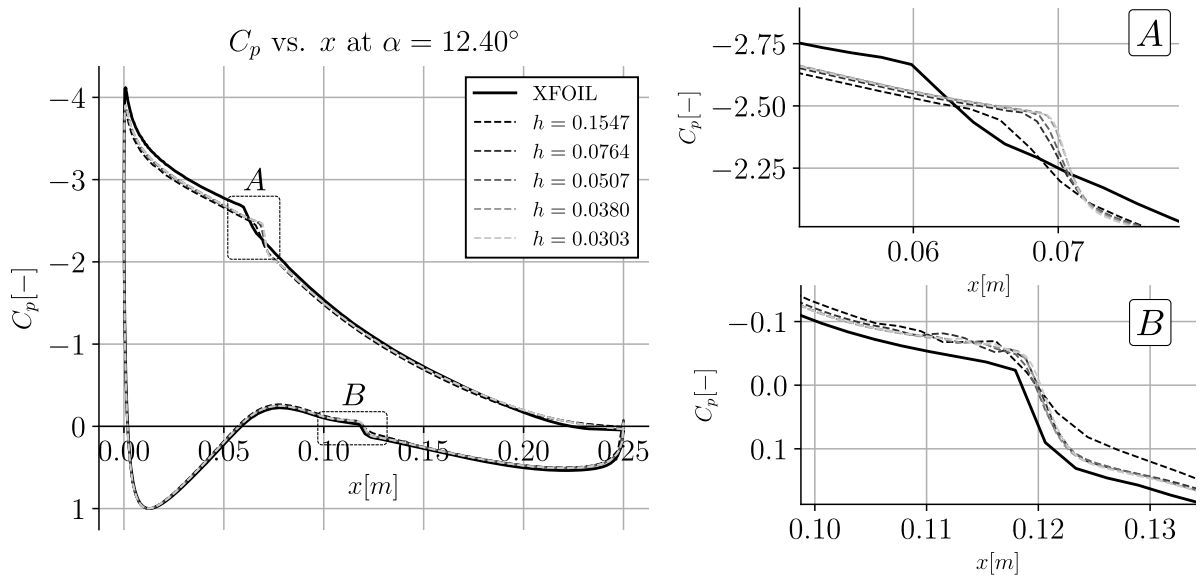

Figure 6.6: Pressure distributions at $\alpha = 12.4°$ for Case 1 computed on subsequently refined grids compared to XFOIL predictions.

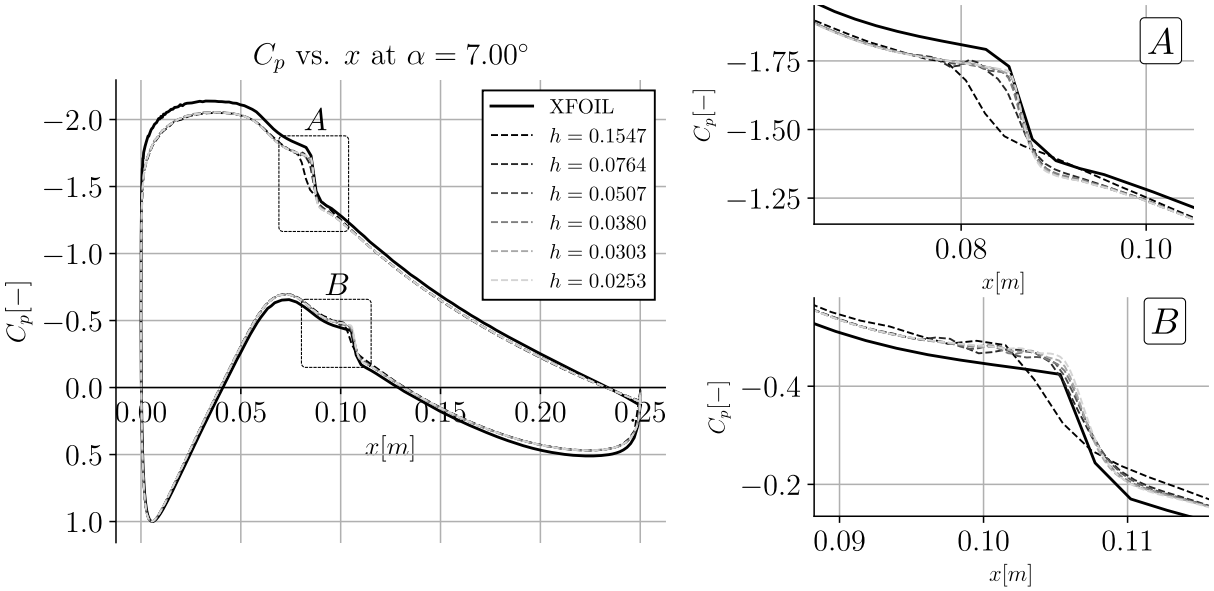

Figure 6.7: Pressure distributions at $\alpha = 7°$ for Case 2 computed on subsequently refined grids compared to XFOIL predictions.

Figure 6.8 shows the development of the lift and pressure drag coefficient and the surface pressure L_2 norm for the two cases. The L_2 norm of the local surface pressures confirms the seemingly convergent behaviour observed in Figures 6.6 and 6.7. The numerical integration scheme's used to compute the lift and pressure drag coefficients could affect the convergence behaviour as discussed by Salas and Atkins [50]. For this reason both the trapezoidal and Simpson scheme are used to compute C_l and C_{dp}.

For Case 2 a third method is utilized to compute the solution functionals using the normal and axial pressure forces $N_(p)$ and $A_{(p)}$ directly from ANSYS Fluent, omitting the need for numerical integration using self written codes. The lift and pressure drag forces are then obtained through Equations (3.12) and (3.13) after which they are made non-dimensional to obtain C_l and C_{dp}.

Despite this, none of the solution functionals C_l, C_{dp}, computed using either the trapezoidal scheme, Simpson rule or from ANSYS directly, seem to converge to a definite value. A decline in lift coefficient is observed in both cases after the fourth grid refinement step at $h_5 = 0.030$ together with an increase in pressure drag coefficient which is referred to as non-monotonic convergence behaviour.

Multiple reasons could exist for non-monotonic convergence (or possibly oscillatory) behaviour of the solution as discussed by Oberkampf and Roy [42]:

- *Non-uniform refinement of the mesh*: Although effort is put in refining the mesh uniformly (notably for meshes $k = 1, 2, 4$) local non-uniformities between subsequent grids might still be present. For instance the cell expansion ratio from boundaries outward is kept at 1.2 for each subsequent grid refinement step which conflicts with the requirement for structural refinement.
- *The asymptotic range of convergence has not been reached* yielding an observed order of accuracy other than the formal order. For a formally 2^{nd} order scheme the asymptotic range is reached when h is sufficiently small such that the error term h^2 dominates yielding an observed rate of convergence around 2. The used mesh sizes are potentially too large for the asymptotic range to be reached.
- *The presence of singularities or non-continuities* can inhibit the computation of a numerical solution as the discretization schemes, and discretziation error estimators, used require the solution to be smooth and differentiable. The discontinuous slope of the trailing edge surface is such an example, possibly having an effect on the observed behaviour.

Other possible causes for the non-monotonic convergence are *effects of velocity field on the applied boundary conditions*. As the airfoil generates lift, circulation is induced in the flow domain deflecting the main stream. Far away from the airfoil deflected flow might conflict with the applied boundary conditions on the domain edges. Furthermore the used *turbulence model might not provide consistent results* on grids that are subsequently (possibly non-uniform) refined.[1]

Non-monotonic convergence is not unique and many scientists and engineers struggle with this problem[1]. Eça and Hoekstra [17] argue that the prominent reason behind "noisy" behaviour of numerical solutions is lack of geometrical similarity between meshes. Furthermore flux limiters, damping functions and switches contained in

[1]Based on oral discussions with dr. E.T.A. van der Weide, Associate Professor EFD group, UT

many modern turbulence models can yield scattering of the solutions. These prevent the valid use of equations (6.7) and (6.8) which require geometrical similar grids with smooth and differentiable solutions.

Moreover Eça and Hoekstra [17] discuss an alternative procedure for the estimation of the numerical uncertainty by grid refinement studies. The authors utilize a least squares fit on four solutions of subsequently refined grids, a technique which could perfectly be used on the data obtained in this thesis. Restrictions in available time however prevented such an analysis to be performed here.

Despite the non-monotonic convergence behaviour observed after the $h_4 \rightarrow h_5$ refinement step, strictly inhibiting the use of Richardson extrapolation for estimating the exact solution, an "engineering approach" is used considering only grids h_1, h_2 and h_4. These grids have a common grid refinement ratio $r = 2$ allowing the use of Equation (6.8) for computing the observed rate of convergence $\hat{p}$ enabling the computation of $\bar{f}$ using Equation (6.9).

Tables 6.7, 6.8 and 6.9 show the observed orders of convergence $\hat{p}$ and the computed estimate for the exact solution based on Richardson extrapolation $\bar{f}$. For both the lift and drag coefficient $\hat{p}$ and $\bar{f}$ are computed providing solutions against which predictions from XFOIL and experimental results can be compared. Observed orders of convergence for the lift coefficient vary between $1.19 - 1.64$ for Case 2 and $0.9 - 1.1$ for Case 1. Using the Simpson rule to compute the force coefficients tends to lower rates of convergence compared to the trapezoidal rule indicating an effect of the quadrature rule on the convergence behaviour. Despite the difference in $\hat{p}$ exact solution estimates of C_l for Case 2 vary only slightly and tend to result in a value of 1.126. For Case 1 the exact value of C_l using the trapezoidal rule is approximated as 1.684.

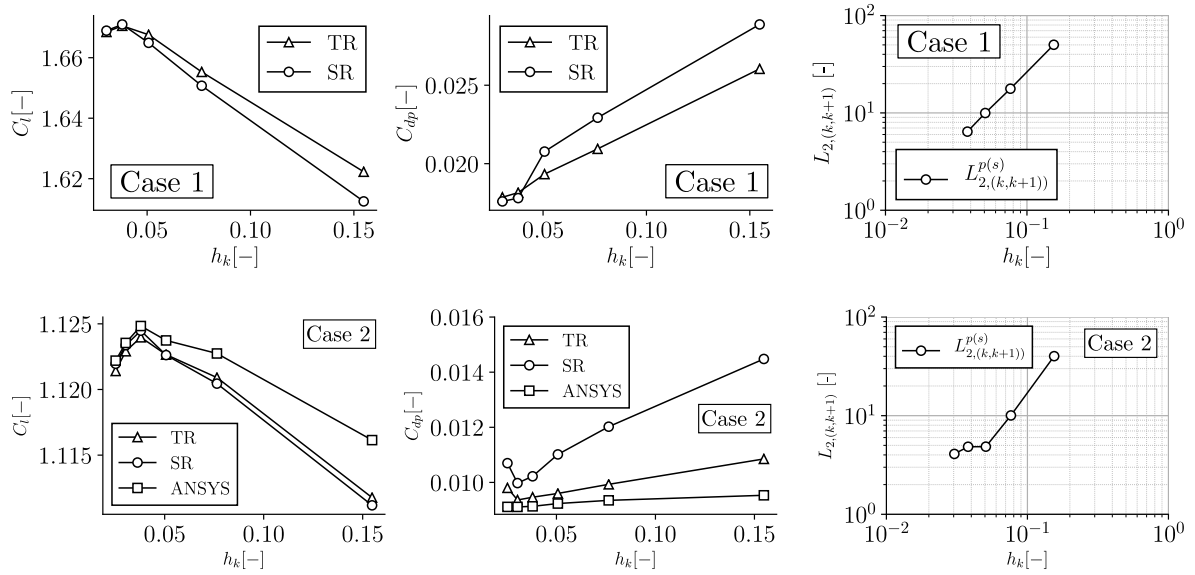

Figure 6.8: Results of the grid refinement study of the two considered cases. The Ansys solutions for Case 2 are obtained via the normal and axial force components (N and A) computed by Ansys Fluent and used for convergence tracking. Equations (3.12) and (3.13) are subsequently used to compute the lift and pressure drag coefficient C_l and C_{dp}.

Table 6.7: Observed rate of convergence $\hat{p}$ and exact solution estimates $\bar{f}$ for the lift coefficient C_l, obtained using the various method of computation.

		Case 2			Case 1	
h	r	C_l^{TR}	C_l^{SR}	C_l^{ANSYS}	C_l^{TR}	C_l^{SR}
0.1548	-	1.112	1.111	1.116	1.622	1.612
0.0764	2.03	1.121	1.120	1.123	1.655	1.651
0.0380	2.01	1.124	1.124	1.125	1.671	1.671
	$\hat{p} \rightarrow$	1.56	1.19	1.64	1.10	0.90
	$\bar{f} \rightarrow$	**1.126**	**1.128**	**1.126**	**1.684**	**1.694**

Table 6.8: Observed rate of convergence $\hat{p}$ and exact solution estimates $\bar{f}$ for the pressure drag coefficient C_{dp}, obtained using the various method of computation.

		Case 2			Case 1	
h	r	C_{dp}^{TR}	C_{dp}^{SR}	C_{dp}^{ANSYS}	C_{dp}^{TR}	C_{dp}^{SR}
0.1548	-	0.0109	0.0145	0.00953	0.0260	0.0289
0.0764	2.03	0.0099	0.0120	0.00934	0.0209	0.0229
0.0380	2.01	0.0095	0.0102	0.00913	0.0182	0.0178
	$\hat{p} \rightarrow$	0.97	0.44	-0.24	0.86	0.21
	$\bar{f} \rightarrow$	**0.009**	**0.005**	**0.011**	**0.015**	**-0.014**

Table 6.8 summarizes the convergence study results for the pressure drag coefficient C_{dp}. The observed orders of convergence range between $-0.24 - 0.97$ for Case 2 and $0.21 - 0.86$ for Case 1. The negative rate of convergence when using the results from ANSYS is due to the larger drop in C_{dp} in the $h_2 \rightarrow h_4$ refinement step than in the $h_1 \rightarrow h_2$ step. It must however be mentioned that the sensitivity of $\hat{p}$ for small changes in the solution data is large such that the variation in $\hat{p}$ can be substantial when errors are made in calculating C_{dp}. As the computation of C_{dp} using surface pressures is prone for large errors (see Appendix B) the found values for $\hat{p}$ and consequently $\bar{f}$ cannot be considered reliable.

In Table 6.9 the observed rate of convergence for the local surface pressures is presented for cases 1 and 2. As for the lift and pressure drag coefficient $\hat{p}$ for Case 2 is higher than for Case 1, possibly due to the larger regions of turbulent flow present in Case 1. The rate of convergence of $L_2^{p(s)}$ coincides better with $\hat{p}$ found using the trapezoidal rule for computing C_l and C_{dp} which might carefully indicate that the trapezoidal rule affects the observed order of accuracy less than the Simpson rule. No further evidence is provided to support is statement however.

Table 6.9: Observed order of accuracies for the relative norm of the surface pressure distribution $L_2^{p(s)}$.

h	r	Case 2 $L_2^{p(s)}$	Case 1 $L_2^{p(s)}$
0.1548	-	40.12	50.15
0.0764	2.03	10.74	25.53
0.0380	2.01	-	-
	$\hat{p} \rightarrow$	1.87	0.96

7 Results comparison and analysis

An overview of the measured data and ANSYS simulation results is made in comparison to predictions by XFOIL and reference data form the TU Delft as laid out in Section 4.1.1. Lift and drag polars in a state of free boundary layer transition are shown in Figure 7.1 while results obtained in "tripped" condition are presented in Figure 7.2.

The lift polar in case of free transition reveals that lift coefficients predicted using ANSYS are slightly lower than those from XFOIL (despite the difference in Re_c in the plots). Both numerical methods tend to over-predict the lift when compared to experiments. Furthermore operation beyond stall is hard/impossible to predict in ANSYS due to the high levels of turbulence involved. The higher C_l obtained at the TU Delft could be accredited to the higher Reynolds numbers compared to the measurements performed in this thesis. Higher Reynolds reduce the boundary layer thickness and the size of laminar separation bubbles which increases the suction side velocity and reduces pressure, thereby increasing lift.

Figure 7.1(r) shows the drag polar in clean state. ANSYS results are omitted in this plot due to the regarded inaccuracy of the results (see Section 6.2.4). The effect of Reynolds number on the boundary layer momentum thickness becomes evident at lower Re_c as increase in drag. Lower Reynolds numbers cause laminar separation bubbles to form causing a profound increase in drag. The rather impressive match between measurements at $\mathrm{Re}_c = 0.87{\times}10^6$ and predictions from XFOIL at the same Reynolds number might be fortuitously. As the standard deviation in wake rake pressures was rather large and the choice of using either the data mean of median as basis (see Section 5.6.3) the spread is significant (see Sections 5.6.1 and 5.6.2).

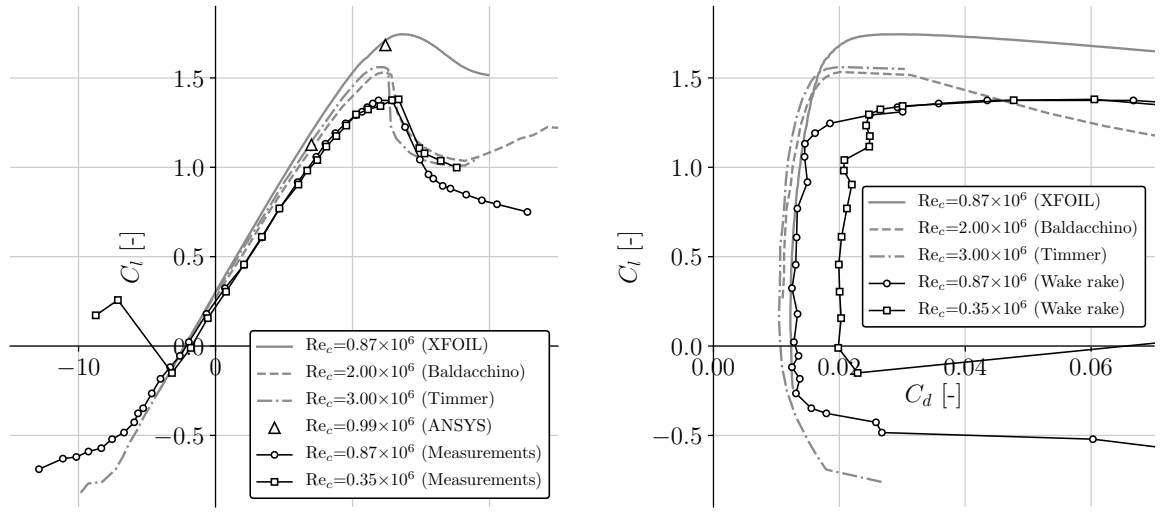

Figure 7.1: Comparison of lift (l) and drag (r) polars, in state of free transition, between measurements and XFOIL at $\mathrm{Re}_c = 0.87{\times}10^6$*, ANSYS at* $\mathrm{Re}_c = 0.99{\times}10^6$ *and reference data from TU Delft by Timmer and van Rooij [60] and Baldacchino et al. [6].*

Under tripped conditions (Figure 7.2) the lift polar shows a reduction in maximum C_l at lower Reynolds numbers as separation of the boundary layer occurs under lower adverse pressure gradients at lower angles of attack. The collapse in lift coefficient becomes less severe as the Reynolds number drops due to the more gradual movement of the separation point from the trailing edge upstream (see Section 5.6.2). Again XFOIL over-predicts the lift coefficient due to reasons discussed above, however the absence of the C_l-collapse is predicted quite well.

Drag in forced transition conditions shows similar trends as under free transition where lower Reynolds numbers yield higher drag coefficients. Again XFOIL predictions match wake rake measurements surprisingly well for low angles of attack which, considering the spread of the data, is again considered fortuitously.

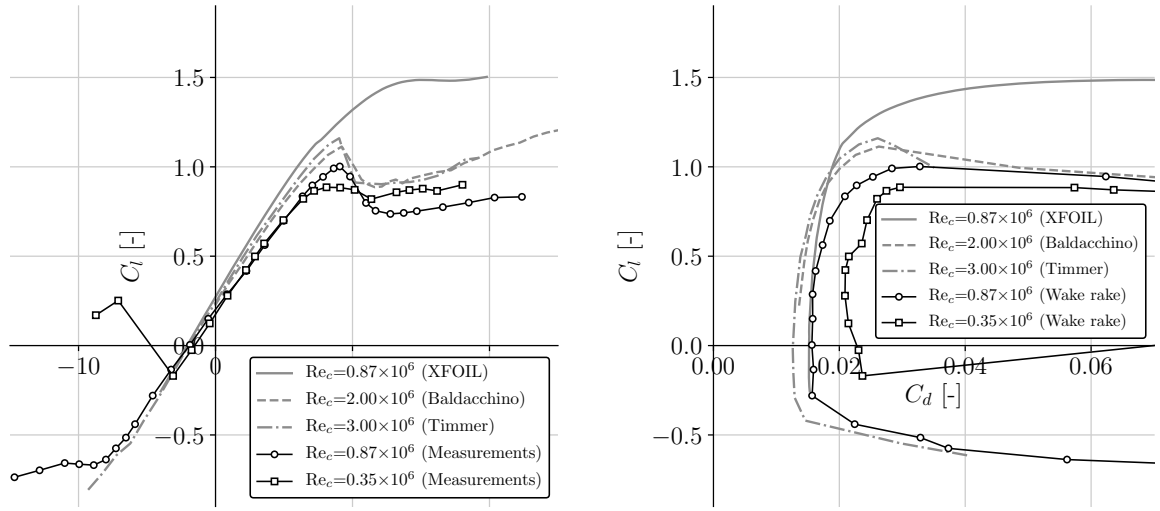

Figure 7.2: Data comparison of lift and drag polars in forced transition conditions.

Surface pressure distributions at $\alpha \approx 7°$ are depicted in Figure 7.3(l) showing both experimental results and predictions from XFOIL and ANSYS. Surface pressures on the suction side again tend to be over-predicted in XFOIL supposedly as a result of its trailing edge treatment (see Section 4.1.1). Also ANSYS shows slight over-prediction of the suction pressures when compared to experimental results albeit the small different in Reynolds number.

At $\alpha \approx 12°$ the over-prediction of suction side pressure by both XFOIL and ANSYS becomes more apparent. The pressure distributions of ANSYS at $\alpha = 12.4°$ and XFOIL at $\alpha = 11.83°$ match surprisingly well which could either be by coincidence or due to boundary effects in the ANSYS simulation. Possibly the induced clockwise circulation by the airfoil deflects the free stream in the computational domain, lowering the effective angle of attack such that is matches with XFOIL. This hypothesis could easily be checked by analysis of the velocity components in the free stream just upstream of the airfoil, however time constrains limited this from doing.

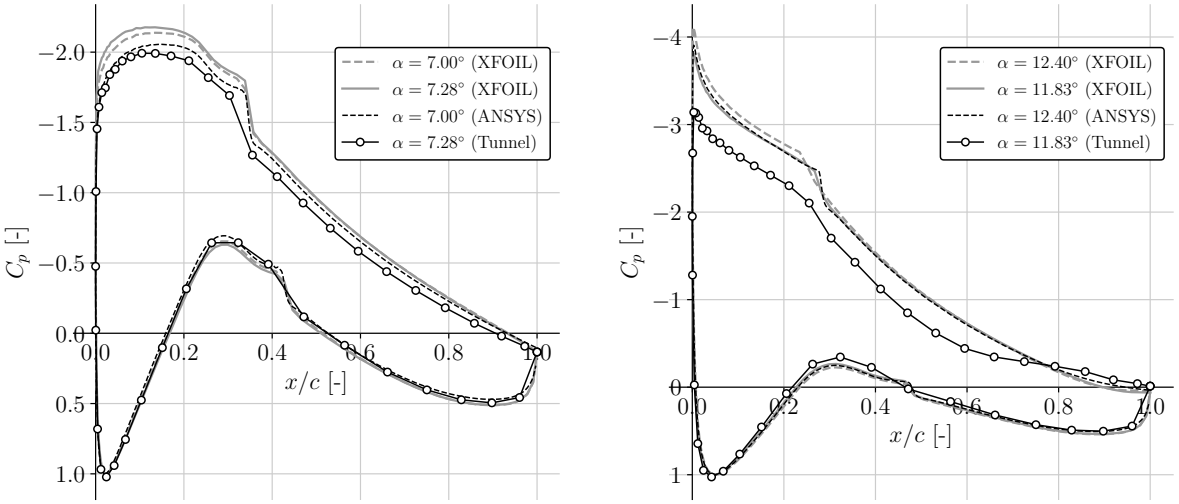

Figure 7.3: Comparison of measured pressure distributions at $\alpha \approx 7°$ (l) and $\alpha \approx 12°$ (r). Reynolds number in case of Tunnel vs. XFOIL equals $\mathrm{Re}_c = 0.87{\times}10^6$ *and for ANSYS vs. XFOIL* $\mathrm{Re}_c = 0.99{\times}10^6$.

8 Conclusions and recommendations

Wind tunnel model design and construction

An airfoil wind tunnel model, manufactured in sections, yields results comparable to those found in literature and provides a good alternative to more expensive manufacturing methods. The total manufacturing costs of the model sections was approximately a factor ten lower compared to models manufactured from a single part[1].

Placement of the pressure taps on the interface between sections proved to be a workable method for realizing a model equipped for measuring surface pressures. Sealing the interface using bees wax in combination with rubber gaskets and vacuum grease created a robust seal that lasted throughout the measurement campaign. Thinner rubber gaskets < 1.0 mm could further smooth transition between both measurement blocks as the aerodynamic effects of interfaces between the blocks is not known yet. As the interfaces between adjacent sections form tiny grooves, effects on (three-dimensional) flow patterns is not excluded. Further research is required to asses the effects on measured pressure distributions and the resulting lift and drag.

The choice for using aluminium combined with CNC machining was based on multiple considerations however the use of additive manufacturing techniques is well worth investigating (see Section 2.1). 3D printing using Digital Light Processing (DLP) has proven to give smooth surface finishes suitable for use with airfoils and allows more freedom in designing surface pressure taps arrangements.

Although precision of the manufactured airfoil sections is expected to be high. Verification of the model contour with respect to the theoretical design using three-dimensional profile measurement equipment is recommended. A possibly deviating contour could then be fed back in XFOIL to re-predict the airfoil performance based on the physical part.

Experimental campaign

The facilities of the Engineering Fluid Dynamics (EFD) group allow measurements of airfoil aerodynamic performance to a seemingly sufficient level of accuracy such that results may be compared to literature. Further assessment of the uncertainty in these experiments is recommended though. A sensor error propagation analysis (see Section 5.6.3) gives insight in the most critical sensors for deducing aerodynamic forces and provides limits of sensor uncertainties required. The book of Lipták [34] contains a thorough discussion on measurements errors and uncertainty calculations and might be consulted for this purpose.

A fixed wake rake, traversed manually in two discrete positions, was used in these experiments. An x, y, z-traverse system, present in within the EFD group, enables (much) higher resolution measurements in the wake, allowing improved drag computations by integration. Furthermore variations in drag measurements over the span-wise direction have been found by other researchers as presented Althaus [4], Mueller and Jansen Jr. [38] and Baldacchino et al. [6]. Performing wake rake measurements at varying locations over the span allows assessment of the three-dimensional character of the flow and enables an average drag coefficient C_d to be established. The wake rake used in this thesis could be adopted for this purpose with the recommendation to add several static pressure taps such that stream velocity at the rake's position is more easily determined.

Next to this the axial force coefficient C_a, computed by numerically integrating the pressure, was used to determine the lift coefficient using Equation (3.12),

$$C_l = C_n \cos\alpha - C_a \sin\alpha \tag{3.12*}$$

The axial force coefficient, predominantly responsible for the drag, is prone to numerical errors (see Appendix B) and does not include shear forces. Although its contribution in (3.12*) is very small, this equation can be improved by utilizing the drag coefficient measured from the wake rake C_d. This value contains both the pressure and shear forces and is not sensitive to numerical errors. We can rewrite (3.12) and (3.13) such that we eliminate C_a yielding:

$$C_l = C_n / \cos\alpha - C_d \tan\alpha \tag{8.1}$$

[1] From oral discussions with dr. L.D. de Santana, Assistant Professor EFD group, UT

This equation is used by Timmer and van Rooij [60] and Baldacchino [6] in the reference measurements at the TU Delft. where C_n is determined from the surface pressures and C_d is computed from i) the wake rake in pre-stall regime and ii) using the pressure distributions in post-stall regime. Reprocessing of the data gathered in this tesis would allow one to compute the lift using this equation.

It is found that numerical integration of the surface pressures with higher order schemes using a modified Simpson rule does not clearly lead to more accurate results (Appendix B). Calculation of the pressure drag from surface pressures leads to significant discrepancies with drag measured by a wake survey (Section 5.6.1) such that this method is discouraged.

The hysteresis effects observed at low Reynolds numbers at negative angles of attack might deserve further research. Although the application of thick airfoils ($> 0.2t/c$) in low Reynolds number flows is limited, the observed phenomena tend to spark the scientific interest.

Lastly integration of experimental work as performed in this thesis in an educational setting such as Bachelors or Masters courses is possible. Preparation time for the experiments is expected to take around a week considering the required data acquisition equipment (Section 5.2) is available and in working order. LabVIEW programs and Python scripts used for post-processing have been included with this thesis[2] and are freely usable.

Numerical work

Results from the grid refinement study reveal that verification of numerical solutions is all but straightforward. Obtaining an approximation of the exact solution with known level of accuracy requires the grid refinement process to obey a range of conditions, some of which are contradictory. The subject of numerical solution verification and validation is heavily studied [17, 42, 50] and becomes increasingly important in engineering and science. As the use of CFD in design processes grows and the complexity of the problems increases a profound understanding of the validity of solutions is required.

Possible improvements concerning the approach taken in this thesis are numerous but some come are directly applicable to the workflow used and have partially been discussed in the corresponding chapter:

- The proper cell height Δy of cells adjacent to the airfoil boundary can more accurately be determined using the iterative process described in Section 6.1.1
- Smoothing of the computational grid is not performed in this thesis as mesh quality decreased substantially. An O-type quadrilateral grid was used in this work which might not be the most suitable grid type for this problem. Proper mesh generation at the trailing edge proved difficult which might have contributed to the poor quality after smoothing (Section 6.1.1).
- Interpolation of surface pressures at locations from the coarse grids onto the finer grids is performed linearly in this thesis which is suspected to influence the solution as linear interpolation is first order accurate. Quadratic interpolation is required to eliminate this influence as the order of accuracy is higher than the numerical scheme used to obtain the solutions. (Section 6.2.2)
- Despite the non-monotonic behaviour of the solutions the method proposed by Eça and Hoekstra [17] could be employed to to obtain a better estimate of the observed convergence rate $\hat{p}$ (Section 6.2.4).

Nevertheless the obtained CFD predictions using the Transition SST turbulence model yield comparable results to XFOIL. As computation time in XFOIL is order of magnitude less than CFD this proves that XFOIL still is a very attractive tool for the prediction of two-dimensional airfoil performance.

[2] Digital version only, and provided separately to the committee prior graduation

References

[1] I. H. Abbott and A. E. von Doenhoff. *Theory of Wing Sections: Including a summary of airfoil data*, page 120. Dover Publications Inc., Dover edition, 1959.

[2] J. Abrahamson. *ANSYS Fluent Theory Guide 2019 R1*, 2019.

[3] C. Aghanajafi, S. Daneshmand, and A. Ahmadi Nadooshan. Influence of Layer Thickness on the Design of Rapid-Prototyped Models. *ARC Journal of Aircraft*, 46(3):981–987, May 2009.

[4] D. Althaus. Drag Measurement on Airfoils. In *XVIIth OSTIV Congress*, page 3, May 1981.

[5] J. Anderson. *Fundamentals of Aerodynamics*. McGraw-Hill Education, 2010.

[6] D. Baldacchino, C. Ferreira, D. De Tavernier, W. Timmer, and G. J. W. van Bussel. Experimental parameter study for passive vortex generators on a 30% thick airfoil: Experimental parametric vortex generator study. *Wind Energy*, 21(9):745–765, September 2018.

[7] J. B. Barlow, W. H. Rae, and A. Pope. *Low-speed wind tunnel testing*. John Wiley & Sons, Ltd., 3rd ed edition, 1999.

[8] A. Björk. Coordinates and calculations for the FFA-W1-xxx, FFA-W2,xxx and FFA-W3-xxx Series of airfoils for horizontal axis wind turbines. Technical Report FFA TN 1990-15, Flygtekniska Försöksanstalten, 1990.

[9] P. Brøndsted and R. P. L. Nijsen. *Advances in wind turbine blade design and materials*. Woodhead Publishing, 2013.

[10] T. F. Brooks, M. A. Marcolini, and D. S. Pope. Airfoil trailing edge flow measurements and comparison with theory, incorporating open wind tunnel corrections. In *AIAA/NASA 9th Aeroacoustics Conference*. American Institute of Aeronautics and Astronautics (AIAA), October 1984.

[11] C. T. Crowe, D. F. Elger, B. C. Wiliams, and J. A. Roberson. *Engineering Fluid Mechanics*. John Wiley & Sons, Ltd., 9$^{\text{th}}$ edition, 2009.

[12] L. D. de Santana, M. P. Sanders, C. H. Venner, and H. W. Hoeijmakers. The UTwente Aeroacoustic Wind Tunnel Upgrade. In *2018 AIAA/CEAS Aeroacoustics Conference*. American Institute of Aeronautics and Astronautics (AIAA), June 2018.

[13] S. Discetti and A. Ianiro. *Experimental aerodynamics*. CRC Press, Taylor & Francis Group, 2017.

[14] A. E. v. Doenhoff and F. T. Abbott. The Langley Two-dimensional Low-turbulence Pressure Tunnel. Technical Report 1283, National Advisory Committee for Aeronautics (NACA), 1947. NACA Technical Note.

[15] M. Drela. XFOIL: An Analysis and Design System for Low Reynolds Number Airfoils. In *Low Reynolds Number Aerodynamics: Proceedings of the Conference Notre Dame*, volume 54, June 1989.

[16] M. Drela. *XFOIL 6.9 User Primer*, 2001.

[17] L. Eça and M. Hoekstra. A procedure for the estimation of the numerical uncertainty of CFD calculations based on grid refinement studies. *Journal of Computational Physics*, 262:104–130, April 2014.

[18] H. W. Emmons. The Laminar-Turbulent Transition in a Boundary Layer-Part I. *Journal of the Aeronautical Sciences*, 18(7):490–498, July 1951.

[19] D. E. Faleiros, M. Tuinstra, and H. W. Hoeijmakers. Drag, Lift and Effective Angle of Attack from the Wake of an Airfoil in the Open-Jet Wind Tunnel. In *54th AIAA Aerospace Sciences Meeting*. American Institute of Aeronautics and Astronautics (AIAA), Januari 2016.

[20] R. Fitzpatrick. *Theoretical Fluid Mechanics*. IOP Publishing, 2017.

[21] P. Fuglsang and C. Bak. Development of the Risø wind turbine airfoils. *Wind Energy*, 7(2):145–162, April 2004.

[22] H. Glauert. Wind Tunnel Interference on Wings, Bodies and Airscrews. Technical Report 1566, Aeronautical Research Committee, 1933. Reports and Memoranda.

[23] F. Hama. An Efficient Tripping Device. *Journal of the Aerospace Sciences*, 24:236–237, 1957.

[24] A. L. Heyes and D. A. Smith. Rapid Technique for Wind-Tunnel Model Manufacture. *ARC Journal of Aircraft*, 41(2):413–415, March 2004.

[25] E. L. Houghton. *Aerodynamics for Engineering Students*. Butterworth-Heinemann, 6th edition, 2012.

[26] B. Jones. The Measurement of Profile Drag by the Pitot-traverse Method. Technical Report 1688, Aeronautical Research Committee, 1936. Reports and Memoranda.

[27] J. Katz and A. Plotkin. *Low-Speed Aerodynamics*, volume 126. Cambridge University Press, 2nd edition, 2004.

[28] R. D. Klafter. On the Numerical Integration of Discontinuous Functions. *IEEE Transactions on Education*, page 3, July 1970.

[29] E. Kroll and D. Artzi. Enhancing aerospace engineering students' learning with 3D printing wind-tunnel models. *Emerald Rapid Prototyping Journal*, 17(5):393–402, August 2011.

[30] M. S. Kuester, A. Borgoltz, and W. J. Devenport. Pressure Tap Effects on the Lift Measurement of an Airfoil Section. In *32nd AIAA Aerodynamic Measurement Technology and Ground Testing Conference*. American Institute of Aeronautics and Astronautics (AIAA), June 2016.

[31] P. K. Kundu, I. M. Cohen, and D. R. Dowling. *Fluid Mechanics*. Academic Press, 5th edition, 2012.

[32] D. B. Landrum, R. M. Beard, P. A. LaSarge, and N. von Sprecken. Evaluation of stereolithography rapid prototyping for low speed airfoil design. In *35th Aerospace Sciences Meeting and Exhibit*. American Institute of Aeronautics and Astronautics (AIAA), Januari 1997.

[33] R. B. Langtry and F. R. Menter. Correlation-Based Transition Modelling for Unstructured Parallelized Computational Fluid Dynamics Codes. *AIAA Journal*, 47(12):2894–2906, December 2009.

[34] B. G. Libták. *Instrument engineers' handbook*. CRC Press, 4th edition, 2003.

[35] D. I. T. P. Llewelyn-Davies. The use of carbon fibre-reinforced plastics in the construction of wings for testing in wind tunnels. *Elsevier Composites*, 7(2):100–106, April 1976.

[36] J. F. Manwell, J. G. McGowan, and A. L. Rogers. *Wind Energy Explained: Theory, Design and Application*. John Wiley & Sons, Ltd., 2009.

[37] M. Miller, K. Lee Slew, and E. Matida. The development of a flatback wind turbine airfoil family. *Wind Energy*, 21(12):1372–1382, December 2018.

[38] T. Mueller and B. Jansen, Jr. Aerodynamic Measurements at Low Reynolds Numbers. In *12th Aerodynamic Testing Conference*. American Institute of Aeronautics and Astronautics (AIAA), March 1982.

[39] NLR - Royal Netherlands Aerospace Center. *Aircraft of the future – researchers conduct first real-time flutter analysis*. Webarticle accessed November 2019.

[40] NLR - Royal Netherlands Aerospace Center. *Smart wind tunnel models: creating a competitive edge*. Webarticle accessed November 2019.

[41] F. Norton. Construction of Models for Tests in Wind Tunnels. Technical Report 74, National Advisory Commity for Aeronautics (NACA), 1920. NACA Technical Report.

[42] W. L. Oberkampf and C. J. Roy. *Verification and validation in scientific computing*. Cambridge University Press, 2010.

[43] A. Picard, R. S. Davis, M. Gläser, and K. Fujii. Revised formula for the density of moist air (CIPM-2007). *Metrologia*, 45(2):149–155, April 2008.

[44] K. Pohlhausen. Zur näherungsweisen Integration der Differentialgleichung der Iaminaren Grenzschicht. *ZAMM - Journal of Applied Mathematics and Mechanics / Zeitschrift für Angewandte Mathematik und Mechanik*, 1(4):252–290, 1921.

[45] G. Ramanujam and H. Özdemir. Improving Airfoil Lift Prediction. In *35th Wind Energy Symposium*. American Institute of Aeronautics and Astronautics (AIAA), Januari 2017.

[46] G. Ramanujam, H. Özdemir, and H. W. Hoeijmakers. Improving Airfoil Drag Prediction. *Journal of Aircraft*, page 13, June 2016.

[47] R. Rayle. An Investigation of the Influence of Orifice Geometry on Static Pressure Measurements. Master's thesis, Massachusetts Institute of Technology (MIT), 1949.

[48] B. C. Reed. Numerically Integrating Irregularly-spaced (x, y) Data. *The Mathematics Enthausiast*, 11(3):7, 2014.

[49] L. Rosenhead. *Laminar Boundary Layers*. Dover Publications, Inc., 1988.

[50] M. D. Salas and H. L. Atkins. On problems associated with grid convergence of functionals. *Computers & Fluids*, 38(7):1445–1454, August 2009.

[51] H. Schlichting. *Boundary-layer Theory*. McGraw-Hill, Inc., 7^{th} edition, 1979.

[52] H. Schlichting and K. Gersten. *Boundary-layer Theory*. Springer-Verlag, 2017.

[53] P. Schubel and R. Crossley. Wind Turbine Blade Design Review. *Wind Engineering*, 36(4):365–388, August 2012.

[54] R. Shaw. The influence of hole dimensions on static pressure measurements. *Journal of Fluid Mechanics*, 7(04):550, April 1960.

[55] S. Shun and N. A. Ahmed. Rapid Prototyping of Aerodynamics Research Models. *Applied Mechanics and Materials*, 217–219:2016–2025, November 2012.

[56] A. M. O. Smith and D. W. Clutter. The Smallest Height of Roughness Capable of Affecting Boundary-Layer Transition. *Journal of the Aerospace Sciences*, 26(4):229–245, April 1959.

[57] A. Springer and K. Cooper. Comparing the aerodynamic characteristics of wind tunnel models produced by rapid prototyping and conventional methods. In *15^{th} Applied Aerodynamics Conference*. American Institute of Aeronautics and Astronautics (AIAA), June 1997.

[58] W. Sutherland. The Viscosity of Gases and Molecular Force. *The London, Edinburgh, and Dublin Philosophical Magazine and Journal of Science*, 36(223):507–531, December 1893.

[59] J. L. Tangler and D. M. Somers. Status of the Special-Purpose Airfoil Families. Technical Report SERI/TP-217-3264, Solar Energy Research Institute (SERI), 1987.

[60] W. A. Timmer and R. P. J. O. M. van Rooij. Summary of the Delft University Wind Turbine Dedicated Airfoils. *ASME Journal of Solar Energy Engineering*, 125(4):488, November 2003.

[61] L. W. Traub. Effect of Rapid-Prototyped Airfoil Finish on Loading at Low Reynolds Numbers. *ARC Journal of Aircraft*, 50(1):307–311, January 2013.

[62] C. Tyler, W. Braisted, and J. Higgins. Evaluation of Rapid Prototyping Technologies for Use in Wind Tunnel Model Fabrication. In *43^{rd} AIAA Aerospace Sciences Meeting and Exhibit*. American Institute of Aeronautics and Astronautics (AIAA), January 2005.

[63] C. van Dam, E. Mayda, D. Chao, K. Jackson, M. Zuteck, and D. Berry. Innovative Structural and Aerodynamic Design Approaches for Large Wind Turbine Blades. In *43^{rd} AIAA Aerospace Sciences Meeting and Exhibit*. American Institute of Aeronautics and Astronautics (AIAA), January 2005.

[64] R. van Rooij and N. Timmer. *Design of Airfoils for Wind Turbine Blades*, May 2004. Presentation.

[65] R. P. J. O. M. van Rooij and W. A. Timmer. Roughness Sensitivity Considerations for Thick Rotor Blade Airfoils. *ASME Journal of Solar Energy Engineering*, 125(4):468–478, November 2003.

[66] N. Verhaagen, H. W. Hoeijmakers, and J. Gijrath. Conversion of the UT wind tunnel to an aeroacoustic test facility. In *37^{th} Joint Propulsion Conference and Exhibit*. American Institute of Aeronautics and Astronautics (AIAA), July 2001.

[67] F. M. White. *Viscous fluid flow*, page 375. McGraw-Hill, Inc., 3^{rd} edition, 2007.

Appendices

A Static pressure taps

To determine the section lift the surface pressure distribution is measured using an array of static pressure taps located around the full perimeter of the wing section. The available pressure scanners limited the amount of taps to $3 \times 16 = 48$ in total[1]. A study is performed to assess the lift predictive accuracy when numerically integrating the pressure distribution over the surface as a function of the tap distributions.

Reference pressure distributions have been obtained using XFOIL 6.99 with a DU97-W-300 airfoil described with a 300 panel distribution composed using the XFOIL routine `PPAR` → `n 300`. Multiple distributions with 48 panels are composed by combining the top and bottom half of two XFOIL panel distributions. Table A.1 gives an overview of the tap distributions and the corresponding XFOIL panel distributions used to create them.

Table A.1: Tap distributions and the XFOIL panel distributions using `PPAR` → `n`.

Case No.	Tap distributions			`PPAR` → `n`	
-	$N_{\text{bottom}}/N_{\text{top}}$	N_{top}	N_{bottom}	Top	Bottom
1	0.50	32	16	66	30
2	0.55	31	17	64	32
3	0.60	30	18	62	34
4	0.66	29	19	60	36
5	0.71	28	20	58	38
6	0.78	27	21	56	40
7	0.85	26	22	54	42
8	0.92	25	23	52	44
9	1.00	24	24	50	46

The C_p values at the tap locations of the 48 panel distributions are obtained by linear interpolation from the 300 panel reference C_p distributions such that for each panel distribution $C_p(x/c)$ is known. The lift coefficient C_l of each panel distribution at a given α is determined by numerically integrating the pressure distribution over the airfoil perimeter. Both a trapezoidal rule and a modified Simpson rule are used to do so. Figures A.1 and A.2 show the results of the lift coefficient prediction using Case 1 and 9 tap distributions with ratios $N_{\text{bot}}/N_{\text{top}} = 0.50$ and 1.0 respectively.

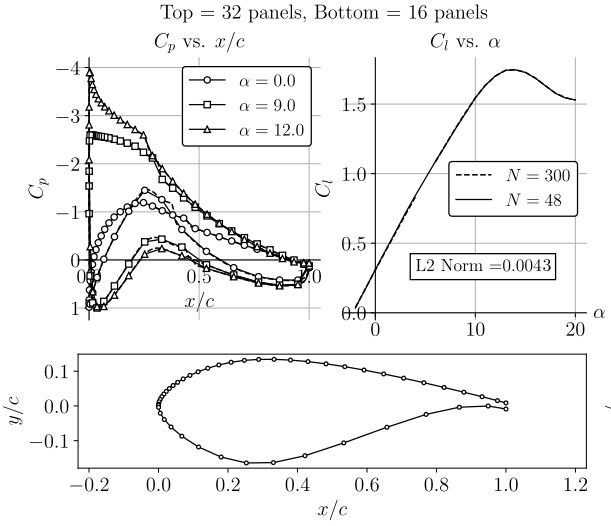

Figure A.1: Panel distribution Case 1

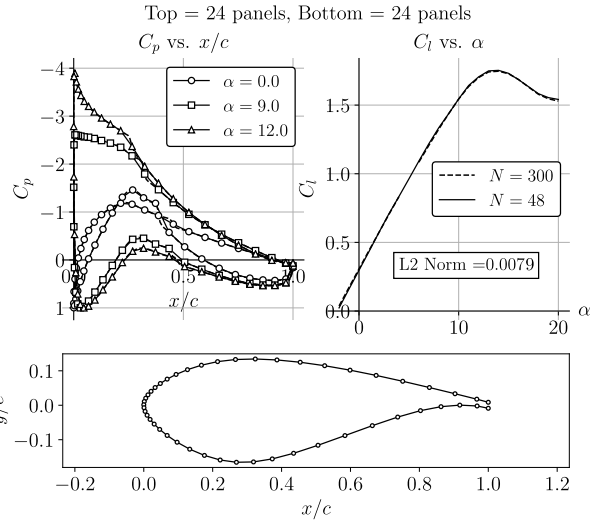

Figure A.2: Panel distribution Case 9

[1] Only three 16-channel pressure scanners where available in the EFD group when designing the model. Currently the group has access to six 16-channel pressure scanners, four with a range of ±1.0 psi and two of ±2.5 psi. This would have allowed more surface pressure taps to be installed in the model.

To evaluate the accuracy of the C_l prediction with 48 panels the L_2 norm is computed for $\alpha \in [-2:20]$

$$L_2 = \sqrt{\frac{1}{N-1}\sum_{\alpha=-2}^{20}\left(C_{l,\alpha,48} - C_{l,\alpha,300}\right)^2} \tag{A.1}$$

The norms of all panel distributions are compared to see there effect on the predictive accuracy of C_l. Figure A.3 shows the L_2 norms of all cases revealing that the difference in accuracy is very limited between the different panel ratios using either the trapezoidal rule or the modified Simpson rule.

Multiple arguments for a proper pressure tap distribution exist:

- The used distribution should result in an accurate determination of C_l for a given integration scheme. Depending on the pressure distribution a Simpson scheme might not be more accurate than a trapezoidal rule based scheme.
- A denser distribution on the top side increases the measurement resolution and hence provides a "better view" on flow phenomena such as separation and laminar to turbulent transition. Furthermore the size of laminar separation bubbles is better observed using a denser distribution.
- The chosen pressure tap distribution must physically fit in the wind tunnel model. Smaller models offer less space for fitting the required tubing and tubulations dictating a coarser tap distribution.

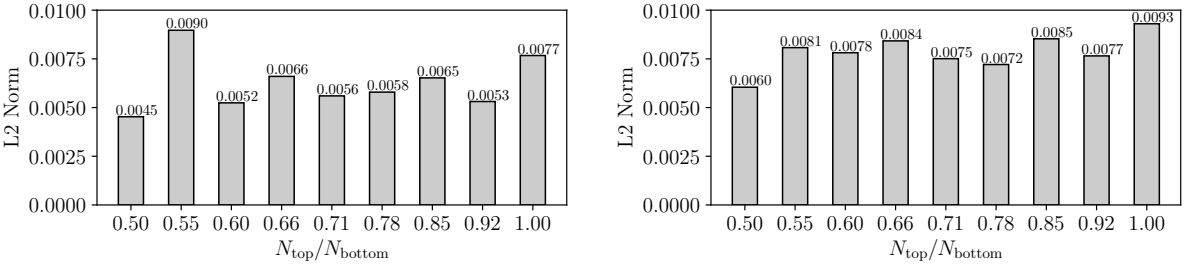

Figure A.3: L2 norms of different panel ratios: (l) C_l computation using a trapezoidal rule. (r) C_l via the modified Simpsons rule (see Appendix B).

Considering these three arguments a panel ratio of 0.71, with 28 panels on top and 20 at the bottom, is chosen for use in the wind tunnel model. This ratio provides good numerical accuracy (compared to the other analysed options), has a higher measurement resolution at the top side and fits physically in the wind model. Figure A.4 shows the location and numbering of the pressure taps in the physical model and Table A.2 gives the tap x, y coordinates together with the arc length parameter Δs

A.1 Pressure tap coordinates

Figure A.4 and Table A.2 show the pressure tap coordinates obtained using the method described above. These coordinates have been used for calculating the lift and pressure drag coefficients from experimental data as described in Appendix B.

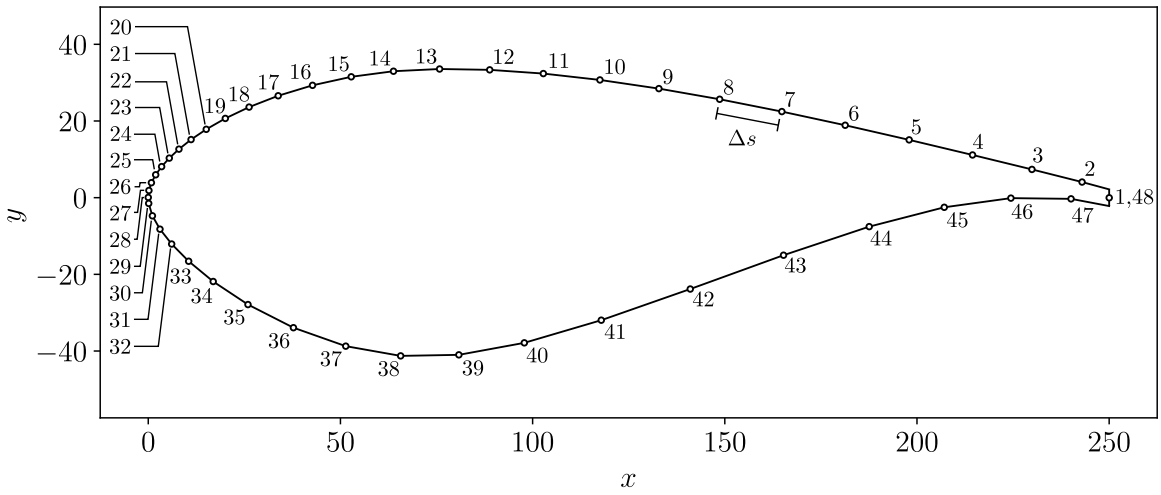

Figure A.4: Locations of static pressure taps around the airfoil perimeter

Table A.2: Spatial locations of pressure taps on the DU97-W-300 wind tunnel model

Tap No.	x [mm]	y [mm]	Δs [mm]	Tap No.	x [mm]	y [mm]	Δs [mm]
1	250.0	0.0 (2.2)	0.0	25	1.9	6.0	2.6
2	243.0	4.1	7.3	26	0.8	3.9	2.4
3	229.9	7.4	13.5	27	0.2	1.9	2.1
4	214.5	11.1	15.9	28	0.0	0.1	1.8
5	198.0	15.1	16.9	29	0.1	-1.5	1.6
6	181.3	18.9	17.1	30	1.1	-4.7	3.4
7	164.8	22.5	16.9	31	3.0	-8.2	4.0
8	148.7	25.7	16.5	32	6.1	-12.1	4.9
9	132.9	28.4	16.1	33	10.5	-16.6	6.3
10	117.5	30.7	15.5	34	16.9	-21.9	8.3
11	102.8	32.4	14.8	35	25.9	-27.9	10.9
12	88.8	33.3	14.0	36	37.8	-33.9	13.3
13	75.8	33.6	13.0	37	51.4	-38.7	14.4
14	63.8	33.0	12.0	38	65.7	-41.3	14.5
15	52.8	31.5	11.1	39	80.8	-41.0	15.1
16	42.7	29.3	10.3	40	97.8	-37.9	17.3
17	33.8	26.6	9.3	41	117.9	-32.0	20.9
18	26.2	23.6	8.1	42	141.0	-23.8	24.5
19	20.0	20.7	6.9	43	165.3	-15.0	25.8
20	15.1	17.8	5.7	44	187.6	-7.6	23.5
21	11.1	15.2	4.8	45	207.1	-2.5	20.2
22	8.0	12.7	4.0	46	224.4	-0.1	17.5
23	5.5	10.3	3.4	47	240.1	-0.3	15.7
24	3.5	8.1	3.0	48	250.0	0.0 (-2.2)	10.1

B Lift, drag and moment coefficients by numerical integration

B.1 Mathematical procedure

Calculation of the section lift and pressure drag is done by numerically integrating the measured surface pressures on the airfoil perimeter as briefly explained in Section 3.2.3. To this end the normal and axial components of the resultant force, N and A respectively, are determined using Equations (3.19) and (3.20) repeated here for convenience.

$$N_{(p)} = \int_{\text{top}} (-p\cos\theta)\, ds + \int_{\text{bot}} (p\cos\theta)\, ds \tag{3.19}$$

$$A_{(p)} = \int_{\text{top}} (-p\sin\theta)\, ds + \int_{\text{bot}} (p\sin\theta)\, ds \tag{3.20}$$

Where θ is the surface angle with respect to the chord line defined positive in clockwise direction.

In case the pressures are measured at discrete locations a numerical approximation of the integrals defining $N_{(p)}$ and $A_{(p)}$ is made. To this end the discrete pressures p_i are decomposed in their normal and axial components, p_i^n and p_i^a respectively and the surface coordinates s_i are computed. This allows the expressions for the normal and axial force to be written in terms of the normal and axial pressure components:

$$N_{(p)} = \int p^n ds, \quad \text{and} \quad A_{(p)} = \int p^a ds \tag{B.1}$$

As mentioned in Section 3.2.3 the surface coordinates s_i run from the trailing edge over the leading edge down to the trailing edge such that $s_0 = s_{N-1}$ corresponds to the trailing edge top and s_{LE} matches the leading edge as shown in Figure B.1. The pressure components are computed first

$$\begin{aligned} p_i^n &= -p_i\cos\bar{\theta}_i \\ p_i^a &= -p_i\sin\bar{\theta}_i \end{aligned} \quad \text{for } i \in [0, \text{LE}) \qquad \begin{aligned} p_i^n &= p_i\cos\bar{\theta}_i \\ p_i^a &= p_i\sin\bar{\theta}_i \end{aligned} \quad \text{for } i \in [\text{LE}, N) \tag{B.2}$$

Where $\bar{\theta}_i$ is the angle of the pressure vector normal to the surface defined positive in clockwise direction with respect to the chord line. $\bar{\theta}_i$ is computed as the mean angle of the two adjacent unit surface patches θ_{i-1} and θ_i respectively. Where,

$$\theta_i = \begin{cases} -\arctan\left(\dfrac{y_i - y_{i-1}}{x_i - x_{i-1}}\right) & (x_i - x_{i-1}) > 0 \\ -\pi/2 & (x_i - x_{i-1}) < 0 \text{ and } (y_i - y_{i-1}) > 0 \\ \pi/2 & (x_i - x_{i-1}) < 0 \text{ and } (y_i - y_{i-1}) < 0 \end{cases} \tag{B.3}$$

and $\bar{\theta}_i$ is computed as,

$$\bar{\theta}_i = \text{mean}(\theta_i, \theta_{i+1}) = \text{arctan2}\left(\frac{1}{2}\sum_{j=i}^{i+1}\sin\theta_j, \frac{1}{2}\sum_{j=i}^{i+1}\cos\theta_j\right) \quad \text{for } i \in (0, N-2) \tag{B.4}$$

The angles of the pressure vectors at the trailing edge ($i = 0$ and $i = N-2$) require special treatment due to the discontinuity in the surface curvature of the blunt trailing edge. Effectively the top and bottom pressure at the trailing edge have two distinct direction vectors as shown in Figure B.1. The angles $\bar{\theta}_0$ and $\bar{\theta}_{N-2}$ are therefore computed as follows:

$$\bar{\theta}_0 = -\arctan\left(\frac{y_1 - y_0}{x_1 - x_0}\right) \tag{B.5}$$

$$\bar{\theta}_{N-2} = -\arctan\left(\frac{y_{N-2} - y_{N-3}}{x_{N-2} - x_{N-3}}\right) \tag{B.6}$$

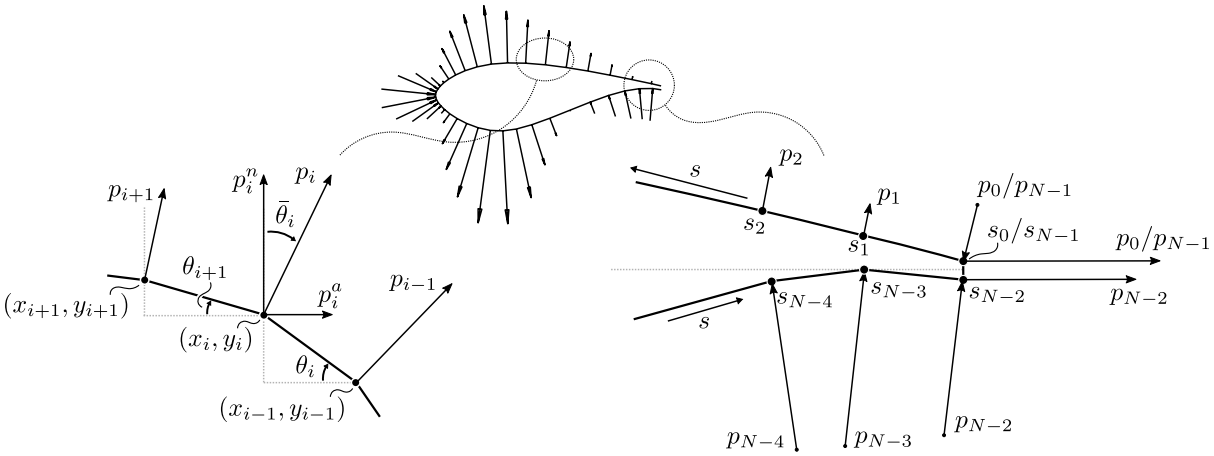

Figure B.1: (l) $\bar{\theta}_i$ computed as $\text{mean}(\theta_i, \theta_{i+1})$ *and $\bar{\theta}$ at the trailing edges. (r) Treatment of direction vectors at the trailing edge where a discontinuity in the surface curvature is present.*

The incremental surface patches s_i are then computed,

$$ds_i = \sqrt{(x_i - x_{i-1})^2 + (y_i - y_{i-1})^2} \quad \text{for } i \in (0, N) \tag{B.7}$$

such that the surface coordinates $s_i = s_{i-1} + ds_i$ of each discrete normal and axial pressure component, p_i^n and p_i^a, are known. This allows the integrals of (B.1) to be approximated numerically using any quadrature rule. The 2$^{\text{nd}}$ order accurate *trapezoidal rule* is arguably the most used method for numerical integration. A theoretically better alternative is the *Simpson rule* which is 4$^{\text{th}}$ order accurate. To approximate an integral $\int p(s)ds$ on the surface grid s composed of N discrete points (including the trailing edge) using a trapezoidal rule the following approximations are made:

$$\begin{aligned} N_{(p)} &= \int p^n ds \approx \sum_{i=1}^{N-2} \bar{p}_i^n ds_i + \bar{p}_{\text{TE}}^n ds_{\text{TE}} \\ A_{(p)} &= \int p^a ds \approx \sum_{i=1}^{N-2} \bar{p}_i^a ds_i + \bar{p}_{\text{TE}}^a ds_{\text{TE}} \end{aligned} \quad \text{where} \quad \begin{cases} \bar{p}_i^n = \frac{1}{2}\left(p_i^n + p_{i-1}^n\right) \\ \bar{p}_i^a = \frac{1}{2}\left(p_i^a + p_{i-1}^a\right) \\ ds_i = s_i - s_{i-1} \end{cases} \tag{B.8}$$

The term $\bar{p}_{\text{TE}} ds_{\text{TE}}$ represents the contribution of pressure acting on the trailing edge to the integral where,

$$\begin{aligned} \bar{p}_{\text{TE}}^n &= \frac{1}{2}(p_{N-1} + p_{N-2})\cos(\theta_{N-1}) = 0 \\ \bar{p}_{\text{TE}}^a &= \frac{1}{2}(p_{N-1} + p_{N-2})\sin(\theta_{N-1}) = -\frac{1}{2}(p_{N-1} + p_{N-2}) \end{aligned} \quad \text{as } \theta_{N-1} = -\pi/2 \tag{B.9}$$

and

$$ds_{\text{TE}} = s_{N-1} - s_{N-2} = \sqrt{(x_{N-2} - x_{N-1})^2 + (y_{N-2} - y_{N-1})^2} \tag{B.10}$$

After computing the normal an axial force on the airfoil, $N_{(p)}$ and $A_{(p)}$ respectively they are converted to dimensionless coefficients C_n and C_a. Calculation of the lift and drag coefficient is done by means of Equations (3.12) and (3.13) where the geometric (tunnel) angle of attack α_t is taken as α

$$\begin{aligned} C_{lt} &= C_n \cos\alpha_t - C_a \sin\alpha_t \\ C_{dpt} &= C_n \sin\alpha_t + C_a \cos\alpha_t \end{aligned} \quad \text{where} \quad \begin{cases} C_n = N_{(p)}/q_0 c \\ C_a = A_{(p)}/q_0 c \end{cases} \tag{B.11}$$

Where again the dynamic pressure q_0 is measured from the pitot-static tube.

If however a Simpson rule is used to approximate the integrals the terms $\bar{p}_i$ and $d\bar{s}_i$ are computed differently. As the surface coordinates s_i are unevenly spaced the standard Simpson rule formulation doesn't hold as it's derivation assumes an equal distribution of points in the abscissa coordinate x, or in this case s. A recent publication by Reed et al.[48] presents a method to circumvent this problem. The technique is, similar to Simpson's rule, based on fitting parabola's through three consecutive data points over which a sub-integral is computed. Summation of all sub-integrals yields the total integral over the

domain of interest. Mathematically the method is written as:

$$N_{(p)} = \sum_{i=2}^{N-2} \left[\int_{s_{i-2}}^{s_i} p^n \, ds \right] ds_i \approx \sum_{i=2}^{N-2} \left[\frac{P^n}{3}(s_i^3 - s_{i-2}^3) + \frac{Q^n}{2}(s_i^2 - s_{i-2}^2) + R^n(s_i - s_{i-2}) \right] ds_i \tag{B.12}$$

$$A_{(p)} = \sum_{i=2}^{N-2} \left[\int_{s_{i-2}}^{s_i} p^a \, ds \right] ds_i \approx \sum_{i=2}^{N-2} \left[\frac{P^a}{3}(s_i^3 - s_{i-2}^3) + \frac{Q^a}{2}(s_i^2 - s_{i-2}^2) + R^a(s_i - s_{i-2}) \right] ds_i \tag{B.13}$$

For $i = 2, 4, 6...N$. Where the coefficients $P^n, Q^n, R^n, P^a, Q^a, R^a$ are found by solving the following linear systems:

$$\begin{pmatrix} s_{i-2}^2 & s_{i-2} & 1 \\ s_{i-1}^2 & s_{i-1} & 1 \\ s_i^2 & s_i & 1 \end{pmatrix} \begin{pmatrix} P^n \\ Q^n \\ R^n \end{pmatrix} = \begin{pmatrix} p_{i-2}^n \\ p_{i-1}^n \\ p_i^n \end{pmatrix} \quad \text{and} \quad \begin{pmatrix} s_{i-2}^2 & s_{i-2} & 1 \\ s_{i-1}^2 & s_{i-1} & 1 \\ s_i^2 & s_i & 1 \end{pmatrix} \begin{pmatrix} P^a \\ Q^a \\ R^a \end{pmatrix} = \begin{pmatrix} p_{i-2}^a \\ p_{i-1}^a \\ p_i^a \end{pmatrix} \tag{B.14}$$

In case $N - 1$ is even, only a single cell remains as $i = N - 2$. The following sub-integrals are then computed and added to the already calculated sum.

$$\int_{s_{N-3}}^{s_{N-2}} p^n \, ds \approx \frac{P^n}{3}(s_{N-2}^3 - s_{N-3}^3) + \frac{Q^n}{2}(s_{N-2}^2 - s_{N-3}^2) + R^n(s_{N-2} - s_{N-3}) \tag{B.15}$$

$$\int_{s_{N-3}}^{s_{N-2}} p^a \, ds \approx \frac{P^a}{3}(s_{N-2}^3 - s_{N-3}^3) + \frac{Q^a}{2}(s_{N-2}^2 - s_{N-3}^2) + R^a(s_{N-2} - s_{N-3}) \tag{B.16}$$

Where the coefficients $P^n, Q^n, R^n, P^a, Q^a, R^a$ are determined by solving:

$$\begin{pmatrix} s_{N-4}^2 & s_{N-4} & 1 \\ s_{N-3}^2 & s_{N-3} & 1 \\ s_{N-2}^2 & s_{N-2} & 1 \end{pmatrix} \begin{pmatrix} P^n \\ Q^n \\ R^n \end{pmatrix} = \begin{pmatrix} p_{N-4}^n \\ p_{N-3}^n \\ p_{N-2}^n \end{pmatrix} \quad \text{and} \quad \begin{pmatrix} s_{N-4}^2 & s_{N-4} & 1 \\ s_{N-3}^2 & s_{N-3} & 1 \\ s_{N-2}^2 & s_{N-2} & 1 \end{pmatrix} \begin{pmatrix} P^a \\ Q^a \\ R^a \end{pmatrix} = \begin{pmatrix} p_{N-4}^a \\ p_{N-3}^a \\ p_{N-2}^a \end{pmatrix} \tag{B.17}$$

The trailing edge component of the pressure distribution is, similar as for the trapezoidal rule, added separately to the summation approximating the integral expressions for $N_{(p)}$ and $A_{(p)}$. This component can, in case of experimental data or pressure distributions from XFOIL, only be approximated using a trapezoidal rule as only one or two pressure components are known. After adding the trailing edge component the normal and axial forces are known and the lift and drag coefficients can be computed using the equations from (B.11).

B.1.1 Moment coefficient

As explained in Section 3.2.3 the moment coefficient around the leading edge is computed via Equation (3.21) repeated here for convenience.

$$M_{\mathrm{LE}(p)} = \int_{\mathrm{top}} [(p\cos\theta)x - (p\sin\theta)y] \, ds + \int_{\mathrm{bot}} [(-p\cos\theta)x + (p\sin\theta)y] \, ds \tag{3.21}$$

In a similar way as for the normal and axial loads this equation can be written in terms of normal an axial pressure components p^n and p^a as:

$$M_{\mathrm{LE}(p)} = -\int p^n x ds + \int p^a y ds \tag{B.18}$$

In which off course both p^n, p^n, x and y are dependent on location s. Also a clockwise moment around the leading edge is considered positive by convention as they tend to increase the angle of attack α. Writing this equation in a descrete form is done similarly as for the lift and drag using Equations (B.2) till (B.7) after which the following discrete relation is found using a trapezoidal rule scheme.

$$M_{\mathrm{LE}}(p) \approx -\sum_{i-1}^{N-2} \bar{p}_i^n ds_i \bar{x}_i + \sum_{i-1}^{N-2} \bar{p}_i^a ds_i \bar{y}_i \tag{B.19}$$

Where the terms $\bar{p}_i^n, \bar{p}_i^a$ and ds_i are as in Equation (B.8). The distance terms $\bar{x}_i$ and $\bar{y}_i$ at which the surface pressure acts with respect to the leading edge are taken as the mean between indices $i-1$ and i such that,

$$\bar{x}_i = \frac{1}{2}(x_{i-1} + x_i) \quad \text{and} \quad \bar{y}_i = \frac{1}{2}(y_{i-1} + y_i), \tag{B.20}$$

The moment around the quarter chord point, $M_{c/4}$ is now computed via Equation (3.22) repeated here for convenience:

$$M_{\mathrm{LE}} = M_{c/4} - \frac{c}{4}L \tag{3.22}$$

B.2 Code verification

As lift and pressure drag are computed as the integral of the pressure distribution over the airfoil surface a verification of the algorithms is required to assure correct approximations. Three (one-dimensional) numerical integration scheme's are verified for correct implementation: *i*) *Trapezoidal rule*. *ii*) *Simpson's rule* and *iii*) *Simpson's rule for unevenly spaced data*.

Mapping of the airfoil coordinates (x, y) to surface coordinates s, as explained in Section B.1 is coded as a subroutine in Python. Prior applying any chosen quadrature rule for approximating the integrals Equations (3.19) and (3.20) this routine, as shown in Listing B.1, is called upon.

Listing B.1: Mapping of surface coordinates

```
def mapping(x,y,p):
        # --- Initializing and pre-alocation ---
        N = len(p) # Number of pressure components
        pn = np.zeros(N) # Pressure components normal direction
        pa = np.zeros(N) # Pressure components axial direction
        s = np.zeros(N) # Surface length coordinates
        ind = list(x).index(min(x)) # Index of leading edge node (x_min)
        # --- Computing normal and axial pressure components ---
        for i in range(N):
                if i == 0: # First trailing edge component
                        pn[i] = - p[i] * np.cos(thetacalc(x[0],x[1],y[0],y[1])) # TE 1st point
                        pa[i] = - p[i] * np.sin(thetacalc(x[0],x[1],y[0],y[1]))
                if i == N-2:# 2nd to last trailing edge component
                        s[i] = s[i-1] + np.sqrt((x[i]-x[i-1])**2+(y[i]-y[i-1])**2)
                        pn[-2] = p[-2] * np.cos(thetacalc(x[-3],x[-2],y[-3],y[-2]))
                        pa[-2] = p[-2] * np.sin(thetacalc(x[-3],x[-2],y[-3],y[-2]))
                if i == N-1: # Last trailing edge component
                        s[i] = s[i-1] + np.sqrt((x[i]-x[i-1])**2+(y[i]-y[i-1])**2)
                        if i > 0 and i < N-2: # All other components
                s[i] = s[i-1] + np.sqrt((x[i]-x[i-1])**2+(y[i]-y[i-1])**2)
                        theta1 = thetacalc(x[i-1],x[i],y[i-1],y[i])
                        theta2 = thetacalc(x[i],x[i+1],y[i],y[i+1])
                        theta_bar = anglemean([theta1,theta2])
                        if i<ind: # Top side
                                pn[i] = -p[i] * np.cos(theta_bar)
                                pa[i] = -p[i] * np.sin(theta_bar)
                        else: # Bottom side
                                pn[i] = p[i] * np.cos(theta_bar)
                                pa[i] = p[i] * np.sin(theta_bar)
        return s,pn,pa
```

Where the routines `thetacalc` and `anglemean` are defined in Equations (B.3) and (B.4) respectively and are coded in Python as shown in Listings B.2 and B.3.

Listing B.2: Mapping of surface coordinates

```
def thetacalc(x1,x2,y1,y2): # Compute surface angle theta CW with respect to the chord line
        if np.abs(x2-x1) < 1e-15 and y2-y1 > 0:
                theta = -np.pi/2
        if np.abs(x2-x1) < 1e-15 and y2-y1 < 0:
                theta = np.pi/2
        if np.abs(x2-x1) > 1e-15:
                theta = -np.arctan((y2-y1)/(x2-x1))
        return theta
```

Listing B.3: Mapping of surface coordinates

```
def anglemean(thetas): # Computing mean angle of list of angles in radians
        N = len(thetas) # Amount of angles
        theta_bar =  np.arctan2([(1/N)*np.sum(np.sin(thetas))],[(1/N)*np.sum(np.cos(thetas))])
        return theta_bar
```

Trapezoidal rule

Integration using the trapezoidal rule, described in Section B.1, is coded in Python using a subroutine requiring the pressure tap coordinates x, y, measured/computed surface pressures p, free stream conditions ρ and U_∞ and angle of attack α as shown in Listing B.4:

Listing B.4: Integration via trapezoidal rule

```
def ClCd_calc_TR(x,y,p,U,rho,alfa):
        # --- Initializing and pre-alocation ---
        N = len(p)
        alf = alfa*np.pi/180
        dn = np.array([])
        da = np.array([])
        # --- Mapping of airfoil surface to straight section ---
        s,pn,pa = mapping(x,y,p)
        # --- Computing normal and axial force components on surface excl. trailing edge ---
        for i in range(1,N-1):
                ds = s[i]-s[i-1]
                dn = np.append(dn,[(ds/2)*(pn[i-1]+pn[i])])
                da = np.append(da,[(ds/2)*(pa[i-1]+pa[i])])
        # --- Adding trailing edge components ---
        ds = s[-1] - s[-2]
        theta = thetacalc(x[-2],x[-1],y[-1],y[-2])
        dn = np.append(dn,[ds*np.mean([p[-1],p[-2]])*np.cos(theta)])
        da = np.append(da,[ds*np.mean([p[-1],p[-2]])*np.sin(theta)])
        # --- Computing force coefficients ---
        Cn = (sum(dn)/(0.25*0.5*rho*U**2)) # Assuming 0.25m chord length
        Ca = (sum(da)/(0.25*0.5*rho*U**2))
        Cl = Cn * np.cos(alf) - Ca * np.sin(alf)
        Cdp = Cn * np.sin(alf) + Ca * np.cos(alf)
        return [Cl,Cdp]
```

Simpson rule for unevenly spaced data

The Python subroutine for Simpson's rule in case of unevenly spaced data is given in Listing B.5.

Listing B.5: Integration via Simpson's rule with unevenly spaced data

```
def ClCd_calc_SRu(x,y,p,U,rho,alfa):
        # --- Initializing and pre-alocation ---
        N = len(p)
        alf = alfa*np.pi/180
        dn = np.array([])
        da = np.array([])
        # --- Mapping of airfoil surface to straight section
        s,pn,pa = mapping(x,y,p)
        # --- Computing sub-integrals ---
        for i in range(2,N-1,2):
                A = np.array([[s[i-2]**2,s[i-2],1] , [s[i-1]**2,s[i-1],1] , [s[i]**2,s[i],1]])
                bn = np.array([pn[i-2],pn[i-1],pn[i]])
                ba = np.array([pa[i-2],pa[i-1],pa[i]])
                # -- Solving linear systems --
                [Pn,Qn,Rn] = np.linalg.solve(A,bn), [Pa,Qa,Ra] = np.linalg.solve(A,ba)
                # -- Computing normal and axial force increments --
                dn = np.append(dn,[(Pn/3)*(s[i]**3-s[i-2]**3) + (Qn/2)*(s[i]**2-s[i-2]**2)\
                + Rn*(s[i]-s[i-2])])
                da = np.append(da,[(Pa/3)*(s[i]**3-s[i-2]**3) + (Qa/2)*(s[i]**2-s[i-2]**2)\
                + Ra*(s[i]-s[i-2])])
        # --- Computing last seqment (excl. TE) in case of (N-1) is even ---
        if (N-1)%2 == 0:
                A = np.array([[s[-4]**2,s[-4],1] , [s[-3]**2,s[-3],1] , [s[-2]**2,s[-2],1]])
                bn = np.array([pn[-4],pn[-3],pn[-2]])
                ba = np.array([pa[-4],pa[-3],pa[-2]])
                # -- Solving linear systems --
                [Pn,Qn,Rn] = np.linalg.solve(A,bn), [Pa,Qa,Ra] = np.linalg.solve(A,ba)
                # -- Computing normal and axial force increments --
                dn = np.append(dn,[(Pn/3)*(s[-2]**3-s[-3]**3) + (Qn/2)*(s[-2]**2-s[-3]**2)\
                + Rn*(s[-2]-s[-3])])
                da = np.append(da,[(Pa/3)*(s[-2]**3-s[-3]**3) + (Qa/2)*(s[-2]**2-s[-3]**2)\
                + Ra*(s[-2]-s[-3])])
        # --- Adding trailing edge components ---
        ds = s[-1] - s[-2]
        theta = thetacalc(x[-2],x[-1],y[-1],y[-2])
        dn = np.append(dn,[ds*np.mean([p[-1],p[-2]])*np.cos(theta)])
        da = np.append(da,[ds*np.mean([p[-1],p[-2]])*np.sin(theta)])
        # --- Computing force coefficients ---
        Cn = sum(dn)/(0.25*0.5*rho*U**2)
        Ca = sum(da)/(0.25*0.5*rho*U**2)
        Cl = Cn * np.cos(alf) - Ca * np.sin(alf)
        Cdp = Cn * np.sin(alf) + Ca * np.cos(alf)
        return [Cl,Cdp]
```

Order of accuracy analysis

In order to determine whether the coded algorithms deliver the expected order of accuracy The following lift integral L of a hypothetical pressure distribution $p(s) = \cos(s)$ is integrated numerically[1]:

$$L = \int_0^{3\pi/2} \cos(s)\, ds = -1 \quad \text{where} \quad \begin{cases} s = \sqrt{x^2 + y^2} \\ x \in [0, 3\pi/2] \\ y = 0 \end{cases} \tag{B.21}$$

The domain $x \in [0, 3\pi/2]$ is divided in $N-1$ cells of varying size according to the following power law:

$$x_i = x_0 + \left(\frac{i}{N-1}\right)^{3/2} (x_{N-1} - x_0) \quad \text{for} \quad \begin{cases} x_0 = 0 \\ x_{N-1} = 3\pi/2 \\ i \in [0...N-1] \end{cases} \tag{B.22}$$

Which assures an uneven distribution of nodes x_i between x_0 and x_{N-1}. To quantify the grid size the parameter h is defined as:

$$h = \frac{x_{N-1} - x_0}{N-1} \tag{B.23}$$

The function $p(s) = \cos(s)$ is numerically integrated on a domain with varying grid densities. The numerical error is calculated as

$$\varepsilon^* = L^* - L \tag{B.24}$$

Where the asterix $(*)$ represents the quadrature rule used with TR for **t**rapezoidal **r**ule, SR for the classical **S**impson **r**ule and SRu for the **u**evenly spaced **S**impson **r**ule. The *rate of convergence* $\hat{p}$ is determined as given by Equation (6.8) and can be written as follows:

$$\hat{p} = \frac{\ln\left[\left(L^*_{k-1} - L\right) / \left(L^*_k - L\right)\right]}{\ln(r_{k-1,k})} = \frac{\ln\left(\varepsilon_{k-1}/\varepsilon_k\right)}{\ln\left(h_{k-1}/h_k\right)} \tag{B.25}$$

When plotting the error ε as a function of the grid size parameter h_k on a logarithmic scale the slope of the line (rate of convergence $\hat{p}$) indicates the order of accuracy as presented in Figure B.2. Table B.1 summarizes the errors ε and the observed rate of convergence $\hat{p}$ for different grid sizes and quadrature rules.

Table B.1: Errors ε and observed order of convergence $\hat{p}$ of the various numerical integration schemes.

Even distribution ($\Delta s = C$)						
h_k	$\varepsilon_k^{\mathrm{TR}}$	$\varepsilon_k^{\mathrm{SR}}$	$\varepsilon_k^{\mathrm{SRu}}$	$\hat{p}_k^{\mathrm{TR}}$	$\hat{p}_k^{\mathrm{SR}}$	$\hat{p}_k^{\mathrm{SRu}}$
0.2244	4.63×10^{3}	1.72×10^{5}	1.72×10^{5}	2.05	4.10	4.10
0.0467	1.85×10^{4}	2.74×10^{8}	2.74×10^{8}	2.01	4.02	4.02
0.0118	1.16×10^{5}	1.07×10^{10}	1.07×10^{10}	2.00	4.01	4.01
0.0029	7.23×10^{7}	4.18×10^{13}	4.17×10^{13}	2.00	4.15	3.94
0.0007	4.52×10^{8}	1.33×10^{15}	1.78×10^{15}	-	-	-
Uneven distribution ($\Delta s \neq C$)						
h_k	$\varepsilon_k^{\mathrm{TR}}$	$\varepsilon_k^{\mathrm{SR}}$	$\varepsilon_k^{\mathrm{SRu}}$	$\hat{p}_k^{\mathrm{TR}}$	$\hat{p}_k^{\mathrm{SR}}$	$\hat{p}_k^{\mathrm{SRu}}$
0.2244	1.34×10^{2}	5.93×10^{3}	7.35×10^{5}	2.05	2.04	4.11
0.0467	5.36×10^{4}	2.39×10^{4}	1.16×10^{7}	2.01	2.01	4.02
0.0118	3.35×10^{5}	1.49×10^{5}	4.51×10^{10}	2.00	2.00	4.01
0.0029	2.09×10^{6}	9.34×10^{7}	1.76×10^{12}	2.00	2.00	3.82
0.0007	1.31×10^{7}	5.84×10^{8}	8.88×10^{15}	-	-	-

Figure B.2 shows the error development by reduction of the grid size parameter h_k (in other words, refining the computational grid). The slope of the lines equals the order of accuracy of the numerical scheme and as such shows that the trapezoidal rule is accurate to $\mathcal{O}(h^2)$, so second order accurate for both equally and unequally spaced data. The standard Simpson rule is accurate to $\mathcal{O}(h^4)$ (fourth order) for equally spaced data, but reduces to a second order accurate scheme when the spacing turns unequal. The modified Simpson rule remains fourth order accurate for unequally spaced data as intended.

[1] Slightly modified versions of the code are used as no distinction between any upper or lower side has to be made and no trailing edge components needs to be added separately.

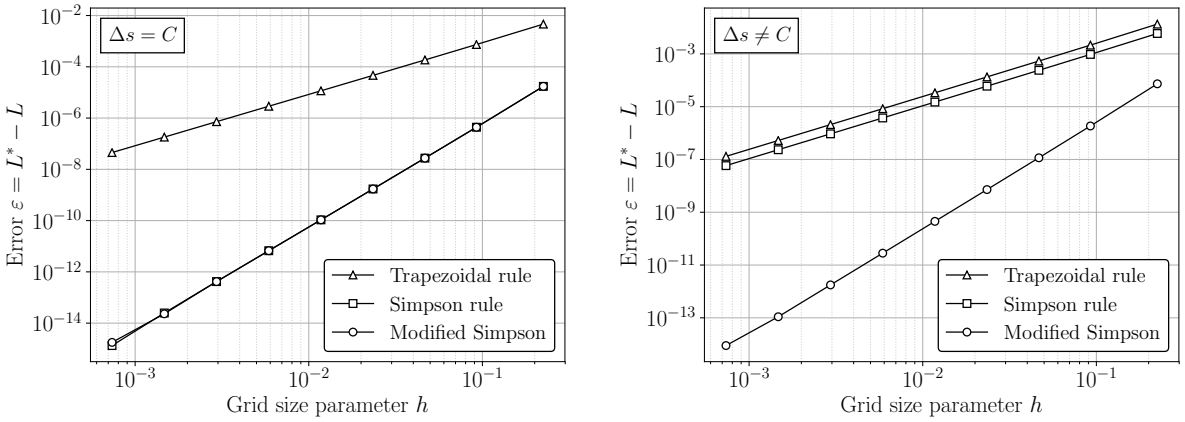

Figure B.2: Order of accuracy analysis of numerical integration schemes integrating $p(s) = \cos(s)$ for $s \in [0, 3\pi/2]$. In case of equally space data (l) and unequally spaced data (r). The standard Simpson rule fails to provide the expected fourth order accuracy when data is unequally spaced.

Lift and pressure drag through trapezoidal and Simpson's rule

Although the modified Simpson scheme is theoretically more accurate than the trapezoidal rule the question remains whether the programmed scheme integrates the lift and pressure drag coefficients, C_l, C_{dp} respectively, correctly. To answer this question pressure distributions from XFOIL are numerically integrated using both schemes to obtain the corresponding lift and drag polars. A comparison is then made to polars obtained from XFOIL directly to see the differences. The L_2 Norm of the lift and pressure drag is computed to asses the difference in accuracy between the quadrature rules.

$$L^*_{2,Cl} = \sqrt{\frac{1}{N-1}\sum_{i=0}^{N-1}\left(C^*_{l,i} - C^{\text{XF}}_{l,i}\right)^2} \quad \text{and} \quad L^*_{2,Cdp} = \sqrt{\frac{1}{N-1}\sum_{i=0}^{N-1}\left(C^*_{dp,i} - C^{\text{XF}}_{dp,i}\right)^2} \tag{B.26}$$

Figure B.3 shows the comparison of lift and pressure drag coefficient computed using both the trapezoidal rule and modified Simpson scheme compared to the results from XFOIL. The lift polar shows that calculation of the lift coefficient using either of the two schemes yield results comparable to XFOIL. The L_2 norms are 0.0055 and 0.0035 for the trapezoidal and Simpson scheme respectively.

The pressure drag polar however shows substantial discrepancies between the numerically integrated values and those obtained from XFOIL resulting in an L_2 norm of 0.0107 for the trapezoidal rule and 0.0116 in case of the Simpson scheme.

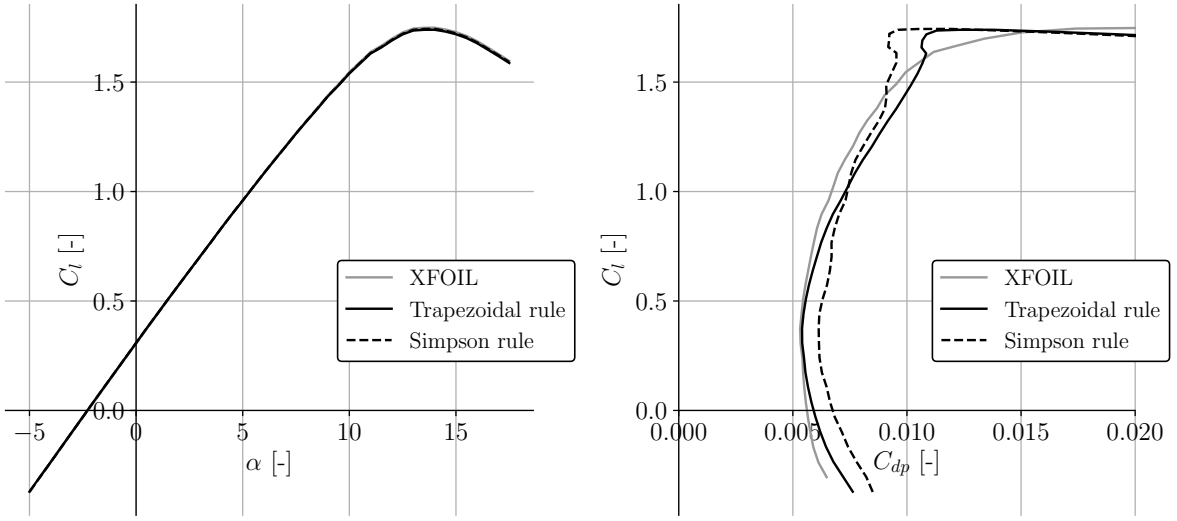

Figure B.3: Lift and drag polars comparing predictions from XFOIL with numerically integrated results.

Note on discontinuous functions

In case the function to be integrated contains discontinuities (e.g. shock waves in compressible flow) numerical integral using either of the discussed schemes will cause problems. If such functions are to be integrated numerically it should be performed separately for each smooth section in the domain after which the results are summed (see Klafter [28]). As the pressure distribution on an airfoil, assuming incompressible flow, generally is a smooth function both the trapezoidal rule and the modified Simpson rule are perfectly suitable to determine the section lift- and drag coefficients C_l, C_d.

C Datafile description

Measurements are performed with a sampling frequency of 10 Hz for a period of 30 seconds yielding 300 samples per measurement as explained in Section 5.5. Each operating point is measured twice to account for traversing of the wake rake from position A to B (see Section 5.2). Prior using the data for post-processing the average over 300 samples is taken. Data files written from LabVIEW have a predefined structure and are formatted as a `.txt` ASCII file that can be read by most applications on Windows or Linux systems. Table C.1 gives an overview of the data file columns.

Table C.1: Data file overview with description of the variables.

Column(s)	Name(s)	Variable(s)	Unit	Description
$1-16$	`box1_p<1-16>_Pa`	p_{w1-16}	Pa	Wake pressures circuits No. 1 till 16
$17-21$	`box2_p<1-5>_Pa`	p_{w17-21}	Pa	Wake pressures circuits No. 17 till 21
22	`box2_p6_Pa`	p_0	Pa	Total pressure at pitot-static tube [2]
23	`box2_p7_Pa`	p	Pa	Static pressure at pitot-static tube [2]
$24-32$	`box2_p<8-16>_Pa`	-	Pa	Not used
$33-48$	`box3_p<1-16>_Pa`	p_{1-16}	Pa	Surface pressure circuits No. 1 till 16
$49-63$	`box4_p<1-15>_Pa`	p_{33-47}	Pa	Surface pressure circuits No. 33 till 47
64	`box4_p16_Pa`	-	Pa	Not used
$65-80$	`box5_p<1-16>_Pa`	p_{17-32}	Pa	Surface pressure circuits No. 17 till 32
81	`Ttop_C`	T_{top}	°C	Temperature at left side of jet
82	`Tbottom_C`	T_{bot}	°C	Temperature at right side of jet
83	`Troom_C`	T_{room}	°C	Temperature below measurement section
84	`pdyn_Pa`	p_{dyn}	Pa	Dynamic pressure $(p_0 - p)$ at pitot-static tube [1]
85	`pamb_Pa`	p_∞	Pa	Ambient pressure from local weather station
86	`RH_pct`	RH	%	Relative Humidity in test cell
87	`rhoinf_kgm3`	ρ_∞	kg/m^3	Jet density (Equation 5.10)
88	`muinf_Pas`	μ_∞	Pa·s	Jet dynamic viscosity (Equation 5.9)
89	`Uinf_mps`	U_∞	m/s	Jet velocity (Equation 5.14) [1]
90	`Re`	Re_c	-	Chord Reynolds number (Equation 5.8) [1]
91	`Alpha`	α_t	°	Geometric angle of attack
92	`pdynPS_Pa`	p_{dyn}	Pa	Dynamic pressure $(p_0 - p)$ at pitot-static tube [2]
93	`UinfPS_mps`	U_∞	m/s	Jet velocity (Equation 5.14) [2]

Tables C.2 and C.3 lay out the data files for measurements at $\text{Re}_c = 0.87{\times}10^6$ and $\text{Re}_c = 0.35{\times}10^6$ respectively. Naming of the files was done in a set structure including the date and time combined with the geometric angle of attack and the designation A or B to denote the position of the wake rake.

`<yyyymmddhhmm>_alfa<Alpha>_<Options>_<A/B>.txt`

To distinguish measurements under forced transition conditions the optional naming `XtrTop` is added to the data file. For files at $\text{Re}_c = 0.35{\times}10^6$ an additional `re3p5e5` is added to the name string.

[1] From AE DPTI/CXLdp pressure sensor
[2] From Netscanner™ 9116 Pressure Scanners

Table C.2: Data files of measurement data for Reynolds number of 870,000.

$\mathrm{Re}_c = 0.87{\times}10^6$ Free transition		$\mathrm{Re}_c = 0.87{\times}10^6$ Forced transition	
A	*B*	*A*	*B*
201909171311_alfamin16_A.txt	201909171311_alfamin16_B.txt	201909231736_alfamin18A_XtrTop.txt	201909231736_alfamin18B_XtrTop.txt
201909171257_alfamin14_A.txt	201909171257_alfamin14_B.txt	201909231727_alfamin16A_XtrTop.txt	201909231727_alfamin16B_XtrTop.txt
201909191251_alfamin13_A.txt	201909191251_alfamin13_B.txt	201909231716_alfamin14A_XtrTop.txt	201909231716_alfamin14B_XtrTop.txt
201909191303_alfamin12_A.txt	201909191303_alfamin12_B.txt	201909241028_alfamin13A_XtrTop.txt	201909241028_alfamin13B_XtrTop.txt
201909190942_alfamin11_A.txt	201909190942_alfamin11_B.txt	201909231628_alfamin12A_XtrTop.txt	201909231628_alfamin12B_XtrTop.txt
201909171107_alfamin10_A.txt	201909171107_alfamin10_B.txt	201909241016_alfamin11A_XtrTop.txt	201909241016_alfamin11B_XtrTop.txt
201909190932_alfamin9_A.txt	201909190932_alfamin9_B.txt	201909231620_alfamin10A_XtrTop.txt	201909231620_alfamin10B_XtrTop.txt
201909190921_alfamin8_A.txt	201909190921_alfamin8_B.txt	201909241650_alfamin9A_XtrTop.txt	201909241650_alfamin9B_XtrTop.txt
201909171050_alfamin7p5_A.txt	201909171050_alfamin7p5_B.txt	201909231612_alfamin8A_XtrTop.txt	201909231612_alfamin8B_XtrTop.txt
201909190912_alfamin7_A.txt	201909190912_alfamin7_B.txt	201909231320_alfamin6A_XtrTop.txt	201909231320_alfamin6B_XtrTop.txt
201909171024_alfamin6_A.txt	201909171024_alfamin6_B.txt	201909231312_alfamin4A_XtrTop.txt	201909231312_alfamin4B_XtrTop.txt
201909251526_alfamin5A.txt	201909251526_alfamin5B.txt	201909231304_alfamin2A_XtrTop.txt	201909231304_alfamin2B_XtrTop.txt
201909171036_alfamin4_A.txt	201909171036_alfamin4_B.txt	201909231248_alfa0A_XtrTop.txt	201909231248_alfa0B_XtrTop.txt
201909251535_alfamin3A.txt	201909251535_alfamin3B.txt	201909231239_alfa2A_XtrTop.txt	201909231239_alfa2B_XtrTop.txt
201909170954_alfamin2_A.txt	201909170954_alfamin2_B.txt	201909231230_alfa4A_XtrTop.txt	201909231230_alfa4B_XtrTop.txt
201909191422_alfa0_A.txt	201909191422_alfa0_B.txt	201909231223_alfa6A_XtrTop.txt	201909231223_alfa6B_XtrTop.txt
201909161736_alfa2_A.txt	201909161736_alfa2_B.txt	201909231215_alfa8A_XtrTop.txt	201909231215_alfa8B_XtrTop.txt
201909161726_alfa4_A.txt	201909161726_alfa4_B.txt	201909231207_alfa10A_XtrTop.txt	201909231207_alfa10B_XtrTop.txt
201909161610_alfa6_A.txt	201909161610_alfa6_B.txt	201909241618_alfa11A_XtrTop.txt	201909241618_alfa11B_XtrTop.txt
201909161558_alfa8_A.txt	201909161558_alfa8_B.txt	201909231159_alfa12A_XtrTop.txt	201909231159_alfa12B_XtrTop.txt
201909161546_alfa10_A.txt	201909161546_alfa10_B.txt	201909240950_alfa13A_XtrTop.txt	201909240950_alfa13B_XtrTop.txt
201909191433_alfa12_A.txt	201909191433_alfa12_B.txt	201909241641_alfa13p5A_XtrTop.txt	201909241641_alfa13p5B_XtrTop.txt
201909251501_alfa13A.txt	201909251501_alfa13B.txt	201909231151_alfa14A_XtrTop.txt	201909231151_alfa14B_XtrTop.txt
201909131310_alfa14_A.txt	201909131310_alfa14_B.txt	201909240941_alfa14p5A_XtrTop.txt	201909240941_alfa14p5B_XtrTop.txt
201909251451_alfa15A.txt	201909251451_alfa15B.txt	201909231749_alfa15A_XtrTop.txt	201909231749_alfa15B_XtrTop.txt
201909251426_alfa16A.txt	201909251426_alfa16B.txt	201909231145_alfa16A_XtrTop.txt	201909231145_alfa16B_XtrTop.txt
201909241813_alfa16p5A.txt	201909241813_alfa16p5B.txt	201909241607_alfa17A_XtrTop.txt	201909241607_alfa17B_XtrTop.txt
201909131126_alfa17_A.txt	201909131126_alfa17_B.txt	201909231115_alfa18A_XtrTop.txt	201909231115_alfa18B_XtrTop.txt
201909131058_alfa17p5_A.txt	201909131058_alfa17p5_B.txt	201909231106_alfa20A_XtrTop.txt	201909231106_alfa20B_XtrTop.txt
201909191443_alfa18_A.txt	201909191443_alfa18_B.txt	201909231057_alfa22A_XtrTop.txt	201909231057_alfa22B_XtrTop.txt
201909171359_alfa19_A.txt	201909171359_alfa19_B.txt	201909231049_alfa24A_XtrTop.txt	201909231049_alfa24B_XtrTop.txt
201909171539_alfa19p25_A.txt	201909171539_alfa19p25_B.txt	201909231040_alfa26A_XtrTop.txt	201909231040_alfa26B_XtrTop.txt
201909171433_alfa19p5_A.txt	201909171433_alfa19p5_B.txt		
201909171608_alfa19p75_A.txt	201909171608_alfa19p75_B.txt		
201909171415_alfa20_A.txt	201909171415_alfa20_B.txt		
201909171555_alfa20p5_A.txt	201909171555_alfa20p5_B.txt		
201909171628_alfa21_A.txt	201909171628_alfa21_B.txt		
201909171644_alfa22_A.txt	201909171644_alfa22_B.txt		
201909190830_alfa23_A.txt	201909190830_alfa23_B.txt		
201909171658_alfa24_A.txt	201909171658_alfa24_B.txt		
201909181319_alfa26_A.txt	201909181319_alfa26_B.txt		

Table C.3: List of data files containing measurement data for Reynolds number of 350,000.

$\mathrm{Re}_c = 0.35{\times}10^6$ Free transition		$\mathrm{Re}_c = 0.35{\times}10^6$ Forced transition	
A	*B*	*A*	*B*
201909251552_alfamin8A_Re3p5e5.txt	201909251552_alfamin8B_Re3p5e5.txt	201909241159_alfamin8A_XtrTop_Re3p5e5.txt	201909241159_alfamin8B_XtrTop_Re3p5e5.txt
201909251548_alfamin6A_Re3p5e5.txt	201909251548_alfamin6B_Re3p5e5.txt	201909241134_alfamin6A_XtrTop_Re3p5e5.txt	201909241134_alfamin6B_XtrTop_Re3p5e5.txt
201909230858_alfamin4A_Re3p5e5.txt	201909230858_alfamin4B_Re3p5e5.txt	201909241121_alfamin4A_XtrTop_Re3p5e5.txt	201909241121_alfamin4B_XtrTop_Re3p5e5.txt
201909251556_alfamin4A2_Re3p5e5.txt	201909251556_alfamin4B2_Re3p5e5.txt	201909241206_alfamin4A2_XtrTop_Re3p5e5.txt	201909241206_alfamin4B2_XtrTop_Re3p5e5.txt
201909251605_alfamin2A2_Re3p5e5.txt	201909251605_alfamin2B2_Re3p5e5.txt	201909241113_alfamin2A_XtrTop_Re3p5e5.txt	201909241113_alfamin2B_XtrTop_Re3p5e5.txt
201909251613_alfamin2A_Re3p5e5.txt	201909251613_alfamin2A_Re3p5e5.txt	201909241210_alfamin2A2_XtrTop_Re3p5e5.txt	201909241210_alfamin2B2_XtrTop_Re3p5e5.txt
201909201352_alfa0A_Re3p5e5.txt	201909201352_alfa0B_Re3p5e5.txt	201909241108_alfa0A_XtrTop_Re3p5e5.txt	201909241108_alfa0B_XtrTop_Re3p5e5.txt
201909251645_alfa0A2_Re3p5e5.txt	201909251645_alfa0B2_Re3p5e5.txt	201909241214_alfa0A2_XtrTop_Re3p5e5.txt	201909241214_alfa0B2_XtrTop_Re3p5e5.txt
201909201356_alfa2A_Re3p5e5.txt	201909201356_alfa2B_Re3p5e5.txt	201909241221_alfa2A_XtrTop_Re3p5e5.txt	201909241221_alfa2B_XtrTop_Re3p5e5.txt
201909251649_alfa2A2_Re3p5e5.txt	201909251649_alfa2B2_Re3p5e5.txt	201909241228_alfa2A2_XtrTop_Re3p5e5.txt	201909241228_alfa2B2_XtrTop_Re3p5e5.txt
201909201402_alfa4A_Re3p5e5.txt	201909201402_alfa4B_Re3p5e5.txt	201909241234_alfa4A_XtrTop_Re3p5e5.txt	201909241234_alfa4B_XtrTop_Re3p5e5.txt
201909251710_alfa4A2_Re3p5e5.txt	201909251710_alfa4B2_Re3p5e5.txt	201909241253_alfa4A2_XtrTop_Re3p5e5.txt	201909241253_alfa4B2_XtrTop_Re3p5e5.txt
201909201407_alfa6A_Re3p5e5.txt	201909201407_alfa6B_Re3p5e5.txt	201909241459_alfa5A2_XtrTop_Re3p5e5.txt	201909241459_alfa5B2_XtrTop_Re3p5e5.txt
201909201412_alfa8A_Re3p5e5.txt	201909201412_alfa8B_Re3p5e5.txt	201909241519_alfa5A_XtrTop_Re3p5e5.txt	201909241519_alfa5B_XtrTop_Re3p5e5.txt
201909201416_alfa10A_Re3p5e5.txt	201909201416_alfa10B_Re3p5e5.txt	201909241301_alfa6A_XtrTop_Re3p5e5.txt	201909241301_alfa6B_XtrTop_Re3p5e5.txt
201909260943_alfa11A_Re3p5e5.txt	201909260943_alfa11B_Re3p5e5.txt	201909241315_alfa8A_XtrTop_Re3p5e5.txt	201909241315_alfa8B_XtrTop_Re3p5e5.txt
201909260937_alfa12A_Re3p5e5.txt	201909260937_alfa12B_Re3p5e5.txt	201909241320_alfa10A_XtrTop_Re3p5e5.txt	201909241320_alfa10B_XtrTop_Re3p5e5.txt
201909251752_alfa13A_Re3p5e5.txt	201909251752_alfa13B_Re3p5e5.txt	201909241450_alfa11A_XtrTop_Re3p5e5.txt	201909241450_alfa11B_XtrTop_Re3p5e5.txt
201909251747_alfa14A_Re3p5e5.txt	201909251747_alfa14B_Re3p5e5.txt	201909241326_alfa12A_XtrTop_Re3p5e5.txt	201909241326_alfa12B_XtrTop_Re3p5e5.txt
201909251742_alfa15A_Re3p5e5.txt	201909251742_alfa15B_Re3p5e5.txt	201909241443_alfa13A_XtrTop_Re3p5e5.txt	201909241443_alfa13B_XtrTop_Re3p5e5.txt
201909251737_alfa16A_Re3p5e5.txt	201909251737_alfa16B_Re3p5e5.txt	201909241335_alfa14A_XtrTop_Re3p5e5.txt	201909241335_alfa14B_XtrTop_Re3p5e5.txt
201909251732_alfa17A_Re3p5e5.txt	201909251732_alfa17B_Re3p5e5.txt	201909241435_alfa15A_XtrTop_Re3p5e5.txt	201909241435_alfa15B_XtrTop_Re3p5e5.txt
201909201437_alfa18A_Re3p5e5.txt	201909201437_alfa18B_Re3p5e5.txt	201909241430_alfa17A_XtrTop_Re3p5e5.txt	201909241430_alfa17B_XtrTop_Re3p5e5.txt
201909201446_alfa19A_Re3p5e5.txt	201909201446_alfa19B_Re3p5e5.txt	201909241354_alfa18A_XtrTop_Re3p5e5.txt	201909241354_alfa18B_XtrTop_Re3p5e5.txt
201909201457_alfa19p5A_Re3p5e5.txt	201909201457_alfa19p5B_Re3p5e5.txt	201909241537_alfa19A_XtrTop_Re3p5e5.txt	201909241537_alfa19B_XtrTop_Re3p5e5.txt
201909251723_alfa19p75A_Re3p5e5.txt	201909251723_alfa19p75B_Re3p5e5.txt	201909241400_alfa20A_XtrTop_Re3p5e5.txt	201909241400_alfa20B_XtrTop_Re3p5e5.txt
201909201441_alfa20A_Re3p5e5.txt	201909201441_alfa20B_Re3p5e5.txt	201909241406_alfa22A_XtrTop_Re3p5e5.txt	201909241406_alfa22B_XtrTop_Re3p5e5.txt
201909251728_alfa21A_Re3p5e5.txt	201909251728_alfa21B_Re3p5e5.txt		
201909230906_alfa22A_Re3p5e5.txt	201909230906_alfa22B_Re3p5e5.txt		

D XFOIL and Python - AeroPy

In this thesis all processing of data is done with the help of the Python programming language, the Numpy package and the Spyder IDE (Integrated Development Environment) all contained in the Anaconda distribution. The aerodynamic analysis capabilities of XFOIL can be neatly integrated in any Python script with the help of the package AeroPy. AeroPy is a 3rd party package allowing one to call XFOIL from any Python script. The package is developed by Pedro Leal and available on Github.

To download and install AeroPy on a Windows OS the following steps have been followed:

1. Download `Aeropy-Master.zip` from https://github.com/leal26/AeroPy
2. Unpack the files in the download directory
3. Using the Anaconda Prompt navigate (`cd`) to the download directory
4. Execute: `python setyp.py install` in the Anaconda Prompt
5. AeroPy is now installed in `C:\Users\<USER>\Anaconda3\Lib\site-packages\aeropy-0.0-py3.7.egg`
6. Copy folder 'aeropy' to `C:\Users\<USER>\Anaconda3\Lib\site-packages`

To call the AeroPy XFOIL module one includes the following line in a Python script:

```
import aeropy.xfoil_module as xfoil
```

E Tabulated measurement results

E.1 Reynolds number 870,000 - free transition

Table E.1: Measured aerodynamic coefficients at $\mathrm{Re}_c = 0.87{\times}10^6$ *under free transition conditions.*

$\alpha_t\,[^\circ]$	$\alpha_{\mathrm{eff}}\,[^\circ]$	$\mathrm{Re}_c\,[-]$	$C_l\,[-]$	$C_m\,[-]$	$C_d\,[-]$	$C_{dp}\,[-]$	$C_l/C_d\,[-]$
-16.0	-12.89	869756	-0.689	0.0250	0.1538	0.1136	-4.480
-14.0	-11.14	871370	-0.630	0.0131	0.1412	0.1002	-4.461
-13.0	-10.16	868967	-0.621	-0.0060	0.1193	0.0904	-5.203
-12.0	-9.28	871715	-0.590	-0.0292	0.0980	0.0766	-6.024
-11.0	-8.33	870000	-0.571	-0.0529	0.0720	0.0559	-7.938
-10.0	-7.55	869256	-0.521	-0.0618	0.0603	0.0514	-8.642
-9.0	-6.68	871557	-0.484	-0.0994	0.0268	0.0256	-18.091
-8.0	-5.94	870800	-0.427	-0.1037	0.0258	0.0220	-16.527
-7.5	-5.66	868910	-0.377	-0.1077	0.0179	0.0192	-20.998
-7.0	-5.28	869921	-0.348	-0.1127	0.0155	0.0157	-22.385
-6.0	-4.65	869240	-0.265	-0.1195	0.0131	0.0124	-20.214
-5.0	-4.02	868757	-0.183	-0.1266	0.0137	0.0092	-13.361
-4.0	-3.31	870281	-0.118	-0.1272	0.0125	0.0080	-9.490
-3.0	-2.60	868650	-0.055	-0.1292	0.0135	0.0063	-4.059
-2.0	-1.95	872240	0.022	-0.1309	0.0128	0.0059	1.710
0.0	-0.66	869903	0.179	-0.1364	0.0134	0.0057	13.428
2.0	0.69	870852	0.323	-0.1403	0.0125	0.0093	25.934
4.0	2.09	869967	0.455	-0.1439	0.0131	0.0157	34.789
6.0	3.40	871173	0.608	-0.1468	0.0132	0.0169	45.999
8.0	4.67	868918	0.769	-0.1508	0.0133	0.0189	57.708
10.0	6.00	871421	0.917	-0.1527	0.0149	0.0212	61.382
12.0	7.35	870191	1.059	-0.1539	0.0145	0.0252	73.128
13.0	8.02	869795	1.132	-0.1528	0.0145	0.0256	77.883
14.0	8.75	868827	1.191	-0.1507	0.0161	0.0280	73.809
15.0	9.49	869904	1.246	-0.1467	0.0185	0.0293	67.276
16.0	10.28	869919	1.292	-0.1409	0.0248	0.0302	51.989
16.5	10.69	870692	1.311	-0.1395	0.0301	0.0323	43.604
17.0	11.07	868098	1.336	-0.1396	0.0292	0.0358	45.709
17.5	11.48	871136	1.357	-0.1395	0.0358	0.0384	37.922
18.0	11.90	870276	1.374	-0.1400	0.0435	0.0426	31.592
19.0	12.90	869855	1.374	-0.1384	0.0667	0.0550	20.594
19.3	13.84	870322	1.225	-0.1473	0.1323	0.0874	9.260
19.5	14.92	869211	1.043	-0.1484	0.1704	0.1128	6.120
19.8	15.55	869327	0.960	-0.1491	0.1879	0.1291	5.109
20.0	15.90	871038	0.937	-0.1429	0.1972	0.1283	4.749
20.5	16.58	870568	0.896	-0.1437	0.1989	0.1424	4.503
21.0	17.15	868607	0.881	-0.1419	0.2267	0.1482	3.885
22.0	18.30	871312	0.847	-0.1385	0.2497	0.1605	3.393
23.0	19.44	869707	0.815	-0.1374	0.2832	0.1745	2.878
24.0	20.55	871309	0.793	-0.1417	0.3142	0.1944	2.525
26.0	22.77	869762	0.750	-0.1615	0.3476	0.2529	2.159

E.2 Reynolds number 870,000 - forced transition

Table E.2: Measured aerodynamic coefficients at $\mathrm{Re}_c = 0.87{\times}10^6$ *under forced transition conditions.*

$\alpha_t\,[^\circ]$	$\alpha_{\mathrm{eff}}\,[^\circ]$	$\mathrm{Re}_c\,[-]$	$C_l\,[-]$	$C_m\,[-]$	$C_d\,[-]$	$C_{dp}\,[-]$	$C_l/C_d\,[-]$
-18.0	-14.68	869443	-0.737	0.0311	0.1594	0.1193	-4.621
-16.0	-12.85	869697	-0.698	0.0223	0.1551	0.1075	-4.500
-14.0	-11.01	868306	-0.657	0.0055	0.1294	0.0956	-5.080
-13.0	-9.95	870642	-0.664	-0.0189	0.1043	0.0833	-6.360
-12.0	-8.89	870259	-0.669	-0.0522	0.0786	0.0633	-8.508
-11.0	-8.00	869921	-0.638	-0.0792	0.0562	0.0414	-11.352
-10.0	-7.27	869437	-0.575	-0.0929	0.0373	0.0316	-15.402
-9.0	-6.54	870687	-0.515	-0.0972	0.0329	0.0276	-15.660
-8.0	-5.88	872102	-0.440	-0.1042	0.0224	0.0218	-19.600
-6.0	-4.59	868619	-0.280	-0.1195	0.0157	0.0135	-17.862
-4.0	-3.24	869462	-0.134	-0.1256	0.0159	0.0095	-8.449
-2.0	-1.87	868860	0.003	-0.1286	0.0156	0.0074	0.223
0.0	-0.53	868135	0.150	-0.1322	0.0158	0.0077	9.505
2.0	0.85	868754	0.287	-0.1351	0.0158	0.0118	18.215
4.0	2.26	869387	0.417	-0.1370	0.0162	0.0171	25.710
6.0	3.60	869368	0.562	-0.1384	0.0173	0.0195	32.427
8.0	4.98	870094	0.698	-0.1380	0.0185	0.0223	37.761
10.0	6.35	868435	0.835	-0.1349	0.0209	0.0239	39.981
11.0	7.07	869608	0.896	-0.1325	0.0228	0.0252	39.390
12.0	7.85	868104	0.944	-0.1284	0.0253	0.0278	37.265
13.0	8.63	869461	0.991	-0.1242	0.0284	0.0303	34.955
13.5	9.07	868695	1.002	-0.1191	0.0328	0.0304	30.555
14.0	9.82	870677	0.946	-0.1109	0.0623	0.0370	15.170
14.5	10.98	870619	0.798	-0.1046	0.1088	0.0517	7.335
15.0	11.68	870406	0.754	-0.1035	0.1326	0.0612	5.688
16.0	12.76	870580	0.737	-0.1030	0.1530	0.0735	4.815
17.0	13.74	867613	0.742	-0.1044	0.1735	0.0839	4.278
18.0	14.69	869406	0.752	-0.1046	0.1860	0.0936	4.043
20.0	16.59	869335	0.775	-0.1067	0.2095	0.1144	3.697
22.0	18.49	869880	0.800	-0.1135	0.2414	0.1399	3.313
24.0	20.37	870347	0.828	-0.1237	0.2688	0.1684	3.081
26.0	22.37	868744	0.832	-0.1386	0.3156	0.2106	2.636

E.3 Reynolds number 350,000 - free transition

Table E.3: Measured aerodynamic coefficients at $\mathrm{Re}_c = 0.35{\times}10^6$ *under free transition conditions. Duplicate values at constant angles of attack represent hysteresis points.*

$\alpha_t\,[^\circ]$	$\alpha_{\mathrm{eff}}\,[^\circ]$	$\mathrm{Re}_c\,[-]$	$C_l\,[-]$	$C_m\,[-]$	$C_d\,[-]$	$C_{dp}\,[-]$	$C_l/C_d\,[-]$
-8.0	-8.74	350240	0.172	-0.0338	0.1440	0.0963	1.194
-6.0	-7.13	350765	0.257	-0.0382	0.1384	0.0859	1.859
-4.0	-5.51	349825	0.341	-0.0424	0.1241	0.0782	2.752
-2.0	-3.88	350601	0.425	-0.0455	0.1115	0.0724	3.811
0.0	-2.20	349858	0.495	-0.0499	0.1129	0.0725	4.388
2.0	-0.60	349480	0.584	-0.0501	0.0957	0.0662	6.103
4.0	1.07	350429	0.657	-0.0507	0.0884	0.0650	7.431
-4.0	-3.18	354337	-0.150	-0.1156	0.0229	0.0241	-6.567
-2.0	-1.81	350288	-0.010	-0.1202	0.0198	0.0190	-0.518
0.0	-0.56	350037	0.156	-0.1272	0.0203	0.0174	7.691
2.0	0.77	349386	0.304	-0.1317	0.0200	0.0162	15.166
4.0	2.08	350224	0.456	-0.1378	0.0199	0.0171	22.895
6.0	3.38	351143	0.611	-0.1411	0.0204	0.0173	30.024
8.0	4.66	351064	0.770	-0.1454	0.0212	0.0194	36.292
10.0	6.05	349279	0.903	-0.1459	0.0220	0.0222	41.095
11.0	6.70	350252	0.982	-0.1477	0.0207	0.0254	47.390
12.0	7.43	350748	1.040	-0.1478	0.0208	0.0309	50.021
13.0	8.09	350242	1.116	-0.1495	0.0248	0.0338	45.078
14.0	8.82	349372	1.175	-0.1485	0.0248	0.0357	47.285
15.0	9.55	349987	1.234	-0.1467	0.0243	0.0367	50.849
16.0	10.26	350610	1.296	-0.1440	0.0247	0.0378	52.461
17.0	11.13	350331	1.324	-0.1415	0.0265	0.0484	49.918
18.0	12.04	350126	1.343	-0.1372	0.0301	0.0581	44.682
19.0	12.89	350050	1.375	-0.1331	0.0477	0.0610	28.833
19.5	13.37	350749	1.380	-0.1349	0.0605	0.0694	22.803
19.8	14.88	350706	1.107	-0.1487	0.1508	0.1083	7.340
20.0	15.26	350353	1.078	-0.1458	0.1738	0.1137	6.198
21.0	16.44	349665	1.037	-0.1414	0.1940	0.1266	5.343
22.0	17.61	349883	0.999	-0.1383	0.2068	0.1410	4.830

E.4 Reynolds number 350,000 - forced transition

Table E.4: Measured aerodynamic coefficients at $\mathrm{Re}_c = 0.35{\times}10^6$ *under forced transition conditions. Duplicate values at constant angles of attack represent hysteresis points.*

$\alpha_t\,[^\circ]$	$\alpha_{\mathrm{eff}}\,[^\circ]$	$\mathrm{Re}_c\,[-]$	$C_l\,[-]$	$C_m\,[-]$	$C_d\,[-]$	$C_{dp}\,[-]$	$C_l/C_d\,[-]$
-8.0	-8.74	350130	0.170	-0.0323	0.1533	0.0948	1.109
-6.0	-7.10	349614	0.252	-0.0377	0.1385	0.0870	1.818
-4.0	-5.49	350474	0.337	-0.0422	0.1279	0.0789	2.635
-2.0	-3.85	350788	0.418	-0.0451	0.1134	0.0729	3.686
0.0	-2.20	349945	0.495	-0.0484	0.1036	0.0696	4.783
2.0	-0.57	350306	0.577	-0.0508	0.0980	0.0664	5.890
4.0	1.13	350326	0.642	-0.0490	0.0932	0.0663	6.883
5.0	1.98	342362	0.675	-0.0493	0.0883	0.0659	7.650
-4.0	-3.10	351356	-0.170	-0.1112	0.0237	0.0246	-7.169
-2.0	-1.75	350542	-0.025	-0.1167	0.0231	0.0200	-1.106
0.0	-0.42	351269	0.124	-0.1219	0.0214	0.0179	5.785
2.0	0.88	351001	0.279	-0.1269	0.0209	0.0164	13.349
4.0	2.22	350403	0.423	-0.1298	0.0210	0.0170	20.167
5.0	2.88	350447	0.499	-0.1318	0.0215	0.0175	23.177
6.0	3.55	349981	0.571	-0.1316	0.0236	0.0179	24.239
8.0	4.95	349939	0.702	-0.1317	0.0244	0.0211	28.760
10.0	6.41	350147	0.821	-0.1274	0.0260	0.0242	31.581
11.0	7.20	350718	0.866	-0.1231	0.0275	0.0277	31.500
12.0	8.10	350548	0.886	-0.1197	0.0296	0.0375	29.888
13.0	9.10	351117	0.884	-0.1092	0.0574	0.0406	15.409
14.0	10.16	350134	0.871	-0.1086	0.0636	0.0545	13.699
15.0	11.38	350206	0.819	-0.0958	0.1071	0.0545	7.651
17.0	13.21	350346	0.858	-0.1038	0.1103	0.0812	7.774
18.0	14.16	350254	0.870	-0.1045	0.1226	0.0917	7.093
19.0	15.13	349742	0.878	-0.1089	0.1358	0.1068	6.465
20.0	16.18	350012	0.865	-0.1036	0.1711	0.1096	5.057
22.0	18.03	350403	0.900	-0.1097	0.1820	0.1327	4.941

F Pressure distributions

F.1 Reynolds number 870,000 - free transition

Figure F.1 shows surface pressure measurements at selected angles of attack comparable with reference data from Baldacchino et al. measured at $\mathrm{Re}_c = 2.0{\times}10^6$ in the Delft University of Technology low turbulence wind tunnel (see Section 4.1.1). The reference data shows overall lower suction side surface pressures, most likely due to the increased Reynolds number. The measured pressures on the pressure side show very good agreement with the reference data and XFOIL predictions.

Although the measurement resolution is quite coarse laminar separation bubbles can be distinguished at $\alpha = 7.2°, 9.3°, 10.9°$ and $12.7°$ besides that, XFOIL predictions of transition seem to match the reference data. At angles of attack post $C_{l,\max}$ ($\alpha = 12.7°$) XFOIL predictions start to deviate significantly as expected. The steep increase in pressure as the flow separates from the suction side is clearly visible in both the measurement and reference data.

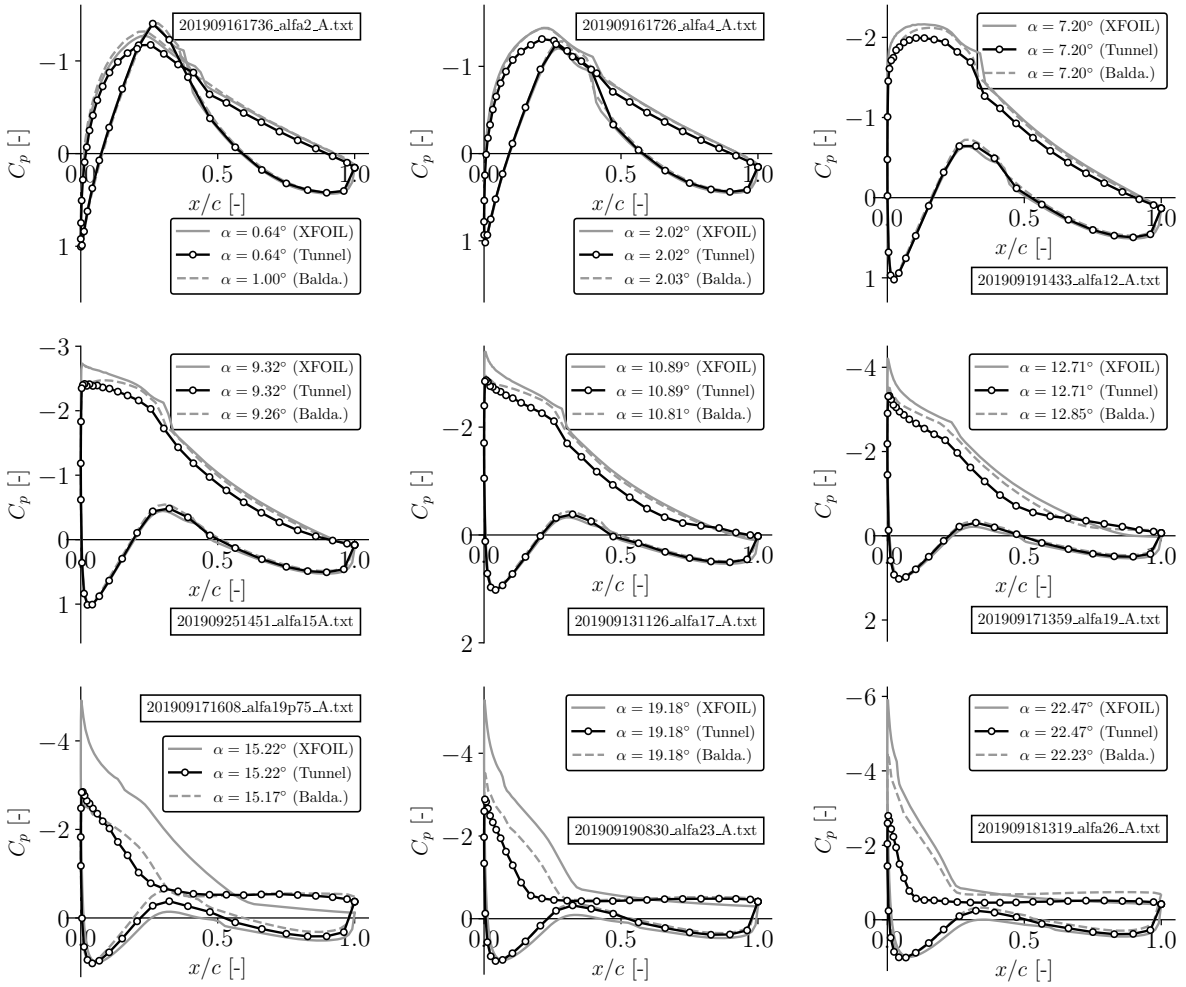

Figure F.1: Measured pressure distributions at selected (effective) angles of attack under free transition conditions at $\mathrm{Re}_c = 0.87{\times}10^6$. *The data is compared to simulations from XFOIL at* $\mathrm{Re}_c = 0.87{\times}10^6$ *and experimental data from Baldacchino et al. measured at* $\mathrm{Re}_c = 2.00{\times}10^6$

F.2 Reynolds number 870,000 - forced transition

Surface pressure measurements at $\mathrm{Re}_c = 0.87{\times}10^6$ under tripped conditions are shown in Figure F.2. Tripping of the boundary layer is done using 0.3 mm thick zigzag tape applied at $0.05x/c$ on the suction side (see Section 5.3.5). Reference data at $\mathrm{Re}_c = 2.0{\times}10^6$ is cross plotted. Presence of the zigzag tape is clearly visible in the pressure distributions as a small suction spike just downstream the tape.

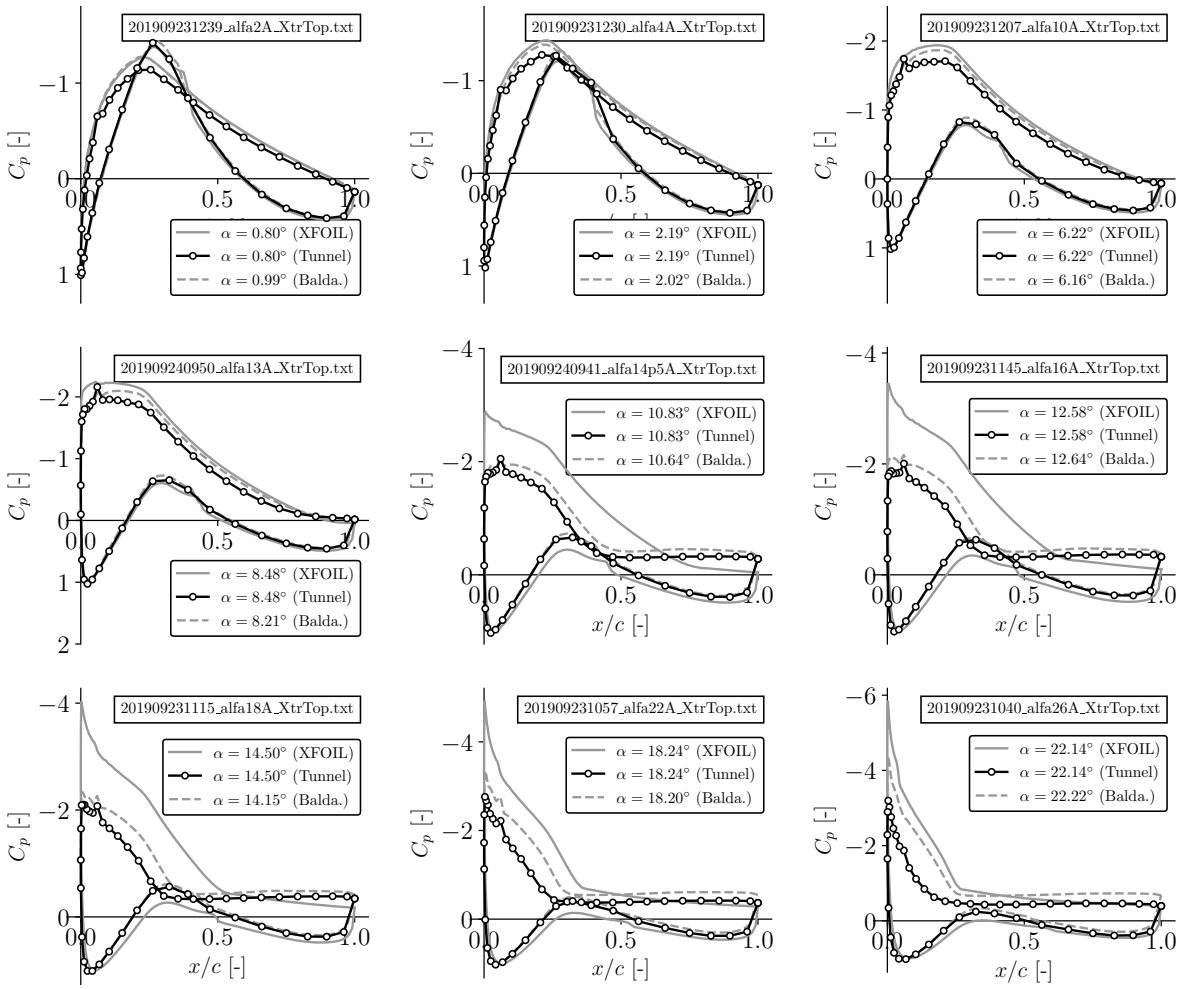

Figure F.2: Measured pressure distributions at selected (effective) angles of attack under forced transition conditions. Boundary layer tripping is performed at 0.05c using zigzag tape. The data is compared to results acquired by Baldaccino et al. and simulations from XFOIL.

F.3 Reynolds number 350,000 - free transition

Pressure distributions at $\mathrm{Re}_c = 0.35{\times}10^6$ are shown in Figure F.3. The top three plots show the hysteresis phenomenon discussed in Section 5.6.2 where the dashed lines represent the separated flow state which XFOIL is unable to predict. Large laminar separation bubbles arise at this low Reynolds number as laminar flow is maintained within regions of adverse pressure gradient.

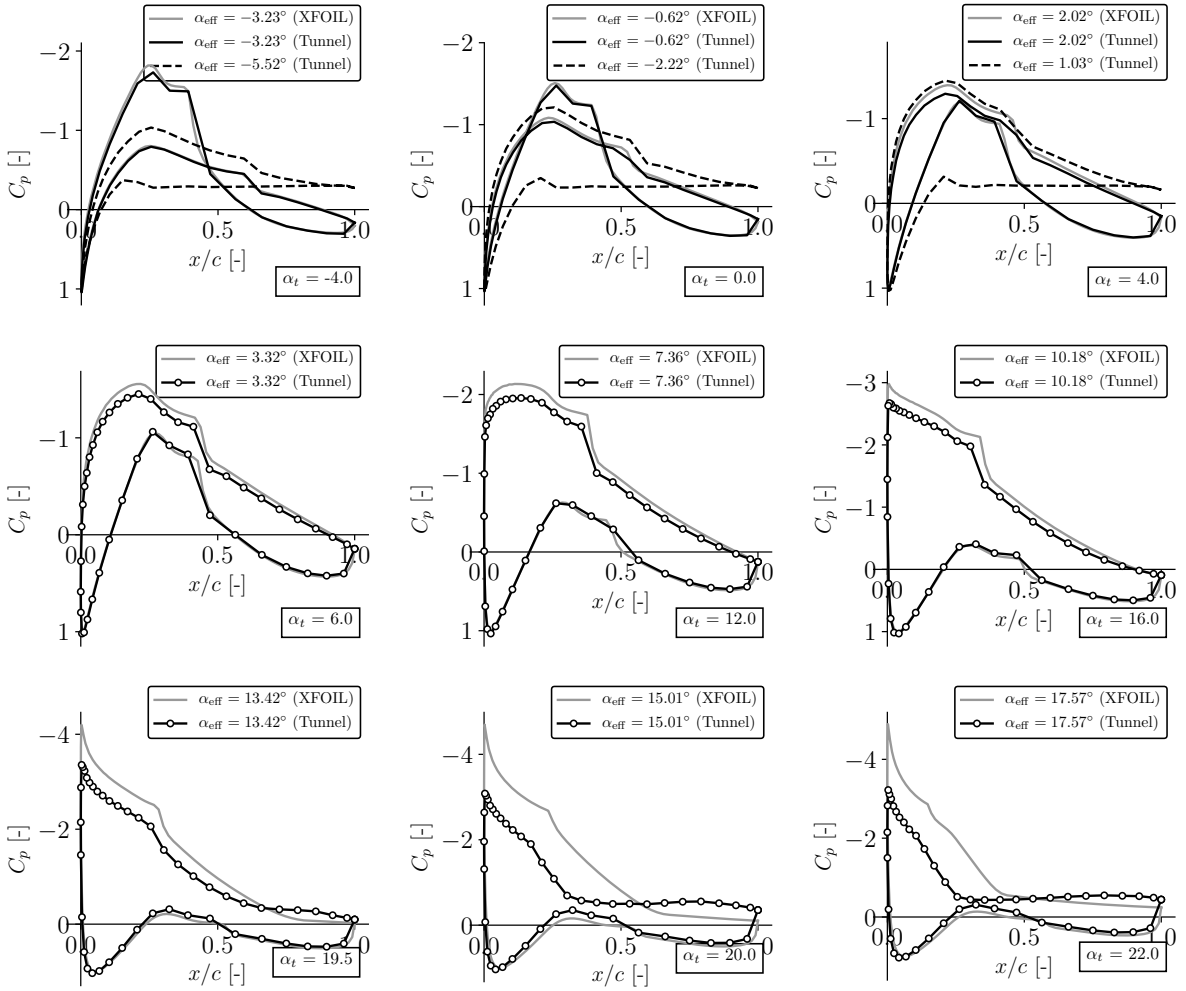

Figure F.3: Measured pressure distributions at $\mathrm{Re}_c = 0.35{\times}10^6$ *at selected angles of attack under free transition conditions.*

F.4 Reynolds number 350,000 - forced transition

C_p vs. x/c plots at $\mathrm{Re}_c = 0.35{\times}10^6$ under forced transition conditions are shown in Figure F.4. Again the hysteresis phenomenon discussed in Section 5.6.2 is visible. Laminar separation bubbles are absent as the boundary layer is forced turbulent prior the separation point.

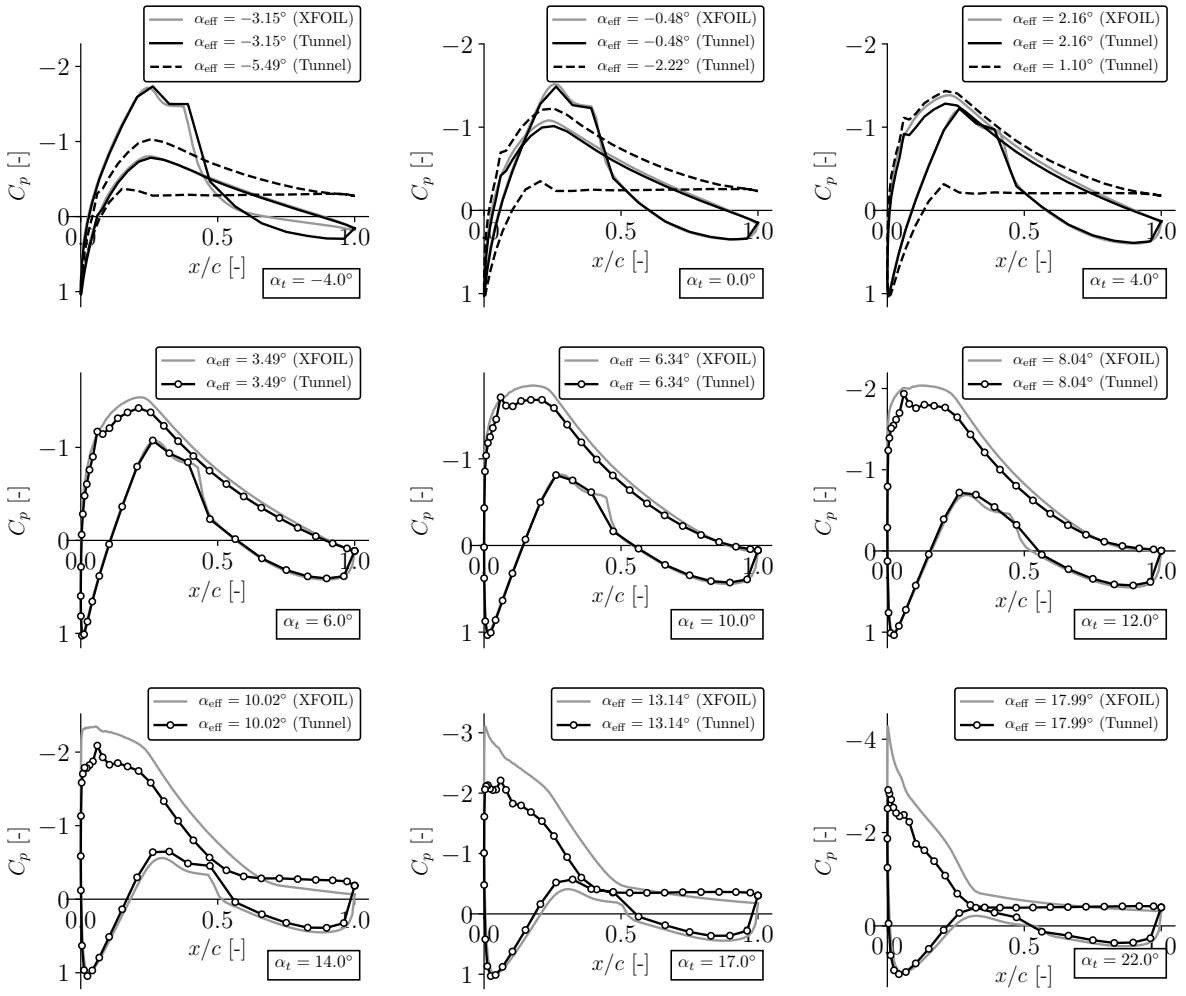

Figure F.4: Measured pressure distributions at $\mathrm{Re}_c = 0.35{\times}10^6$ *at selected angles of attack under forced transition conditions. Boundary layer tripping is performed at 0.05c using zigzag tape.*

G Note on calibrations

To assure sufficient confidence in the acquired pressures and temperatures the corresponding measurement equipment should be calibrated against known (and accurate) references. Three out of the five Netscanner® Pressure Scanner 9116 devices had been calibrated within twelve months of the measurements, One device was calibrated within 18 months from the measurements and one device was only calibrated eight years prior the experiments. Table G.1 gives an overview of the pressure scanners used and their calibration dates.

Table G.1: Pressure scanners used in experiments

No.	Model	Range	S/N	Default IP-address	Calibration date	Applied for:
1	9116	±1.0 psi	9430	`200.200.36.214`	03/2018	Wake rake 1-16
2	9116	±1.0 psi	6498	`200.200.25.98`	02/2011	Wake rake 17-21 & pitot tube
3	9216	±1.0 psi	20452	`200.210.97.228`	06/2019	Surface pressures 1-16
4	9216	±1.0 psi	20451	`200.210.79.227`	06/2019	Surface pressures 33-47
5	9216	±2.5 psi	20447	`200.210.79.223`	06/2019	Surface pressures 17-32

As the last calibration of S/N 6498 was more than 18 months prior the experiments a calibration check was performed by taking S/N 9430 as reference device. Both devices are subjected to a common pressure source during which data is recorded simultaneously. All 16 channels of S/N 9430 are averaged to establish a reasonable estimate of the true pressure to which the channels of S/N 6498 refer to. The error ε is computed for each channel and checked against the allowable error

$$\varepsilon_i = p_i - p_{ref} \quad \text{with} \quad p_{ref} = \frac{1}{16}\sum_{i}^{16} p_{9430,i} \tag{G.1}$$

Results of the calibration check are shown in Figure G.1(l) revealing that between ±0.5 psi (±3447 Pa) all channels of S/N 6498 were within the allowable error band (±0.0015 psi / ±10.3 Pa).

Next to the S/N 6498 pressure scanner the AE DPTI/CXLdp sensor used for the pitot-static tube was checked against the S/N 9430 pressure scanner for accuracy of the calibration. Figure G.1(r) shows the results of the calibration check revealing that at 500 and 1000 Pa the error is larger than the specified accuracy band (±6.25 Pa) namely -9.8 and -9.1 Pa respectively. However the dynamic pressure measured at the pitot static tube at 52 and 21 m/s ($\mathrm{Re}_c \approx 0.87{\times}10^6$ and $\mathrm{Re}_c \approx 0.35{\times}10^6$) is 1629 and 265 Pa respectively[1] for which the measured accuracy of the AE DPTI/CXLdp sensor is within the specified error band.[2]

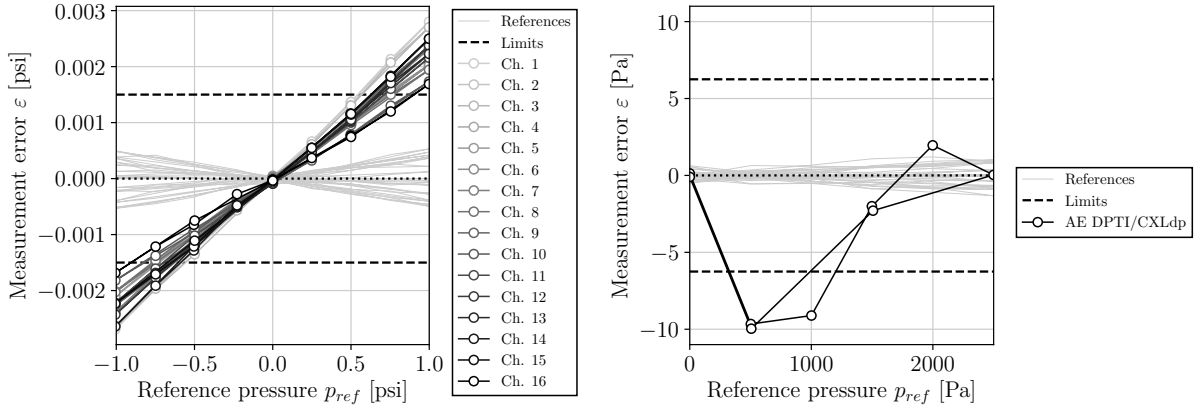

Figure G.1: Calibration checks of the S/N 6498 pressure scanner (l) and the AE DPTI/CXLdp sensor (r). The reference pressure p_{ref} is obtained by averaging of all channels of the S/N 9430 pressure scanner.

[1] At 20°C yielding $\rho = 1.204$ kg/m^3 and $\nu = 1.516{\times}10^{-5}$ m^2/s.
[2] Up to 300 Pa the AE DPTI/CXLdp sensor was calibrated using a Betz Manometer device in 04/2019.

H Richardson extrapolation

The concept of Richardson Extrapolation aims to find an estimate $\bar{f}$ of the exact solution $\tilde{f}$ to a mathematical problem based on the numerical solutions on two systematically refined computational grids, knowing the formal rate of convergence of the used discretization method. The method considers the discretization error ε_h of a certain solution variable f on a grid with spacing h

$$\varepsilon_h = f_h - \tilde{f} \tag{H.1}$$

Where f_h and $\tilde{f}$ are the discrete solution on the grid of size h and exact solution to the differential equations respectively. We can expand the discrete solution f_h in a Taylor series around the exact solution, which can be generalized as a power series.

$$\begin{aligned} f_h &= \tilde{f} + \frac{\partial \tilde{f}}{\partial h}h + \frac{\partial^2 \tilde{f}}{\partial h^2}h^2 + \frac{\partial^3 \tilde{f}}{\partial h^3}h^3 + \mathcal{O}\left(h^4\right) \\ &= \tilde{f} + g_1 h + g_2 h^2 + g_3 h^3 + \mathcal{O}\left(h^4\right) \end{aligned} \tag{H.2}$$

Moving $\tilde{f}$ to the left hand side yields the expression for the discretization error:

$$\varepsilon_h = f_h - \tilde{f} = g_1 h + g_2 h^2 + g_3 h^3 + \mathcal{O}\left(h^4\right) \tag{H.3}$$

The general form of Richardson Extrapolation considers p^{th}-order accurate schemes on two grids refined by an arbitrary grid refinement factor $r = h_2/h_1 > 1$. The general expression for the discretization error can be written as:

$$\varepsilon_h = f_h - \tilde{f} = g_p h^p + g_{p+1} h^{p+1} + g_{p+2} h^{p+2} + \mathcal{O}\left(h^{p+3}\right) \tag{H.4}$$

Now we consider two grid sizes h_1 and h_2 where $h_2 = r h_1$ of which the numerical solutions f_1 and f_2 have been computed. We can expand these numerical solutions as:

$$f_1 = \tilde{f} + g_p h_1^p + g_{p+1} h_1^{p+1} + \mathcal{O}(h_1^{p+2}) \tag{H.5}$$

$$f_2 = \tilde{f} + g_p (r h_1)^p + g_{p+1} (r h_1)^{p+1} + \mathcal{O}(h_1^{p+2}) \tag{H.6}$$

From these equations we eliminate g_p and solve for $\tilde{f}$ yielding:

$$\tilde{f} = f_1 + \frac{f_1 - f_2}{r^p - 1} + g_{p+1} h_1^{p+1} \frac{r^p (r-1)}{r^p - 1} + \mathcal{O}(h_1^{p+2}) \tag{H.7}$$

If we now combine the terms with order h_1^{p+1} with the exact solution $\tilde{f}$ we obtain the generalized Richardson extrapolation estimate $\bar{f}$:

$$\bar{f} = f_1 + \frac{f_1 - f_2}{r^p - 1} \tag{H.8}$$